Imaging Polyatomic Molecules in Three Dimensions Using Molecular Frame Photoelectron
Angular Distributions

by

Joshua Brown Williams

A dissertation submitted to the Graduate Faculty of
Auburn University
in partial fulfillment of the
requirements for the Degree of
Doctor of Philosophy

Auburn, Alabama
May 7, 2011

Keywords: COLTRIMS, Methane, MFPAD, K-Shell Photoionization

Approved by

Allen L. Landers, Carr Professor of Physics
Michael Fogle, Assistant Professor of Physics
Thorsten Weber, Staff Scientist, Lawrence Berkeley National Laboratory
Joe D. Perez, Full Professor of Physics and Physics Department Head
Vincent Ortiz, Ruth W. Molette Professor and Chemistry Deparment Chairman

Abstract

We demonstrate a method for determining the full three-dimensional molecular frame photoelectron angular distribution in polyatomic molecules using methane as a prototype. Simultaneous double Auger decay and subsequent dissociation allow measurement of the initial momentum vectors of the ionic fragments and the photoelectron in coincidence, allowing full orientation by observing a three-ion decay pathway, $[H^+, H^+, CH_2^+]$. Prompt dissociation in the two-ion decay pathway, $[H^+, H^+, CH_2]$, also allows for full three-dimensional orientation of the molecule. We find the striking result that at low photoelectron energies the molecule is effectively imaged by the focusing of photoelectrons along bond directions. Furthermore, we observe a dynamic breakdown of axial recoil behavior in one of the dissociation pathways of the intermediate dication, which we interpret using electronic structure calculations.

To the memory of my brother,
Matthew Williams

"Death is certain, replacing both the siren-song of Paradise and the dread of Hell. Life on this earth, with all its mystery and beauty and pain, is then to be lived far more intensely: we stumble and get up, we are sad, confident, insecure, feel loneliness and joy and love. There is nothing more; but I want nothing more."

—Christopher Hitchens

Acknowledgments

The task of acknowledging everyone who should be acknowledged seems a superhuman one. The experiment that led to this dissertation took many people and is by no means mine alone. I would like to thank my undergraduate mentor Justin Sanders for his patience with me and my complete and total lack of the prerequisite knowledge needed. Thorsten Weber for supporting me throughout this experiment and dissertation. Ali Moradmand and Jon Hebert for their continual help no matter how trivial the task. Mike Fogle for always having the time to help me. Markus Schöffler and Till Jahnke for always sharing their immense knowledge.

My advisor, Allen Landers has been a constant guide in my graduate studies, and has given me every opportunity to succeed. I can not thank Allen enough. Our theoretical collaboration with Bill McCurdy, Cynthia Trevisan, and Tom Rescigno for their guidance and knowledge in this experiment. Chapters 4 and 5 are a synthesis of two papers we coauthored and published with them, and I would like to thank them for allowing me to use material from those papers here. I would especially like to thank Bill for all of his efforts.

The two people who influenced me the most in life must be, of course, my parents, Ralph & Melanie. I do not know how to properly thank them. They instilled a sense of wonder and supported me no matter where my foolish ambition led me. I could not ask for better parents.

Contents

List of Figures

List of Tables

Chapter 1

Introduction

"Facts are the air of scientists. Without them you can never fly."

—Linus Pauling

1.1 Overview

The experiment presented in this dissertation examines the photoelectron and molecular dynamics following core ionization of methane (CH_4), which is accomplished via absorption of a soft x-ray photon produced by the Advanced Light Source (ALS) synchrotron.

$$CH_4 + \gamma \rightarrow CH_4^{+*} + e^-_\gamma$$
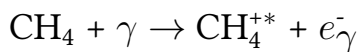
Once the photon has been absorbed, and the photoelectron ejected, the molecule is left in an excited state. Excited molecules have a high propensity to relax into a lower energy state and there are several processes that allow this to happen. Perhaps, the simplest method is for one of the valence electrons to transition into the core hole, created by the photoelectron ejection, by emitting a photon with its surplus energy. The other method is for one valence electron to fill the core hole and another valence electron to be ejected with the excess energy. This ejected electron is called an Auger electron. In methane, the Auger process is much more likely than the photon process. It is actually possible that more that one Auger electron is ejected. Once the Auger electron(s) have been emitted, the molecule is almost always on a repulsive curve, which eventually leads to the molecule breaking up into multiple ionic fragments.

To measure the molecular breakup and photoelectron, we use cold target recoil ion momentum spectroscopy (COLTRIMS), which is an experimental technique that allows us to measure the impact position and time of flight (tof) for each charged particle. This type of apparatus uses electric fields to push the electrons and ions to their respective detectors. A simplified diagram is shown in Fig. 1.1. After the impact positions and times have been recorded along with the photon's time, the initial momentum vectors can be calculated.
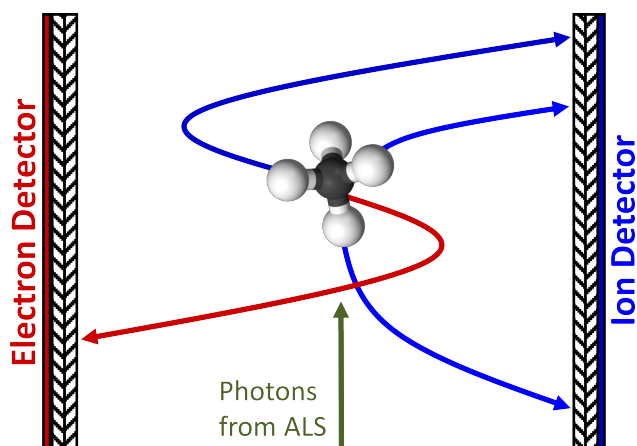
Figure 1.1: Simplistic diagram of the COLTRIMS apparatus. A static elecetric field between the detectors directs the fragments to their respective detectors.

The preparation for the experiment that eventually led to this dissertation took place in the summer of 2010 at Lawrence Berkeley National Laboratory. We started by simulating the apparatus to optimize the length of each region in the spectrometer, along with the field strengths needed in each region. The spectrometer was assembled with the attached particle detectors and tested with an alpha source. The simulation, construction, and testing is a rather short process, which took about a month. This short time frame is only possible because the vast majority of the apparatus does not have to change from one experiment to another. The entire experiment takes less than two weeks. In that two weeks half a terabyte of data was recorded on methane. This led us to the largest and most difficult step of the process, which is the analysis of the data. The analysis took us more than a year to complete. A large part of this time was spent in an attempt to calibrate the data. There are many different facets to calibration and a proper order in which each one should be addressed. This is covered in greater detail in Chapter 3.

The experiment and all of data analysis work has led us to the creation of the first three dimensional Molecular Frame Photoelectron Angular Distribution (MFAPD). MFPADs are a sensitive probe of the molecular structure and electronic state of the molecule. This work draws upon more than a decade of COLTRIMS work in diatomic molecules, which we have extended to polyatomic molecules. With diatomic molecules it is possible to fix the molecule in space and examine the two dimensional MFPADs[1,2]. We found that methane dissociates promptly, which lead to the initial momentum vectors of the hydrogen ions being along the bond axis. This prompt dissociation allows us to determine the molecules three dimensional orientation in an a posteriori fashion. These measurements, whether performed on diatomic or polyatomic molecules, are a useful tool for understanding molecular dynamics. The molecular dynamics of methane are explored in detail in Chapter 5.

1.2 Alternative Experimental Techniques

COLTRIMS paired with a synchrotron radiation is not the only method available capable of studying polyatomic molecules and molecular dynamics. There are several different alternative techniques. These methods include adiabatic and nonadiabatic molecular laser alignment, crystallography, intense field photon pulse from high harmonics or free electron lasers (FEL), and velocity map imaging (VMI). Often researchers will combine several of these techniques in one experiment depending on the goals of the experiment.

1.2.1 Velocity Map Imaging

VMI is a powerful experimental technique that uses Einzel lens fields in the spectrometer to focus ions or electrons. The lenses are setup in a manner that makes any particles with the same 2D (in the particle detector's plane) velocity vectors land in the same position on the particle detector[3]. This means that any two particles with 2D initial velocity vectors of the same

magnitude will land at the same radius on the particle detector. The main draw back to this approach is that, at least in the normal configuration, the third dimension of the velocity, in the time of flight direction, is not measured. VMI is often configured in a manner so the tof is compressed into a very short time frame for all the particles, which makes it difficult to measure tof accurately. This technique is thus often used in situations where tof would not be measurable, because of other experimental constraints. These constraints may include ionization sources that do not have a suitable time structure (i.e. no timing structure at all or a structure that is shorter than the particle tof), or are too intense and would thus flood the particle detectors. Under the limited condition that the particles initial momentum distribution is cylindrically symmetric, the third dimension can be reconstructed through the use of an inverse Abel transform[4]. There are also certain conditions, like the ability to rotate the photon polarization arbitrarily, that may make it possible to reconstruct the third dimension[5]. VMI's general inability to measure three dimensional momentum distributions makes it a poor candidate for measuring MFPADs.

1.2.2   Laser Alignment

Laser alignment methods are particularly useful for measuring MFPADs. In adiabatic, or long pulse, laser alignment the target molecule is fixed or aligned in space before being ionized. The electric field of the laser acts upon the dipole moment of the target molecule which causes a torque on the molecule. Here it is important to note the molecule does not need to initially possess a dipole moment only a anisotropic polarizability. The intense laser field induces a dipole moment in the molecule that then aligns the molecule. Friedrich et al. states "The anisotropy arises from the induced dipole moment and creates pendular eigenstates, directional hybrids of the field-free rotational states, in which the molecular axis librates about the electric field vector."[7] Through the use of elliptically polarized laser light, molecules with an anisotropic polarizability can be aligned in three dimensions. With the addition of a weak static electric field the molecule can
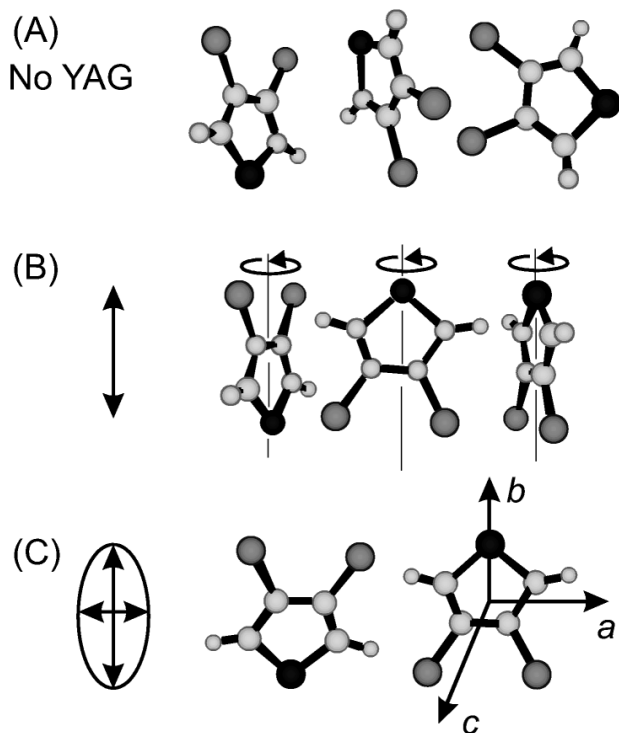
Figure 1.2: Figure and caption from Stapelfeldt[6] et al.: Illustration of the orientational distribution of 3,4-dibromothiophene (black circles:sulfur, dark grey circles: bromine) molecules for the following: (A) No alignment field present; all orientations are equally likely. (B) A linearly polarized alignment field. The symmetry axis is aligned along the space-fixed axis defined by the alignment field but the molecules are free to rotate around this axis. (C) Elliptically polarized alignment field. All three molecular axes are forced into alignment. The principle inertia axes a,b,c are superimposed on the bottom right model.

also be orientated, i.e. the dipole moment can be fixed in the lab frame. This alignment process is illustrated in Fig. 1.2.

One limitation to this technique is that molecules with an isotropic polarizability can not be aligned in their ground state. Also, not all of the target molecules can be orientated. A recent paper by Stapelfeldt et al. achieved "at least 80%"[8] orientation of the target molecules. Another issue with adiabatic laser alignment is that the molecules only remain aligned as long as the laser field is on[9], which means any measurement carried out is done so while the molecule is bathed in an intense field. While nonadiabatic, or short pulse, laser alignment would solve the field free problem, it cannot currently align and orientate molecules in 3D, at least to the author's knowledge.

1.3   Experimental Challenges

While there are multiple alternative technologies that can measure MFPADs and study molecular dynamics, COLTRIMS is particularly well suited. COLTRIMS is capable of measuring 3D momentum vectors of each and every charged particle created from the ionization event. But measuring every charged particles momentum vector is not a trivial task, and in the case of four and five fold coincidence measurements, like the one necessary here, requires a bit of luck. The calibration, discussed in Chapter 3, alone took many months. There are many challenges that must be addressed to produce useful measurements, such as identifying the fragmentation channel, multi-hit position corruption, and detection inefficiencies to name a few.

1.3.1   Channel Identification

$$CH_4 + \gamma \rightarrow CH_4^{+*} + e_\gamma^-$$

$$\rightarrow CH_3^+ + H^+ + e_\gamma^- + e_{Auger}^-$$
$$\rightarrow CH_2^+ + H_2^+ + e_\gamma^- + e_{Auger}^-$$
$$\rightarrow CH_2^+ + H^+ + H^+ + e_\gamma^- + 2e_{Auger}^-$$
$$\rightarrow CH_2 + H^+ + H^+ + e_\gamma^- + e_{Auger}^-$$
$$\rightarrow H^+ + H^+ + H^+ + CH^? + e_\gamma^- + 2e_{Auger}^-$$
$$\rightarrow CH^+ + H^+ + ?H_? + e_\gamma^- + e_{Auger}^-$$
$$\rightarrow C^+ + H^+ + ?H_? + e_\gamma^- + e_{Auger}^-$$
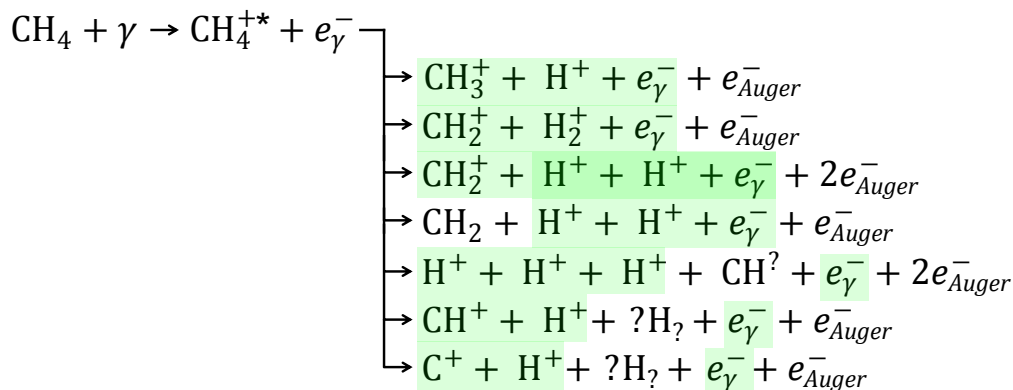
Measured fragments from each channel

One of the first challenges that must be overcome is simply to sort all of the possible fragmentation channels produced in this experiment. Some fragmentation channels we observed in the experiment are listed above. One of the easiest methods to identify a fragmentation channel is to examine the photo-ion photo-ion tof coincidence (PIPICO) plot. A PIPICO plot is a histogram of the tof for the first ion to hit the detector vs. the tof for the second ion to hit the detector. In the case where the methane molecule breaks up into two fragments, the PIPICO plot allows us

to sort some fragmentation channels, but in general, it allows us to see correlation between the first and second hit ions.
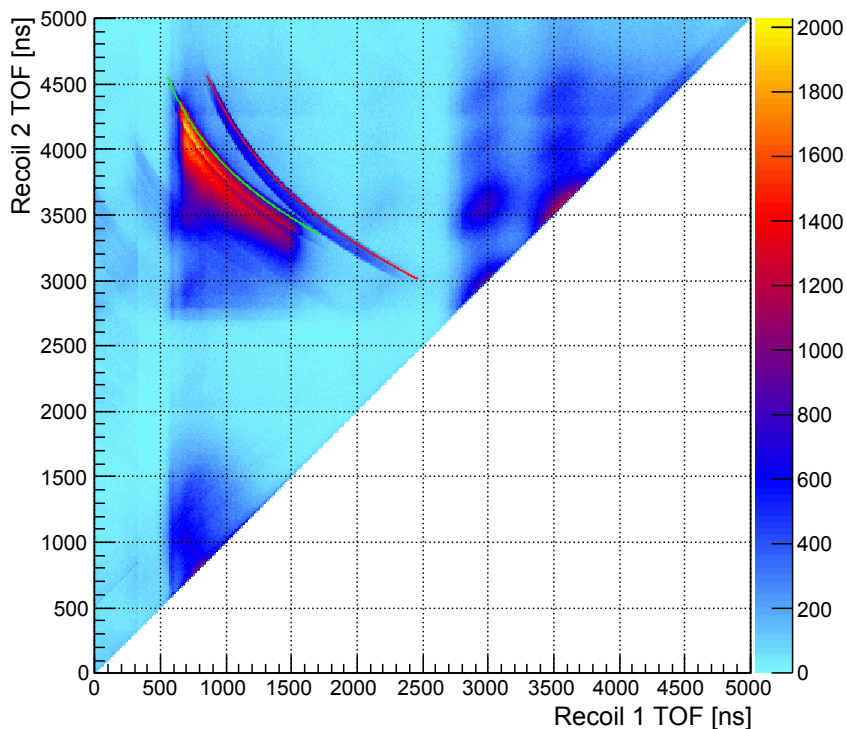
Figure 1.3: Raw photo-ion photo-ion coincidence plot. Simulated PIPICO lines are shown on top of the experimental data. The green curve represents the simulated CH_3^+ and H^+ channel and the red curve represents the simulated CH_2^+ and H_2^+ channel.

Figure 1.3 shows many reaction channels, but, for instance, examine the superimposed red line. This red line is a simulation predicting the position on this plot of the CH_2^+ and H_2^+ channel. The corresponding experimental data is visible as a blue stripe. This channel in the PIPICO plot is nicely separated form the adjacent channels and is therefore easily sorted, but now examine the green line, which is the predicted position of the CH_3^+ and H^+ channel. This channel in the PIPICO plot is not separated from the other channels, which can make it much more difficult to isolate.

To overcome this problem, we used a 3D momentum conservation algorithm, which is included in Appendix E. This algorithm takes the mass of the two particles (1 amu and 15 amu in this case) and fields in the spectrometer and calculates the momenta of every particle. Then it
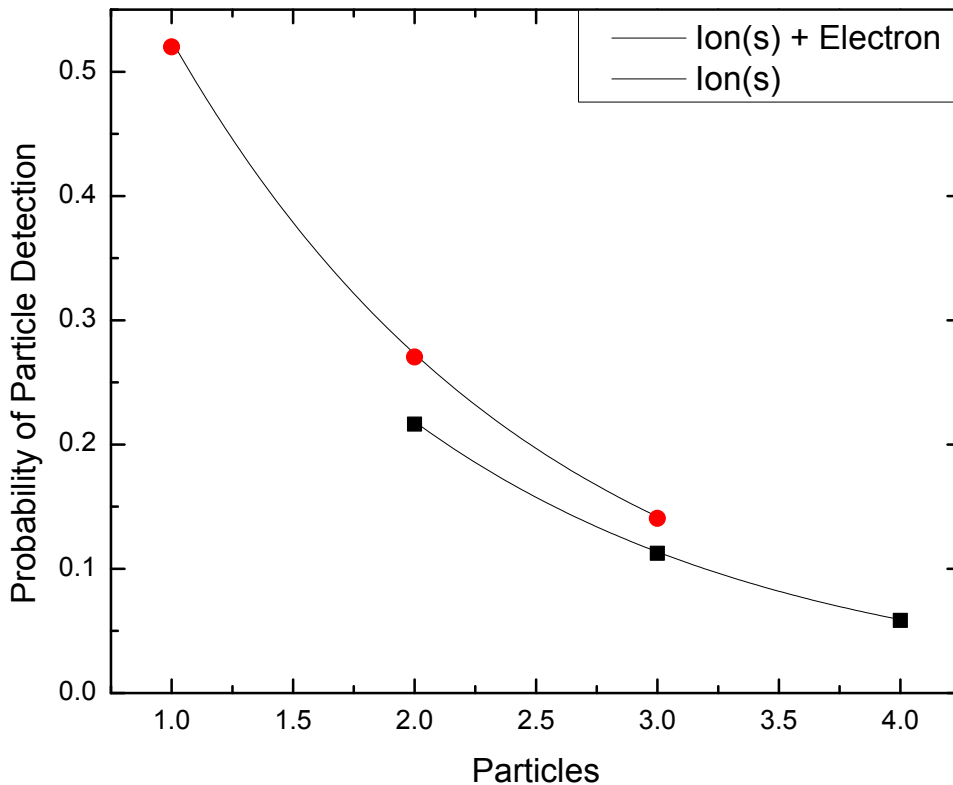
Figure 1.4: Probability of particle detection in our apparatus.

checks to see if the momentum for each particle sums to zero, or at least to a value close to zero. This algorithm is also implelmented for the three body breakup channel of CH_2^+ , H^+ , and H^+ . This routine allows us to sort and label each event into their corresponding reaction channels. It also greatly reduces the number of random coincidences in each channel.

1.3.2   Multi-hit Challenges

The delay line anodes we use to detect particles are multi-hit capable, but they do not always work perfectly. This leads us to another challenge. Under certain conditions, the detectors can fail to correctly measure two incident particles. Usually this happens when the two particles land

close together in time and position. But, fortunately, the detectors are an overdetermined system, and therefore in these situations, it is usually possible to reconstruct what actually occurred. This is accomplished through the use of a proprietary DLL routine that is supplied to us by Roentdek. The reconstruction routine contains 21 different methods to reconstruct missing position and time data.

1.3.3 Detection Inefficiencies

Another example of experimental challenges involved in this study is low detection particle probability. Our apparatus has multiple wire grids that ions and electrons must pass through. The grids are necessary to define the electric potential in the apparatus. However, each grid has ∼80% open area, or only 80% of the incident particles are transmitted. Micro-channel plates in the detectors have ∼65% open area. In our apparatus, this leads to ∼5% detection probability for the five fold coincidence (counting the photon as one particle) probability as shown in Fig. 1.4. To combat this low detection probability we simply increases the time spent acquiring the data along with increasing the photon flux.

1.4 Molecular Structure and Symmetries of Methane
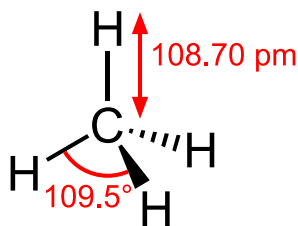
Figure 1.5: Cram diagram of Methane [10]

Methane is composed of a carbon atom bonded to four hydrogen atoms. The equilibrium angle between two adjacent hydrogen atoms is $109.47°$ as given by the molecule's symmetry, as shown in Fig. 1.5. The molecule has tetrahedral symmetry and therefore belongs to the T_d

point group. It is important to remember all four hydrogen atoms are indistinguishable from one another.

(a) A Single C_2 Symmetry Axis

(b) All Three C_2 Symmetry Axes
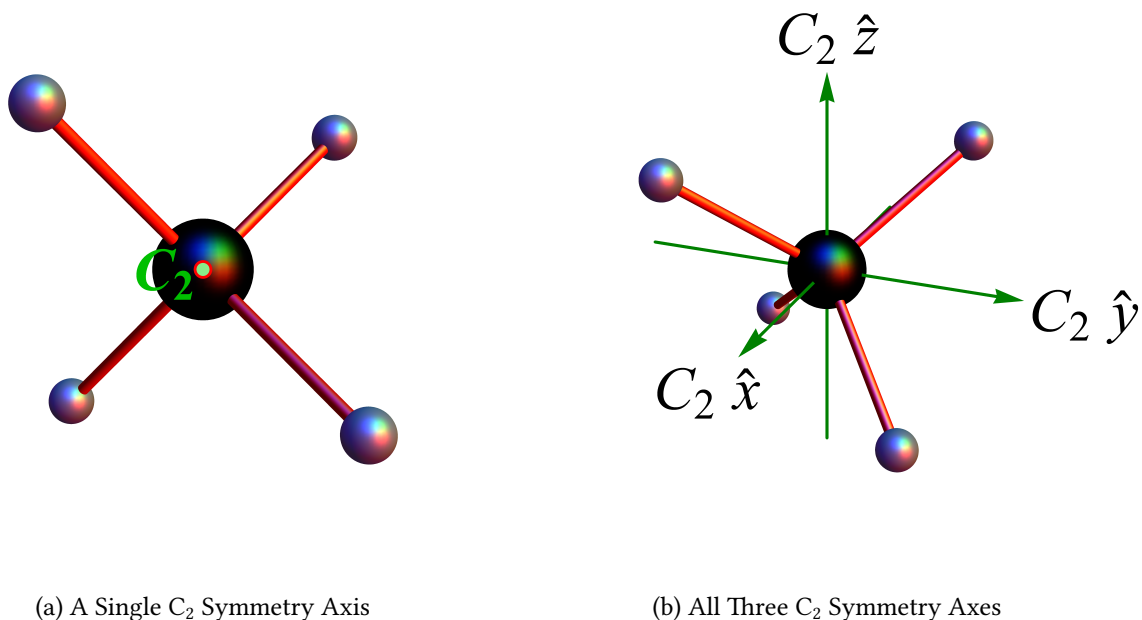
Figure 1.6: Methane's C_2 symmetry axes.

The first symmetry operation we will examine is the C_2 rotation symmetry axes. In general, a n-fold rotation is denoted by C_n, where the angle of rotation is $2\pi/n$ radians about an axis. This angle is the smallest angle by which the molecule can be rotated, about a particular axis, which will return it to an orientation indistinguishable from the original orientation. It is clear that if you rotate, about the green (outlined in red) axis that is normal to the page, the molecule in Fig. 1.6(a) by 18Ø° it will be indistinguishable from its original orientation. Methane has three C_2 axes, which are all orthogonal to one another. This results in a "natural" molecular coordinate system, which was heavily utilized in the analysis of the experimental data.

Methane also has four C_3 symmetry axes. This can be seen in Fig. 1.7(a), where a rotation of 12Ø° about the green (outlined in red) axis will return it to the same orientation. These C_3 axes are all located along the C-H bonds, which can be seen in Fig. 1.7(b). In methane, the C_3 axes are the principle axes, but in general it is the C_n axis with the largest n.
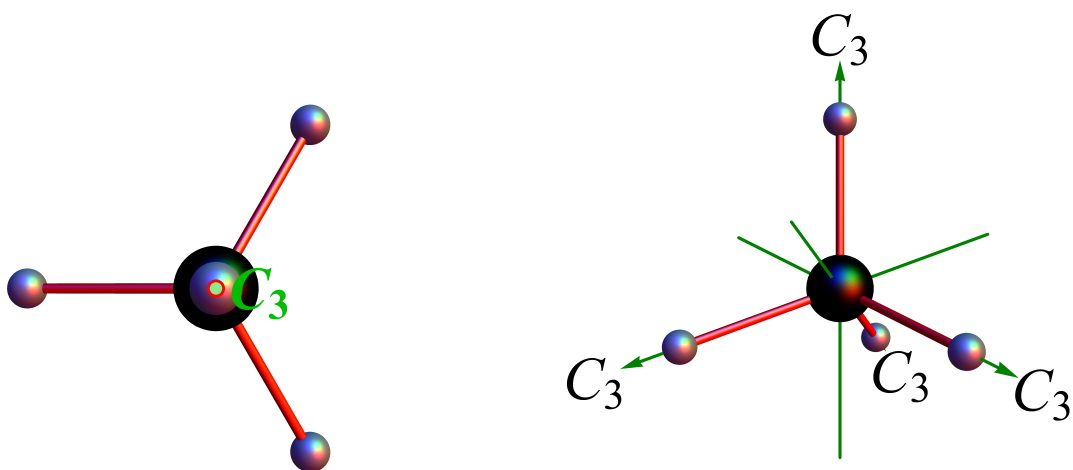
(a) A Single C$_3$ Symmetry Axis

(b) All Four C$_3$ Symmetry Axes

Figure 1.7: Methane's C$_3$ symmetry axes
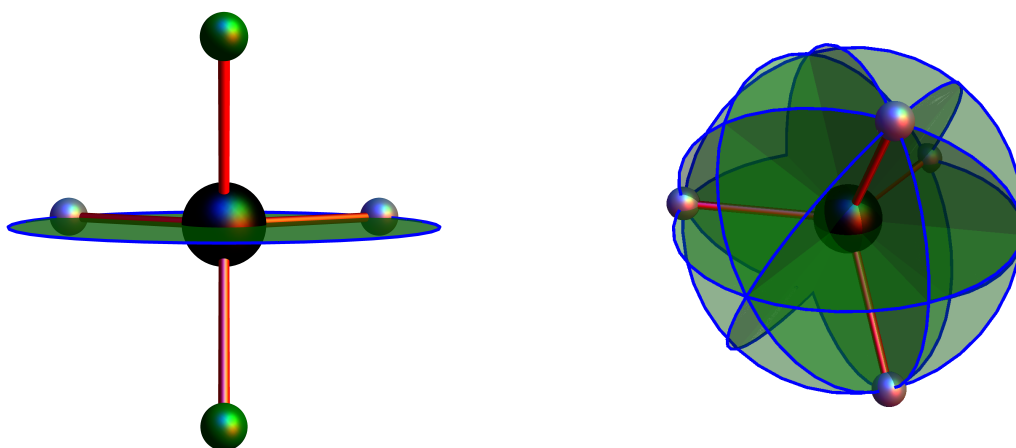
(a) A Single Reflection Plane of Symmetry

(b) All Six Reflection Planes of Symmetry

Figure 1.8: Methane's σ_d symmetry planes

Methane has another type of symmetry operation, which is reflection. Methane has six planes about which it can be reflected and remain in an indistinguishable orientation. A single
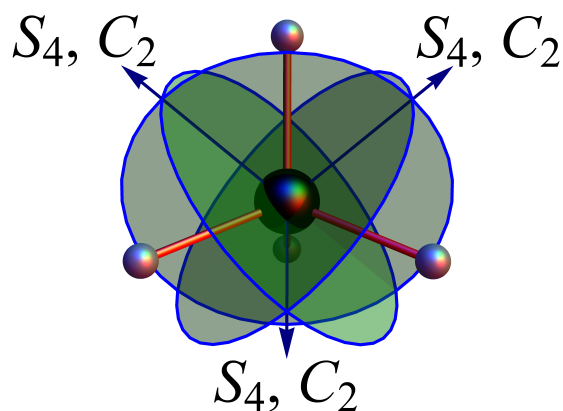
Figure 1.9: Methane's S_4 symmetry axis

plane has been shown in Fig. 1.8 (a); it is obvious that a reflection through the green plane will leave the molecule in the same orientation. With methane these symmetry operations are denoted by σ_d. The d in σ_d identifies it a dihedral plane, which is a plane that contains the principal axis and bisects the angle between two C_2 axes.

The last symmetry operation for methane is the so called improper axis of rotation or more sensibly called, though much less often, a rotary reflection. This symmetry operation is denoted by S_n and consists of a C_n operation followed by a σ operation. In the case of methane, the operations that make up the S_4 operation are valid symmetry operations when carried out separately. The n in S_n is the same as the n in C_n. Thus, in methane, the S_4 operation is a rotation about one of the C_2 axes by $90°$ and then a reflection through the plane defined by the two other C_2 axes. The S_4 axes and reflection planes can be seen in Fig. 1.9.

1.5 Background

The study of methane via photoionization has a long history going back to at least 1954[11,12] with the first K-shell measurement appearing in 1964[13]. This first K-shell measurement by A.P. Lukirskii is shown in Fig. 1.10. The vertical C 1s core ionization energy is 290.844[15], which can be seen in Fig. 1.11.
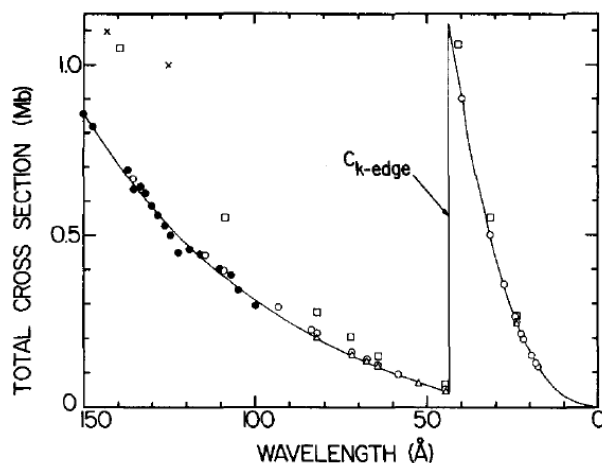
Figure 1.10: Mehtane 1s cross-section as compiled by D. A. L. Kilcoyne et al.[16,17] Data from Lukirskii et al.[13] is shown as square.

(a) From L. J.Sæthre et al.[18]

(b) From V. Myrseth et al.[15]

Figure 1.11

13
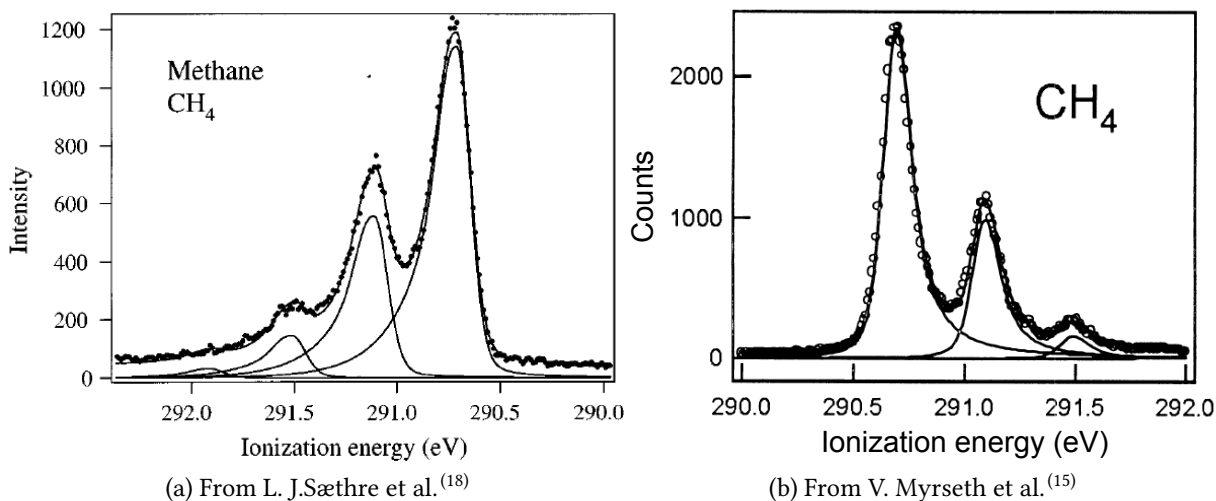
The other major feature visible in Fig. 1.11 is the vibrational structure of methane. This structure has been observed by many other researchers[19,20,21]. These peaks appear to be the excited states of the symmetric stretch normal mode, which is listed as mode 6 in Appendix C. Kukk et al.[21] found the Franck-Condon principle is violated as the photoelectron energy is increased. This leads to the excitation of the asymmetric stretching and bending vibrational modes.

Ueda et al. investigated the electronic state dependence of ions production in the k-shell ionization of methane[22]. The particular initial state dependence of the dication is mapped to the final ions produced. This is shown in Fig. 1.12. This measurement became particularly important to the work presented here by illuminating the fact that CH_3^+ and H^+ fragmentation channel is only produced by the ^1E state.
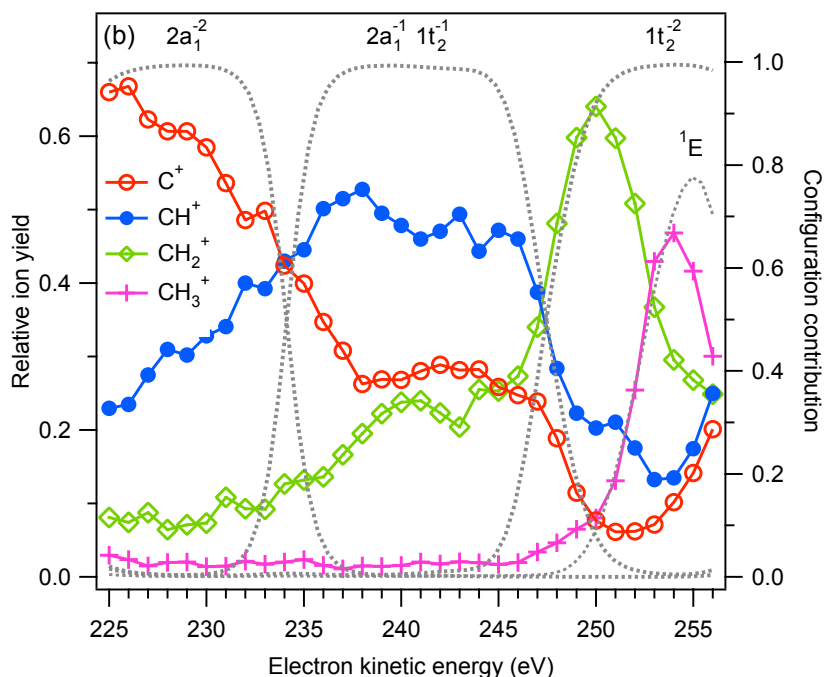
Figure 1.12: Initial Electronic State Dependence on Dissociation Pathway from Ueda et al.[22]

14

1.5.1 Molecular Frame Photoelectron Angular Distributions

Over the last decade MFPAD has seen remarkable growth as a tool for understanding molecular dynamics, and thus has generated much interest in the atomic and molecular physics community. Many papers have now been published containing MFPADs for diatomic molecules[23,24,25,26] and even polyatomic[27,28,29] molecules. At lower photon energies, MFPAD are very sensitive to the molecular potential.

Yagishita et al. claims to have measured the 3D MFPAD of H_2O at 14eV above the O 1s threshold[30]. They measured the momentum vectors of the ions directly in three dimensions, but the photoelectron momentum is only measured in two dimensions (VMI). This VMI measurement, while useful, is difficult to convert to a three dimensional distribution, but it can be converted in at least a couple of circumstances. One of these circumstances is if the distribution is known to possess a certain azimuthal angular dependence.

In the Yagishita water paper, they cite one of their previous papers to explain the experimental and data analysis methods used. In that paper, they introduce a improved peeling method[a], which they state "Since the azimuthal angle dependence is known, we can peel the photoelectron images in coincidence with ion pairs"[31]. Essentially, if the azimuthal dependence of the distribution is already known, then it is possible to "reconstruct" the three dimensional distribution.

For this 3D MFPAD measurement on water, the polarization axis is selected to bisect the angle between the two hydrogen atoms. For this alignment, they state that "the symmetry of the photoelectron wavefunction is restricted to a_1 due to the dipole selection rules"[30,32]. They do not state how they determined the photoelectrons azimuthal angle dependence. Perhaps they used the wavefunction's azimuthal angle dependence, but this is pure speculation as this important detail is missing. In any case they appear to have the requirement of knowing the answer in advance before they are able to "measure" the MFPAD.

---

[a]The peeling method is a numerical inverse Abel transform.

1.6 Dissertation Summary

The next chapter of this dissertation covers the general experimental technique used in these measurements. These measurements start with soft X-ray photons produced by the Advanced Light Source. Photons interact with our supersonic gas jet target and produce core ionized methane molecules and photoelectrons. Charged fragments trajectories are directed toward detectors by electric and magnetic fields. The charged particles are detected using micro-channel plates and delay line anodes, which allows us to measure the time of flight for each particle and the position of where each particle impacts the detectors. A large and complex part of the experiment is actually software, much of which is custom written for each experiment.

Chapter 3 covers the lengths to which we went to calibrate the data. The first task was to calibrate the energy of the photon used in this experiment, which was accomplished through the use of the N_2 (N $1s \rightarrow \pi^*$) Rydberg line. The time of flight for all particles were adjusted to correct for signal delays in the acquisition electronics. To correctly calculate the initial momentum of each fragment, the center of mass motion of the fragments must be determined. To do this, we measured the velocity of the supersonic gas jet, which is then subtracted off in the momentum calibration. It was also necessary to orientate both detectors so they share a common coordinate system. The electric and magnetic fields are set during the experiment, but only roughly. This can be calibrated using the data by simulating the time of flight of each fragment in the two ion coincidence channels. The spectrometer we used also contained an electrostatic lens, which must be controlled for.

Chapter 4 show the primary results of this experiment. In this chapter we present a method for measuring the molecular structure of methane using a core level photoelectron. This result arises from the propensity of the photoelectron to be ejected along the hydrogen bonds. We are also able to compare these measurements to theoretical calculations of the MFPAD, which are in good agreement.

Chapter 5 examines the fragmentation channel of H^+ and CH_3^+ . Only one initial dication, the ^1E state, results in the production of these fragments, but the ^1E state goes through a conical intersection with the $^1A_1$ state. These two states lead to different Kinetic Energy Release (KER), which allow us to differentiate the two states in the experimental data. The evidence for there being two different states involved is greatly strengthened through the use of MFPADs.

Chapter 2

Apparatus

"A large part of mathematics which becomes useful developed with absolutely no desire to be useful, and in a situation where nobody could possibly know in what area it would become useful; and there were no general indications that it ever would be so. "

—John von Neumann

2.1 Coltrims Apparatus Overview

Over the last two decades cold target recoil ion momentum spectroscopy (Coltrims) technique has become a powerful tool to understand atomic and molecular dynamics[33,34] . The Coltrims apparatus has evolved in complexity and ability. The result of this evolution is the modern Coltrims apparatus, which is the focus of this chapter. The Coltrims apparatus is complex and as with any complicated system the setup and calibration becomes time consuming and difficult. The experimental apparatus is pictured in Figure 2.1 and Figure 2.2.

In this experiment, and most Coltrims experiments, the target was a supersonic gas jet. The gas jet produces a cold localized target. The supersonic gas jet target rises vertically out of the floor of the vacuum chamber. A pulsed soft x-ray photon beam intersects the gas jet in basically the center of the spectrometer. This intersection of the photon beam and supersonic gas jet is referred to as the interaction region. If a photon is absorbed by a methane molecule then an electron will be ejected from the molecule. This first electron is referred to as the photoelectron.
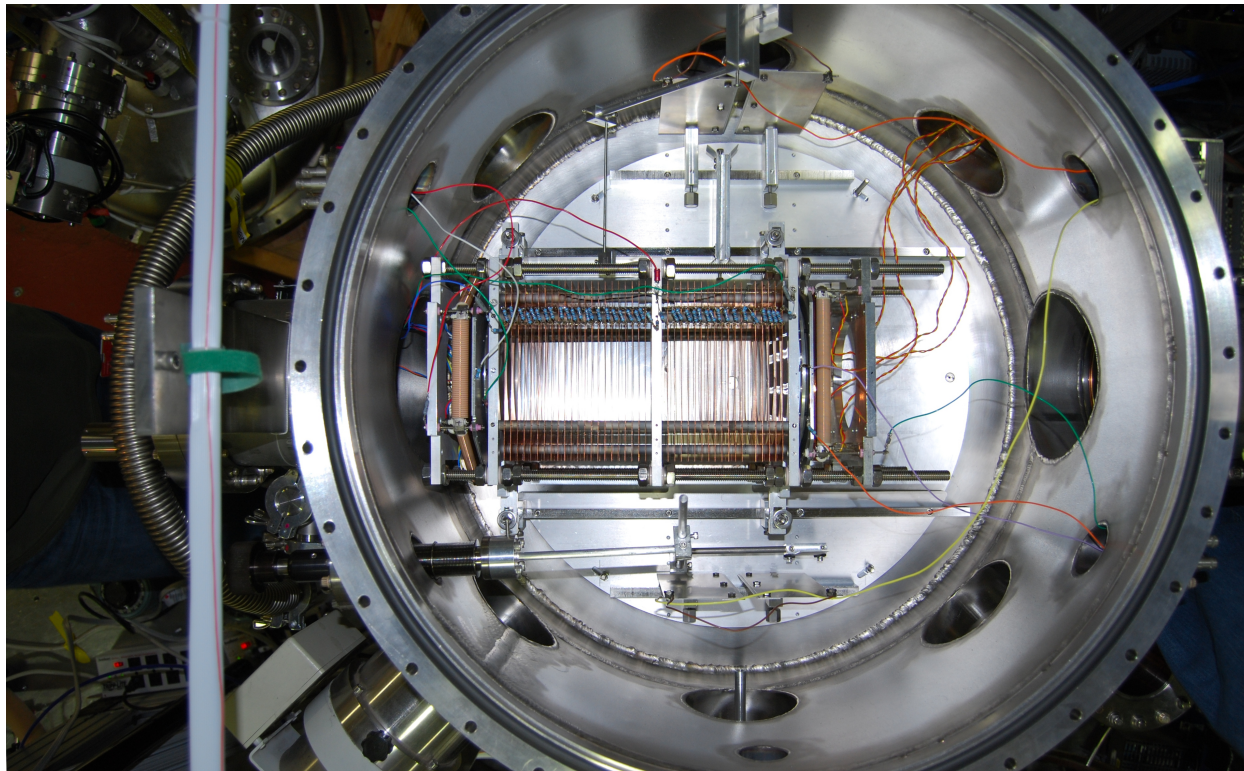
Figure 2.1: Picture of the COLTRIMS apparatus used for this experiment. Visible in the center of the chamber is the spectrometer with the detectors attached to each end to the spectrometer.

The carbon 1s vertical ionization threshold in methane is $I_c = 290.844\text{eV}$ [15] In our experiment, the photon's energy is tuned to be just above this threshold. This ensures the probability of removing the 1s carbon electron is vastly greater the any other electron. The molecule usually then undergoes an Auger decay, which results in an excited doubly charged methane molecule. The molecule can also undergo a double Auger decay, though this is much less probable. There is also a small probability that a stable CH_4^+ cation is formed. The dication and trication states are unstable, which causes the molecule to fragments into two or three pieces.

In the center of the COLTRIMS apparatus is the spectrometer which consists of copper and aluminum plates and grids. The spectrometer has a series of evenly spaced plates that are connected electrically to one another through resistors. The plates and resistors are visible in Fig. 2.1. The purpose of the spectrometer is to produce an electric field which will force the ions and
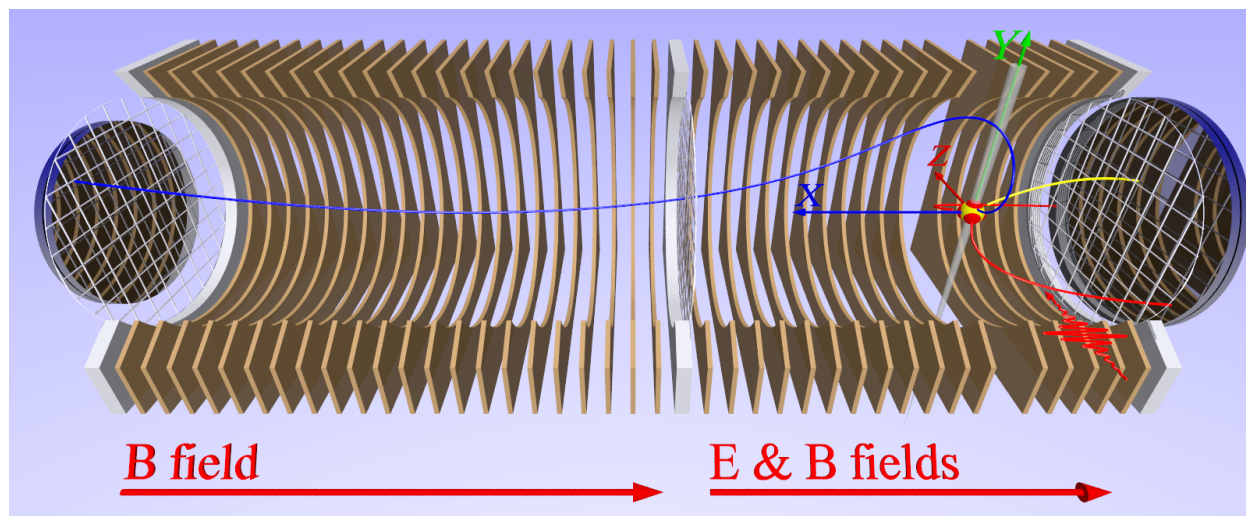
Figure 2.2: Schematic of the COLTRIMS spectrometer. The ionic fragments' flight paths are shown in yellow and red. The photoelectron's flight path are shown in blue. On each end of the spectrometer there is a position sensitive charged particle detector.

electrons toward the detectors. When different voltages are applied to the ends of the spectrometer it produces a uniform electric field inside the spectrometer [a]. There are also two large coils, not visible here, on the outside of the chamber. These coils are in a Helmholtz coil configuration. When current is passed through the coils, it produces a uniform magnetic field that is parallel to the electric field. This magnetic field is present throughout the entire spectrometer and is parallel to the electric field.

Once the excited molecule has broken up into fragments, which are often all charged, the photoelectron and ionic fragments are accelerated toward position sensitive detectors. The acceleration towards the detectors is caused by the electric field. The electrons are often too energetic to be contained inside of the spectrometer by the electric field alone. If the electric field was the only force acting on the electrons they would often fly out of the spectrometer, in which case we would be unable to measure them. We would, of course, prefer to measure a $4\pi\ \Omega$ of solid angle on the photoelectrons. A magnetic field, parallel to the electric field, is used to achieve this. Electrons emitted in a direction not parallel to the electric field are accelerated in a fashion that

---

[a]This is not entirely true, please see Chapter 3.

causes them to have a helical trajectory, given by the Lorentz force. The strength of the magnetic field is tuned so that the photoelectrons are all collected.

Once the electrons and ion have been pushed to their detectors, they are measured using micro-channel plates and delay line anodes. Micro-channel plates (MCP) are used to amplify the signal of a single electron or ion into a signal that is measurable by solid state electronics. The MCP also allows us to measure the impact time of the incident particle. The delay line anode is used to measure the incident particle's position.

To reduce confusion, the word "event" will be used to describe all of the particles that are ejected after the molecule has absorbed the photon. The word "hit" will be used to describe a particular fragment or electron that is collected by their respective detectors. The experiment data is recorded in list mode, which means for a single event (one photon colliding with a methane molecule) the computer records the time of flight (TOF) and the position on the detector for the first hit, then the second hit, et cetera on the ion detector and then does the same for however many electrons hit the electron detector. We observed seven different ways (with significant probabilities for each) for methane to fragment in this experiment. The list mode nature of the data is one of the major advantages of COLTRIMS , because we are able to replay the experiment and select only the events of a particular type. For instance, we could select only those events including two protons and a CH_2^+ fragments. It would otherwise be impossible to examine this particular fragmentation channel in detail, because it comprises only about two percent of the collected events.

2.2   Soft X-rays

Photons were produced by the Advanced Light Source at Lawrence Berkeley National Laboratory (LBNL). Beam line 11.0.2 was used to make the linearly polarized photons[35]. This experiment was performed at the ALS, shown in Fig. 2.3, located in Lawrence Berkeley National

Figure 2.3: Advanced Light Source at Lawrence Berkeley National Laboratory overlooking the San Fransisco Bay[36].

Laboratory. The ALS is a third generation synchrotron, which uses 1.9GeV electrons to produce x-rays. These electrons travel at 99.999996% of the speed of light. The synchrotron consists of a storage ring, with straight sides, that the electrons travel around in. When the electrons come to the end of a straight section their trajectory is bent via a magnetic field. There are a number of technologies deployed at the ALS to produce x-rays: bending magnets, superbends, wiggler, undulator.

A schematic of Beamline 11.0.2 is shown in Fig. 2.4. This beamline uses a 5-cm-period elliptical polarization undulator. The undulator allows the user to select the energy and polarization of the x-ray light. Inside the undulator, there is a series of alternating magnets. There are four of these magnet series in the undulator. Electrons travel though the gap between the four magnet series, which causes them to be accelerated back and forth. When any charged particle
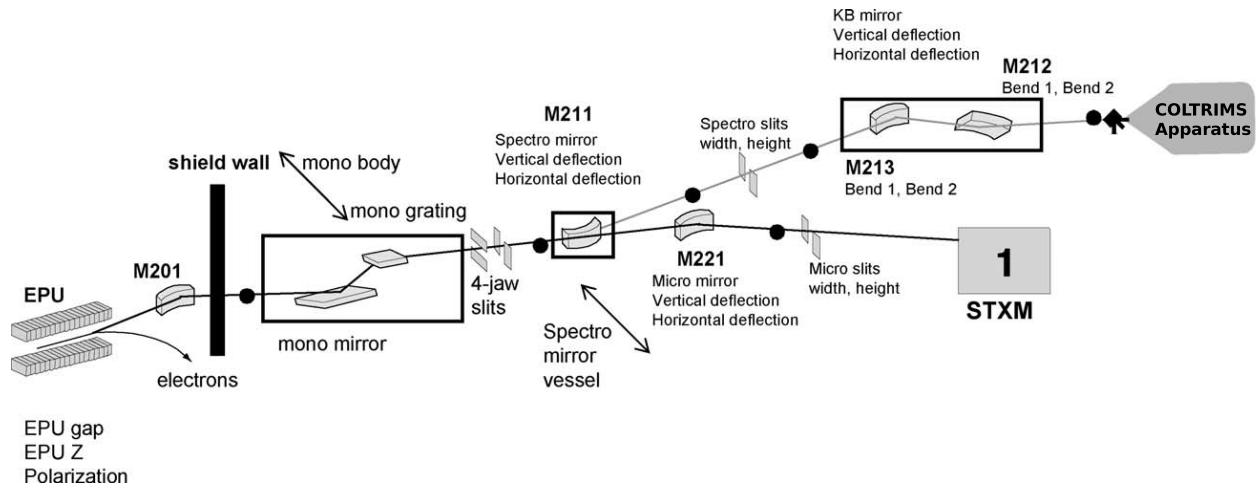
Figure 2.4: Schematic of Beamline 11.0.2 at the Advanced Light Source[35].

is accelerated it emits radiation. The undulator gap width is adjustable and determines the peak of the photons' energy distribution. After the x-ray light is produced in the undulator, the light passes though a monochromator, which is used to further refine the energy distribution. The monochromator has a 150 $^{\text{lines}}/_{\text{mm}}$ and a 1200 $^{\text{lines}}/_{\text{mm}}$ diffraction grating. Fig. 2.5 shows the flux output of the beamline with the different diffraction gratings and harmonics.
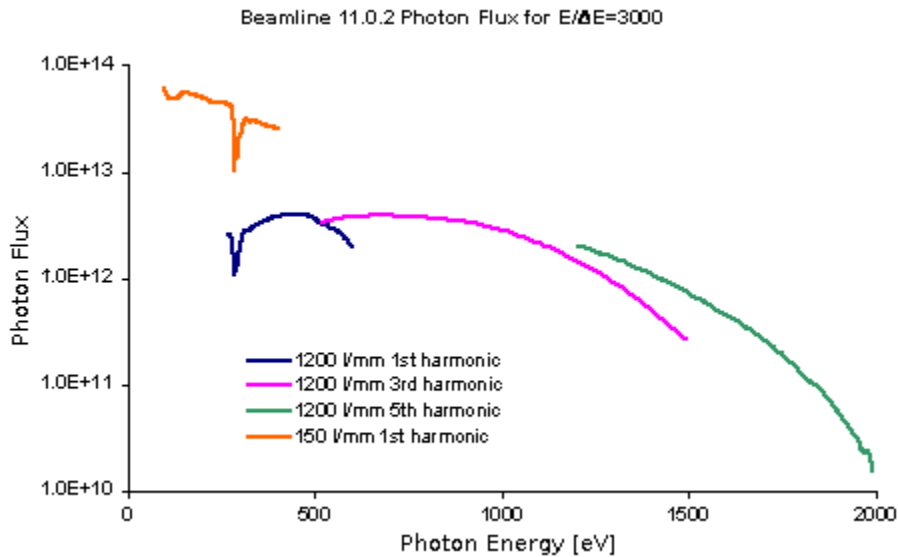
Figure 2.5: Beamline 11.0.2 Photon Flux.

23

After the photons are diffracted off of the diffraction grating, they pass though the exit slits. These slits are adjustable and define the energy resolution and the photon flux. The slit gap is always a compromise between the resolution and flux needed for the experiment, but for this experiment the energy resolution was not critical. The exit slits were set to 7.5 μm for the dispersive slits and 200 μm for the non-dispersive slits. The photon energy for this experiment was tuned to be just above the carbon k-edge (290.844eV for methane). The 150 $^{\text{lines}}/_{\text{mm}}$ grating was used to produce $\sim$295eV linearly polarized photons.

2.3   Gas target

Coltrims systems uses a supersonic gas jet for the gas target. This technique has two advantages. First, the target is localized in the spectrometer. This localization allows us to know the starting position of the ejected ions and electrons, which when combined with other information (final position, electric and magnetic fields, et cetera) allows us to calculate the initial momenta of the ions and electrons. The gas jet is about a millimeter in the interaction region. Second, the gas is cooled, through expansion, in the process of making the jet. Methane is cooled to the point that it is in the rotational and vibrational ground state.

A schematic of the supersonic gas jet system is shown in Fig. 2.6. The gas jet subsystem has four major parts: nozzle, skimmer, aperture, and jet dump. The nozzle is a 30μm diameter hole. A high pressure gas bottle containing methane is connect to a regulator. The regulator allows the experimenter to control the pressure on the back side of the nozzle, which is called the driving pressure. The driving pressure was $\approx$ 2atm. The gas then expands through the nozzle into the source vacuum chamber. The source vacuum chamber has an operating pressure of $\approx 10^{-4}$ torr. The gas is cooled through adiabatic expansion.

The nozzle sprays gas over a large area and thus many directions as shown in Fig. 2.6. Gas emitted in the vertical direction is allowed to pass through the skimmer. The skimmer consist
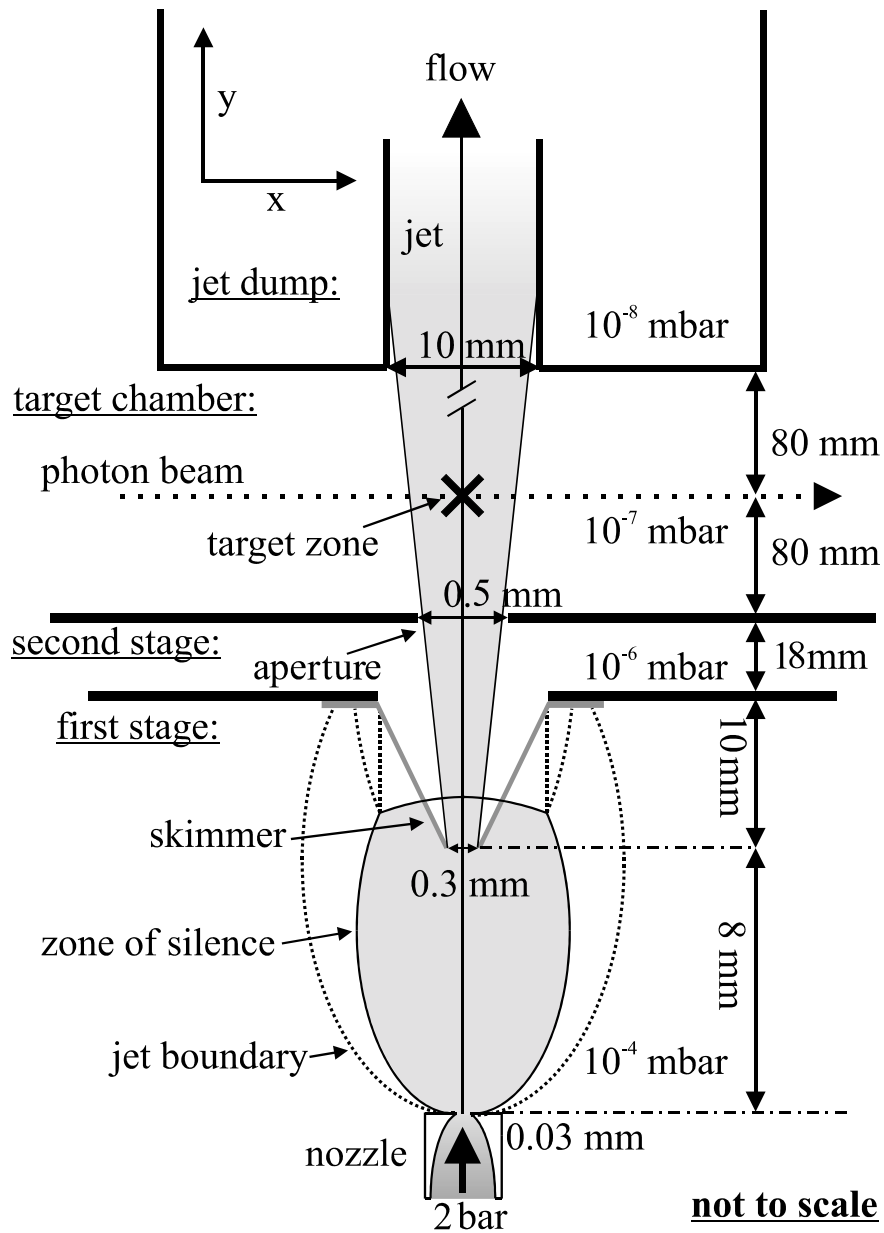
Figure 2.6: Diagram of the supersonic gas jet subsystem[37]. All values are approximate.

of a metal cone with a 300 micron hole at the apex, and is located about ≈8 mm directly above the nozzle. There is a high throughput turbo pump on the source vacuum chamber to remove the remaining gas. Gas that makes it through the skimmer and into the second stage vacuum chamber is traveling in a vertical or mostly vertical direction. The second aperture is ≈28 mm above the tip of the skimmer. The second aperture acts as second collimator of the gas jet. This further increases the speed ratio $\frac{V_{\text{veritcal}}}{V_{\text{perpendicular}}}$; since V_{veritcal} will remain constant $V_{\text{perpendicular}}$ must

25

Figure 2.7: The skimmer used in the gas jet system.

decrease. This lower $V_{\text{perpendicular}}$ means the gas target will be more localized in the interaction region.

Roughly 160 mm above the second aperture is the location of the jet dump. The jet dump is simply a tube with a small hole on the bottom end and a turbo pump on the other. The hole is approximately 1 cm in diameter. The purpose of the jet dump is to pump away the jet after it has left the interaction region. This allows the main chamber to more easily maintain a low pressure, which reduces the chance a photon interacting with a stray (not in the gas jet) methane molecule.

2.4 Electric and Magnetic Field

The electric field is produced through the spectrometer plates. Each plate in the spectrometer is electrically connected to the adjacent plates via resistors. The strength of the field is controlled by setting the potential on each end of the spectrometer and in the middle. This experiment used a 7.48 $^V/_{cm}$ field in the region between the ion side and the middle as shown in Fig. 2.8. This section of the spectrometer is called the acceleration region. The acceleration region is 10.56 cm long and the interaction region is located at about 3.33 cm from the ion side. The next section had a 0.0 $^V/_{cm}$ field and is referred to as the drift region. This drift region is 14.40 cm in length. This means the electron side of the spectrometer satisfies the Wiley-McLaren condition[38], which allows the tof of the electrons to be unaffected by the interaction region's thickness.

Between the acceleration region and the drift region, the electric field transitions from 7.48 to 0.0 $^V/_{cm}$. To ensure there is a sharp transition, and thus a uniform field in both regions, a metal grid is placed between the two regions. This grid has about an 80% open area, meaning only 80% of the particles will be able to pass through each grid. The MCP must be operated at a different potential than the spectrometer, so we must use grids at each end of the spectrometer, which further reduces the number of transmitted particles. This small space between each end of the spectrometer and the front of the MCP acts as an acceleration region, which helps the MCP trigger more efficiently. The electrons must pass through two grids, consequently only about 65% of the electrons make it to the detector. However, ions have only one grid.

The magnetic field is generated by a pair of Helmholtz coils located on the exterior of the chamber. These coils produce a uniform magnetic field in the spectrometer region. These coils are water cooled and can produce up to a 40 gauss magnetic field. The spectrometer is aligned on the same axis so that the electric field is parallel (or anti-parallel) to the magnetic field.

Alignment of the spectrometer and magnetic field is not perfect, but the mechanical misalignment shouldn't be more than about 5°. To compensate for this misalignment, there are two
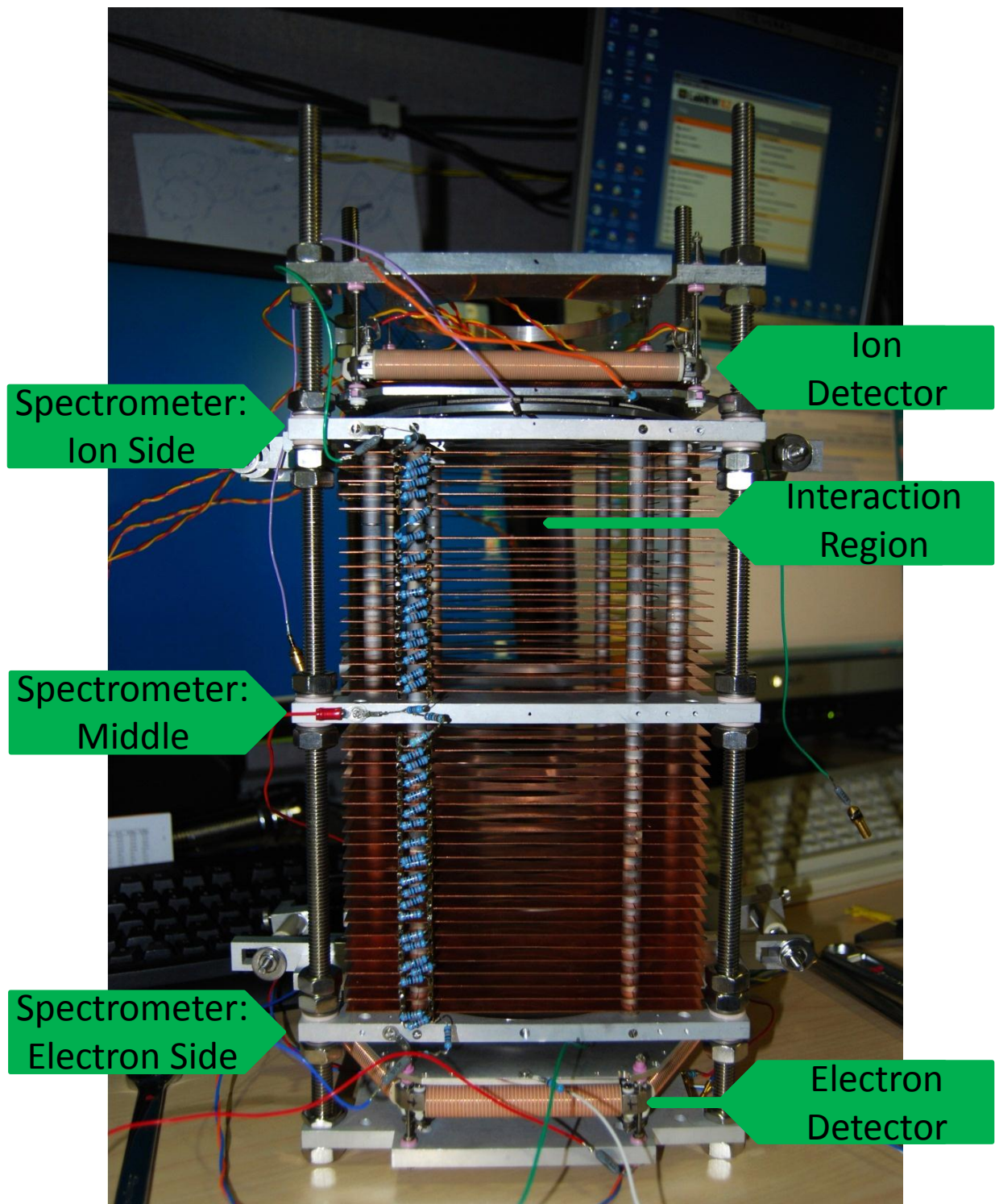
Figure 2.8: The Spectrometer with the square ion delay line anode visible on the top and the hex anode visible on the bottom.

sets of smaller coils positioned on orthogonal axes to the main Helmholtz coils. One set of trim coils are on the vertical axis and the other set is on the horizontal axis. These trim coils can only produce a few gauss, but this is more than what is necessary. With these trim coils, it is possible to align the aggregate magnetic field vector with the electric field vector; this is covered in more detail in Section 3.6.3.

One of the ultimate goals of this experiment is to be able to determine the initial momentum (momentum after being ejected from the molecule, but before being accelerated by the electric and magnetic fields) of each particle in three dimensions. To do this we must examine the effects of the electric and magnetic fields on a charged particle. This will allow us to find the necessary equation to determine the initial momentum in each direction. The force from an electric and magnetic field on a charged particle is given by the Lorentz force equation, which is

$$\vec{F} = q\left[\vec{E} + \vec{v} \times \vec{B}\right],\tag{2.1}$$

where $\vec{F}$ is the force on the particle, q is the charge on the particle, $\vec{E}$ is the electric field, $\vec{v}$ is the particle's velocity, and $\vec{B}$ is the magnetic field. If we let $\vec{E} = [E_x, 0, 0]$ and $\vec{B} = [B_x, 0, 0]$ then we get

$$\vec{F} = q\left(\vec{E} + \begin{vmatrix} \hat{x} & \hat{y} & \hat{z} \\ v_x & v_y & v_z \\ B_x & 0 & 0 \end{vmatrix}\right) = q\left(E_x\hat{x} + B_x v_z\hat{y} - B_x v_y\hat{z}\right) = m\vec{a}.\tag{2.2}$$

We can write the acceleration as

$$a_x\hat{x} = \frac{qE_x}{m}\hat{x}, \qquad a_y\hat{y} = \frac{qB_x}{m}v_z\hat{y}, \qquad a_z\hat{z} = \frac{qB_x}{m}v_y\hat{z}.\tag{2.3}$$

In examining Equation 2.3, it becomes obvious that if a charged particle has an initial velocity that includes nonzero $\hat{y}$ or $\hat{z}$ components then that particle will be accelerated in the $\hat{x}$ direction by the electric field and the magnetic field will cause the particle to follow a helical

trajectory toward the particle's respective detector. This magnetic field is used to confine the electrons inside the spectrometer and greatly increase the collection solid angle of the electrons. The magnetic field strength is set to collect a 4π solid angle on the photoelectron.

In order to determine each particle's initial $\hat{x}$ momentum in terms of time of flight, its necessary to rewrite the $\hat{x}$ component of the acceleration, Eq. 2.3, as

$$\dot{v}_x \hat{x} = \frac{dv}{dt}\hat{x} = qE_x\hat{x}. \tag{2.4}$$

Integrating Eq. 2.4 gives

$$P_x = mv_{ox} = (\frac{qE_x}{2}t^2 + x)/t, \tag{2.5}$$

which gives a time to momentum function for a single acceleration region. Here x is the length of the acceleration region, v_{ox} is the initial velocity, P_x is the initial momentum in the $\hat{x}$ direction, and t is the TOF. In this experiment, there were two acceleration regions for the recoils, and two acceleration regions and a drift region for electrons. Solving equation 2.4 for three acceleration regions of arbitrary length and field is not a trivial task. This difficulty was overcome by using Newton's method to solve equation 2.4. This numerical method is covered in more detail in Appendix D.

Returning to the motion of particles with nonzero initial velocity components in $\hat{y}$ or $\hat{z}$ directions we get

$$\dot{v}_z \hat{z} = \frac{qB_x}{m}V_y\hat{z}, \tag{2.6}$$

$$\dot{v}_y \hat{y} = \frac{qB_x}{m}v_z\hat{y}. \tag{2.7}$$

Using a time honored method of solving differential equations, guessing the answer, results in

$$v_z = V_{o\perp} Cos(\omega t + \phi), \tag{2.8}$$

$$v_y = V_{o\perp} Sin(\omega t + \phi), \tag{2.9}$$

where $V_{o\perp}$ is the magnitude of the two dimensional $(\hat{z}, \hat{y})$ initial velocity vector, and $\omega = {}^{qB_x}/m$ is the cyclotron frequency and ϕ is the phase angle or the angle in the $\hat{z}\hat{y}$ plane that the initial velocity was directed. Before integrating these equations, it is illuminating to expand the trigonometric functions in the following manner, which gives

$$\int \frac{dz}{dt} dt = \int V_{o\perp}(Cos(\phi)Cos(t\omega) - Sin(\phi)Sin(t\omega))dt, \tag{2.10}$$

$$\int \frac{dy}{dt} dt = \int V_{o\perp}(Cos(t\omega)Sin(\phi) + Cos(\phi)Sin(t\omega))dt. \tag{2.11}$$

When we apply the appropriate initial conditions $z|_{t=0} = 0$ and $y|_{t=0} = 0$, we get

$$z = \frac{V_{o\perp}}{\omega}(Cos(\phi)Sin(t\omega) + Sin(\phi)Cos(t\omega) - Sin(\phi)), \tag{2.12}$$

$$y = -\frac{V_{o\perp}}{\omega}(Cos(t\omega)Cos(\phi) + Sin(\phi)Sin(t\omega) - Cos(\phi)). \tag{2.13}$$

Now we have two equations and two unknowns $V_{o\perp}$ and ϕ. Solving the system of equations yields the following results in

$$V_{o\perp} = \frac{\omega (y^2 + z^2)}{2\sqrt{(y^2 + z^2) Sin\left(\frac{\omega t}{2}\right)^2}}, \tag{2.14}$$

$$\phi = Cos^{-1}(\frac{y - y\,Cos(\omega t) + z\,Sin(\omega t)}{2\sqrt{(y^2 + z^2) Sin\left(\frac{\omega t}{2}\right)^2}}). \tag{2.15}$$

Solving for P_z and P_y and reducing this equation produces

$$P_z = m\frac{\omega}{2}\left(z\,Cot\left(\frac{\omega t}{2}\right) + y\right), \text{ and } P_y = m\frac{\omega}{2}\left(y\,Cot\left(\frac{\omega t}{2}\right) - z\right), \tag{2.16}$$

31

which are the equations used to determine the initial momentum for each fragment.

The trajectory of the ions are also twisted but this turns out to be a much smaller and even ignorable effect, because the ions are considerable more massive (at least 1836 times more massive) and thus their initial velocities are lower. The end result of Eq. 2.2 is that electron and ionic fragments, often called recoils, are accelerated to their respective particle detectors.

2.5 Detectors

Once the ions and electrons have been pushed to the end of the spectrometer by the magnetic and electric fields, they must then be measured. The position sensitive detectors are sensitive enough to measure an individual electron or ion. Each detector consist of two main elements: micro-channel plates, and the delay line anode. Two MCPs are mounted on top of the delay line anode and separated by roughly half a centimeter[39].

A cutaway of a MCP is shown in Fig. 2.9. A MCP works on the same principles as a continuous-dynode electron multiplier[40,41]. The plate is made out of a highly resistive material, usually some type of lead glass, with an array of through holes. These holes or channels are "treated in such a way as to optimize the secondary emission characteristics of each channel and to render the channel walls semiconducting"[40]. The channels are biased at a shallow angle (usually 8° from the normal vector). The front and rear surfaces are usually plated with Nichrome or Inconel. This metal plating allows electrical contact to the top and bottom of each channel. The exact specification of the MCP are considered trade secrets and therefore not known to the author.

When an incident particle strikes a channel, it produces secondary electrons that are then accelerated toward the opposite side of the MCP by the electric field in the MCP. These secondary electrons then collide with the walls of the channels and produce tertiary electrons. This cycle is
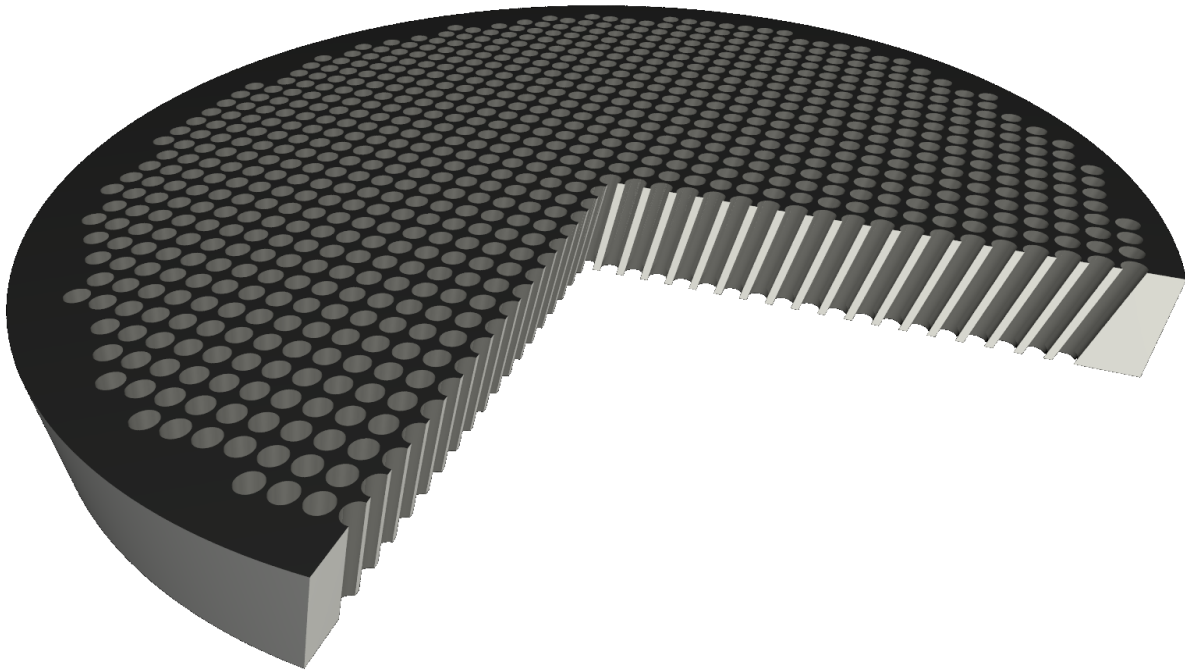
Figure 2.9: Cutaway view of a MCP.

repeated many times over before the electrons exit the opposite side of the plate as shown in Fig. 2.10. Each cascade of electrons leaves the MCP stack with a deficit of electrons, which is then replenished by the power supply. This is measurable via the small dip in the voltage on the MCP. This fluctuation in the voltage is picked off via a RC high pass filter, and is used to determine when a particle has hit the detector.

For optimal response characteristics, one needs to operate the MCP with a ≈ 1000 volt difference between the front and back of the plate[40]. The incident charged particle needs to have at least a certain kinetic energy in order to reliably trigger a cascade in the MCP. For ions a couple of kilovolts is optimal and for electrons half a kilovolt is sufficient. The potential difference between the spectrometer grid and MCP front is adjusted so that the kinetic energy of the incident
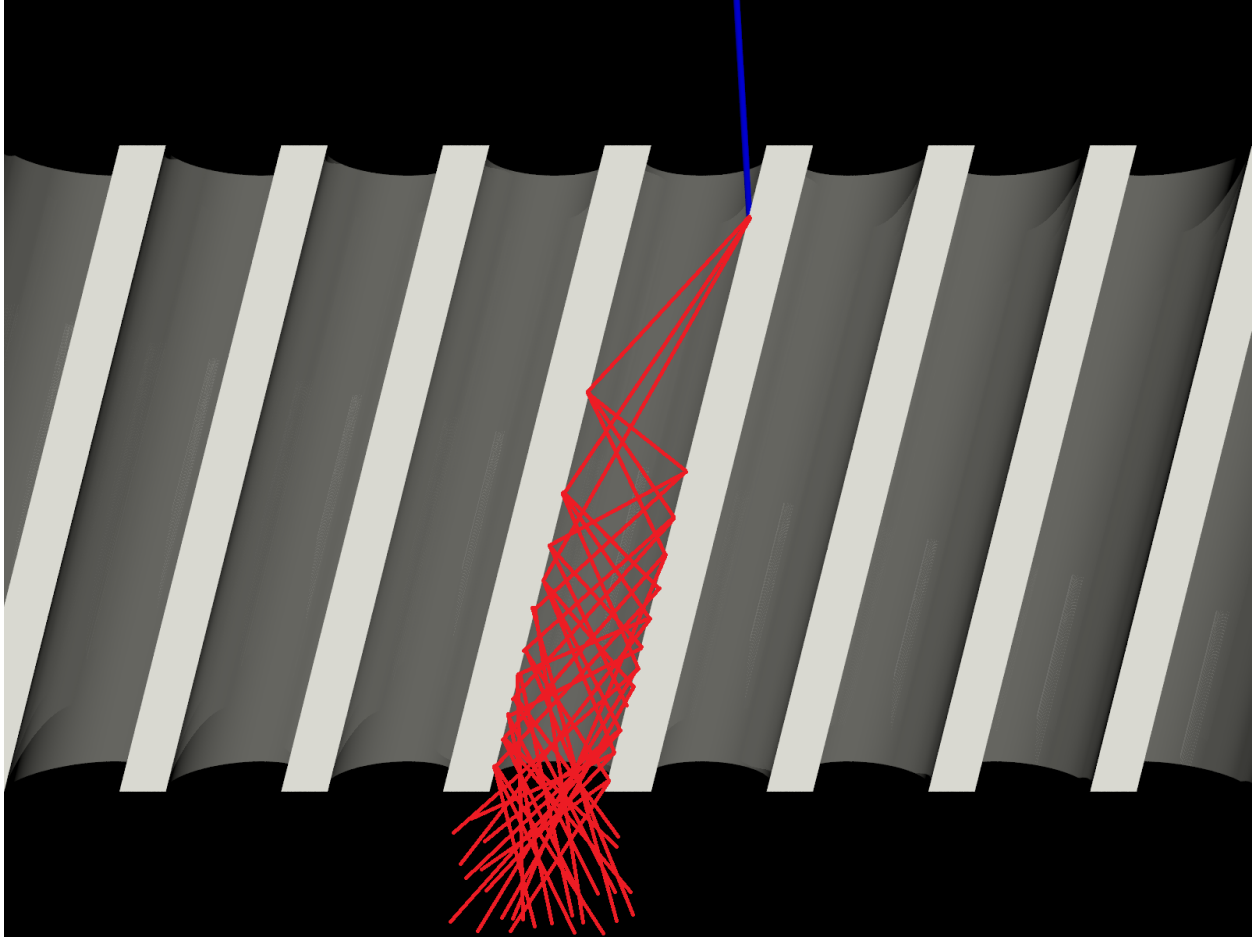
Figure 2.10: Diagram of the electron avalanche in a micro channel plate. The incident charged particle is shown in blue and the subsequent electrons are in red.

particles is high enough to ensure a cascade is likely. To increase the gain, two plates are used together in a chevron configuration. This results in a gain of 10^7 to 10^8.

The next stage of the detector is the delay line anode shown in Fig. 2.11. The delay line anode is held at a higher electrical potential than the back of the MCP stack. This potential difference causes the electrons produced in the MCP stack to be accelerated towards the delay line anode. This cloud of electrons produce a signal pulse on the wires of each layer.

There are several types of delay line anodes, but in this experiment we used a two layer anode, called a square anode, and a three layer anode, called a hex anode. Each layer consists of two parallel wires wound around the detector frame. These two wires are labeled as "signal" and
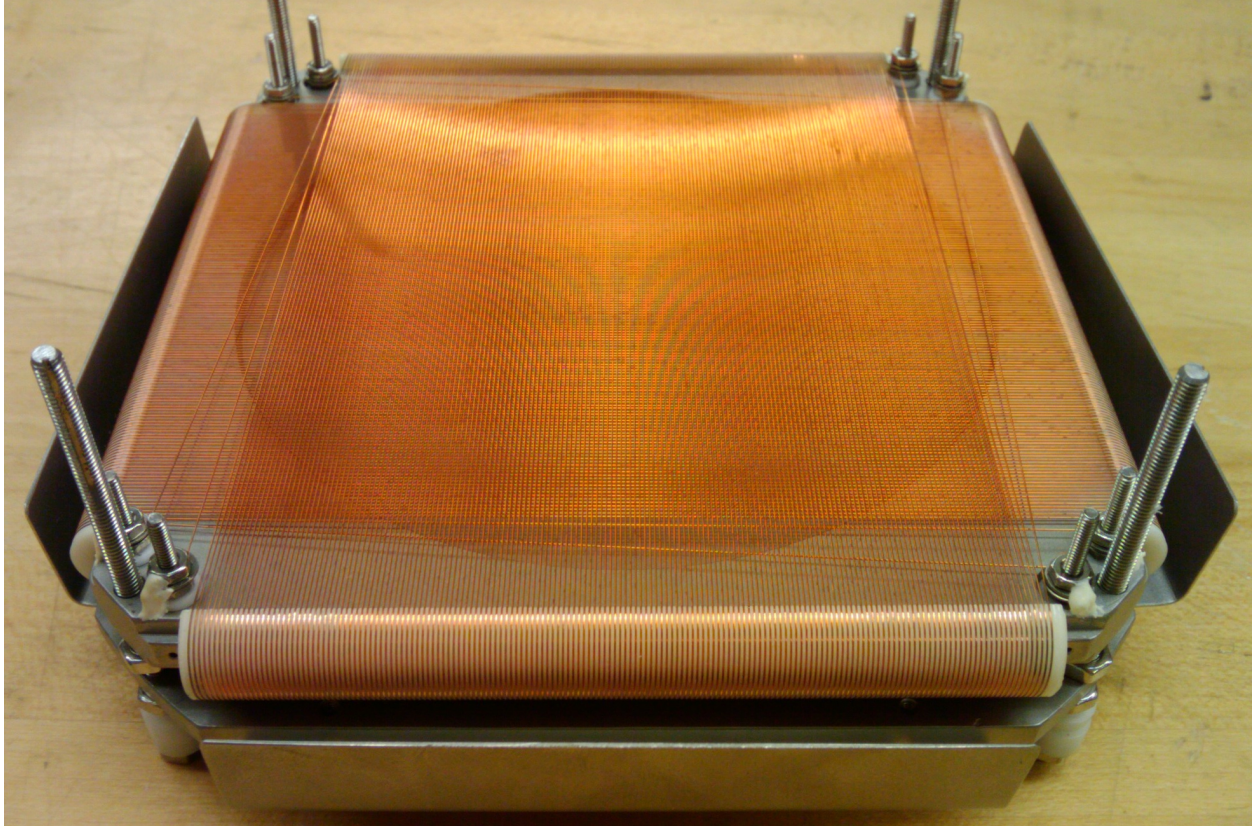
Figure 2.11: Picture of a square delay line detector. This is the back of a square delay line anode.

"reference", but there is no physical difference between the wires. The "signal" and "reference" wires are normally set to have about a 50 volt relative difference and roughly 300 volts between the wires and the back of the MCP. These two wires act as a waveguide and the potential difference helps electrical signal propagate down the wires.

In the case of the square anode, which has two layers, the layers are wrapped in orthogonal directions. The hex anode's, which has three layers, layers are wrapped at 60° intervals. The hex anode is a more complicated detector and the software to analyze the results is also more complicated, but they have better multi-hit capabilities. The ion detector was a square anode 120 mm detector, and the electron detector was a hex anode 80 mm detector.

The AC signals off of the "signal" and "reference" wires are combined through a transformer to filter out noise. This combination is done on each end of the layer. The result for the first layer

is labeled x$_1$ and x$_2$. As with any wire, a signal starting on one end of the wire will take some measurable amount of time to reach the opposite end of the wire, which we referred to as the time sum. This speed of signal propagation is the basis of the delay line detector. The electron cloud emitted from the MCP stack causes a signal to be induced on the wires of each layer. This signal then propagates down the wires in both directions and eventually reaches the end the wire. The position of a hit on the detector can be determined by comparing the time it takes for the signal to reach each end of the layer, or

$$x = \frac{L}{t_{sum}} \left(t_{x_1} - t_{x_2} \right),$$ (2.17)

where x is the position, L is the length of the wire in the layer, t_{x_1} is the time that the signal arrives at the x$_1$ side of the layer, t_{x_2} is the time that the signal arrives at the x$_2$ side of the layer, and t_{sum} is the time sum. It should be noted the time sum is a constant for each layer. This is a useful fact that is used to discriminate noise from real hits. This algorithm is used on each layer, which allows us to determine the two dimensional position of each particle.

2.6 Electronics

The electronics setup for an experiment of this nature is daunting. Many of the electrical components in this experiment were custom made. Maximizing the signal to noise ratio can be quite time consuming and difficult since all of the electrical hardware is adjustable. This adjustability leads to a vast parameter space.

The first step in setting up this experiment was to supply power to the spectrometer and detectors. The spectrometer was powered by a pair of Standford Research Systems PS300 series power supplies[42]. These supplies are stable to within 0.01%/hour and have a display accurate to ± 1 V. The recoil grid was set at -78 V and the middle grid and the electron grid was set at ground.
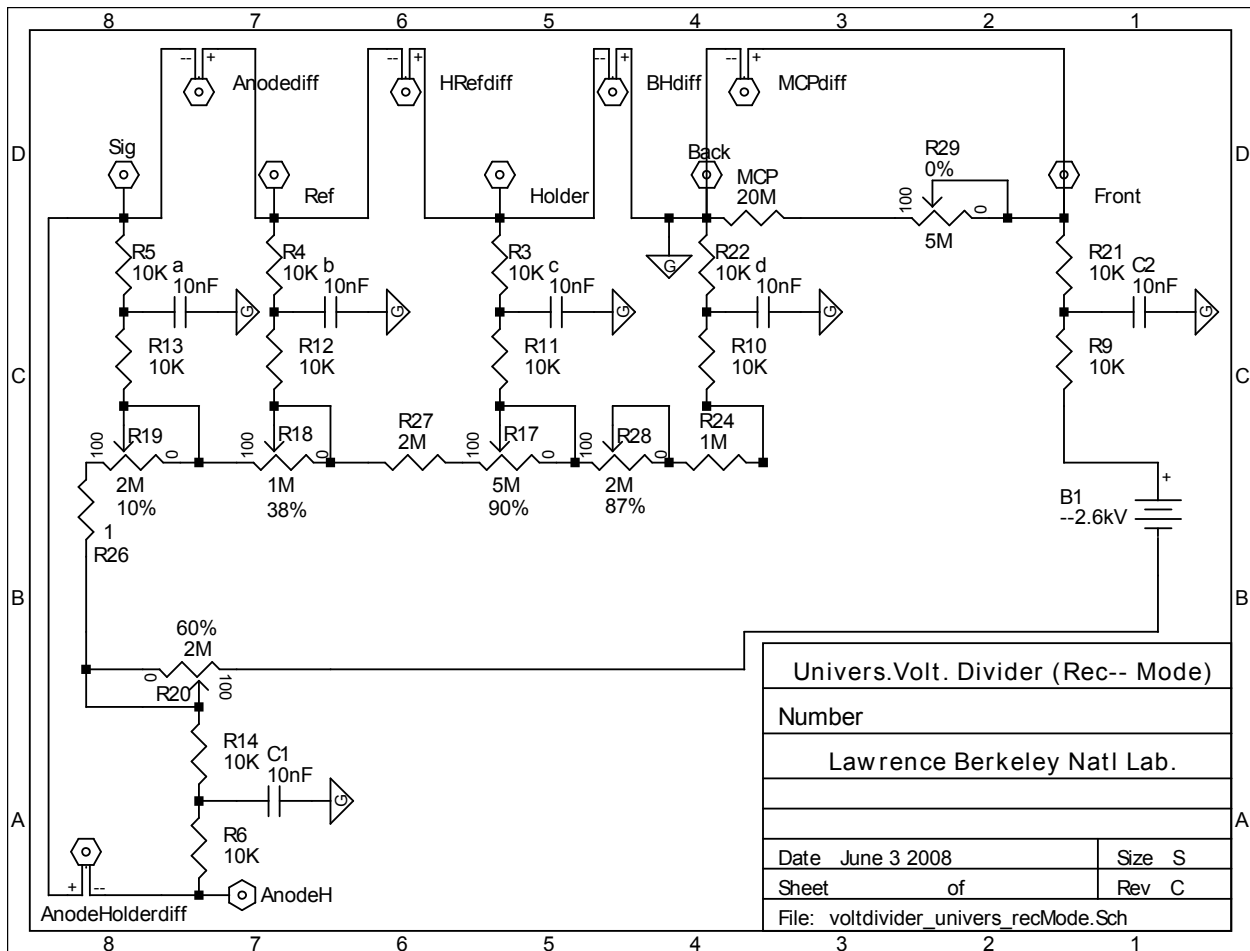
Figure 2.12: Schematic of the voltage divider circuit.

Powering the detectors was accomplished through the use of a voltage divider, which is shown in Fig. 2.12. This voltage divider is powered by a RoentDek HV2/4. The voltage on the front of the MCP and the anode holder is set by the power supplies directly. The remainder of the detector components are set through the resistor chain in the voltage divider. This is designed to supply approximately the correct voltage to each component, but the potentiometers usually have to be tuned for ideal operating conditions. The recoil MCP front was at -2199 V and the anode holder was at +200 V. The electron MCP front was at +249 V and the anode holder was at +2901 V.

The next major piece of the electronics system was the signal processing subsystem. Fig. 2.13 shows the signal flow from the MCP and anode wires to the Time to Digital Converter
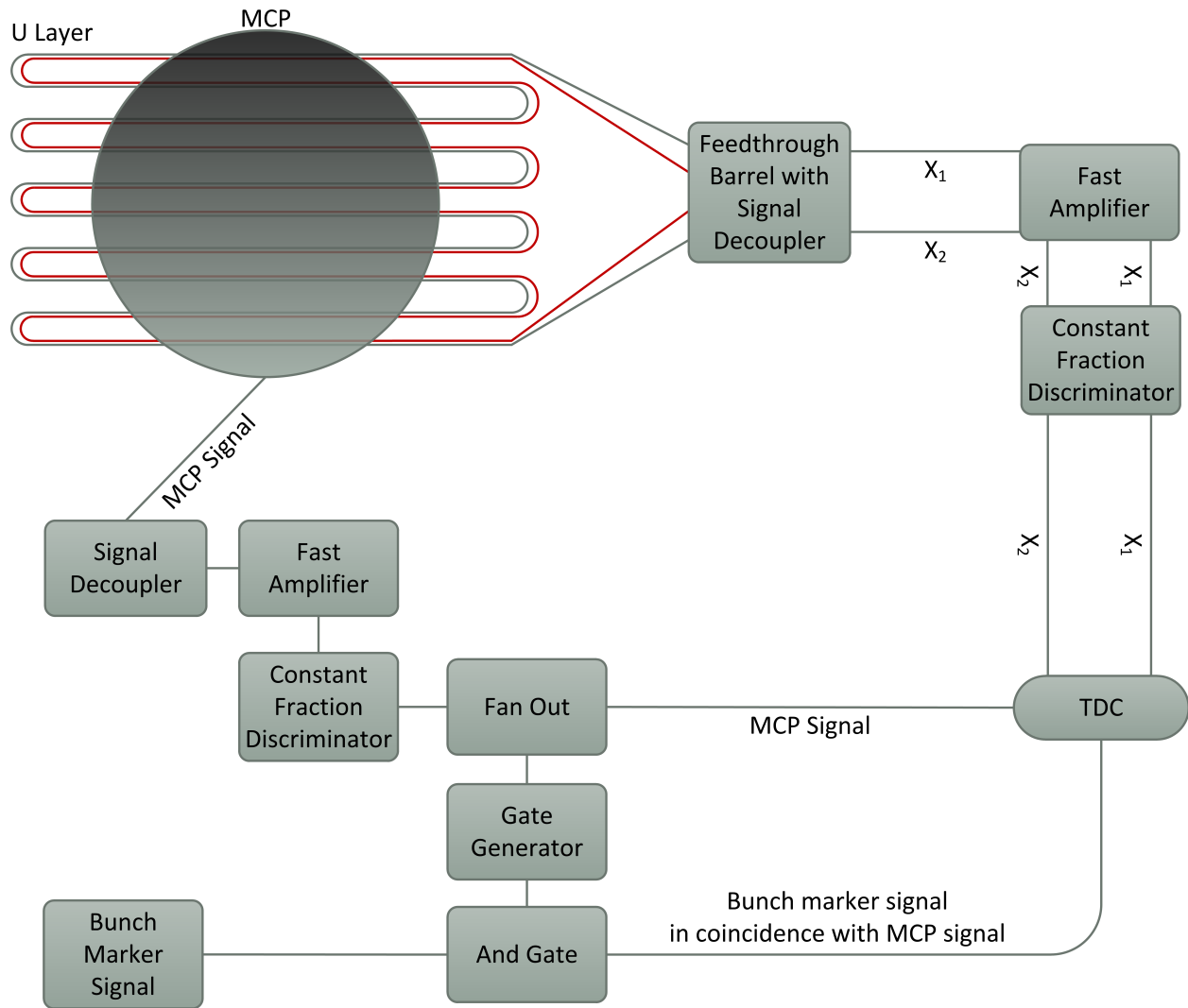
Figure 2.13: Flow chart of the signal electronics. This is repeated for each detector. The part that handles the position signals is repeated for each layer on the detector.

(TDC). The high voltage DC for the "signal" and "reference" wires passes through the vacuum feedthrough barrel where the AC signal is picked off via a RC circuit similar to the one shown in Fig. 2.14. These AC signals from "signal" and "reference" are then combined through a pulse transformer. This pulse transformer is configured so that when the voltage on both "signal" and "reference" move up or down together, the signal is attenuated on the output of the transformer. However, if the voltage on the two wires move in opposite directions, the output signal is amplified. This helps increase the signal to noise ratio.

The signal decouplers are the first step in measuring the TOF. Again, the high voltage DC passes through the decoupling circuit and a RC circuit picks off the AC signal. All of the detector
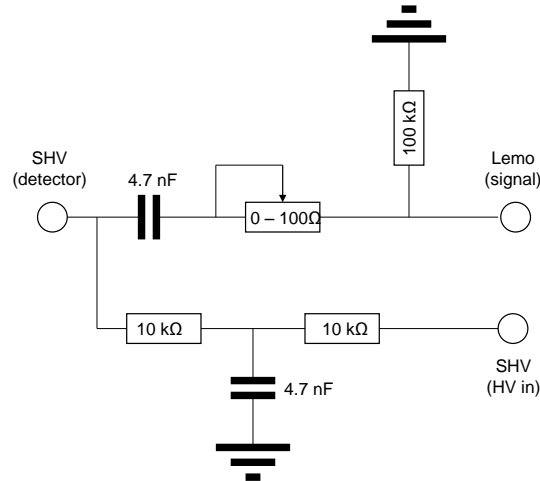
Figure 2.14: Schematic of the signal decoupler circuit used for the MCP signal.

signals are feed into several custom fast amplifiers. Once the signals have been amplified they are then fed into a RoentDek CFD4 constant fraction discriminator (CFD). These CFDs convert an analog pulse into a square pulse. This square pulse is triggered at a constant fraction of the analog pulse rise time. This is a useful technique for determining the time of the analog pulse and it is independent of the analog pulse's pulse height.

The beamline at the ALS provides a signal to notify us when a pulse of x-rays have entered the spectrometer. This is referred to as the bunch marker signal. The photon repetition rate is about 3MHz, and the time between the bunches is very regular (328ns). The most probable result of a photon pulse is that nothing is ionized. As a result of this, and because of limited buffer size in the TDC card, a bunch marker is only recorded if there is also a hit on the detector. Usually the gate width is set to be three or four multiples of the bunch spacing.

From the CFDs the signals are routed into the TDC cards. There are two synchronized Cronologic TDC8HP cards to digitize the input signals. The TDC8HP cards have 8 channels each

and have a 25ps bin size[43]. The TDC was configured to record all signals that happen with $\pm 15\mu$s of the TDC trigger, which was a single recoil.

2.7   Software

The data is taken through CoboldPC 2008, which is a proprietary software package made by Roentdek specifically to record data from delay line anodes. CoboldPC records the data in a list mode file (LMF). The LMF format is useful, because it records each event separately. This allows us to replay the experiment offline. This means that we can select and examine particular fragmentation channel all in software after the experiment is finished.

Most of the analysis was accomplished in the custom written program LMF2root. LMF2root was written primarily by A. Czasch, T. Jahnke, and M. Schoeffler of J. W. Goethe Universität. Since every experiment is different, the analysis code must be individually written. The analysis is really a two step process. The data is processed via LMF2root and then the results are displayed via ROOT[44], which is an open source data analysis application and framework.

The software used in this experiment is one of the most intricate parts of this experiment, but it is also the most opaque. To help alleviate this problem, some of the most intricate pieces of source code will be include in the appendices. The techniques used to obtain our results for each fragmentation channel will be heavily discussed in the subsequent results sections of this dissertation.

Chapter 3

Calibration

"[T]here are known knowns; there are things we know we know. We also know there are known unknowns; that is to say we know there are some things we do not know. But there are also unknown unknowns – there are things we do not know we don't know."

—United States Secretary of Defense Donald Rumsfeld

3.1 Overview

This study could be viewed in three phases: the first phase is planning and preparation, followed by the actual experiment, and then data analysis. This experiment was the result of a fruitful collaboration between LBNL, Goethe University Frankfurt, and Auburn University. The first step was deciding what experiment will be done and how to accomplish it. This means that the spectrometers must be simulated, cross-sections determined, and a suitable beam line must be chosen and an application[a] to use that beam line must be submitted and accepted. Then the apparatus was prepared by the LBNL group and the author. This included assembling the spectrometer and detector and then testing them. In addition the jet nozzle had to be changed, which forced us to realign all of the jet components and differential stage. We tried to test as many components as possible before the experiment to ensure everything was functioning properly. This phase is crucial, because it affects everything that comes after it.

---

[a]In reality this is usually done well in advance of the beam time.

The actual experiment involves an international collaboration that comes together to make the experiment possible. A team from Goethe University Frankfurt along with workers from Auburn University joined the LBNL group to help conduct the experiment. This large team was useful, because the setup and operation was a twenty-four hour affair. Setting up the experiment required us to move a large amount of equipment to the ALS. Because many of the parts are delicate, most of the equipment assembled in the first phase had to be taken apart before it could be moved. It is all reassembled at the beam line in a marathon fashion. Once everything was functioning, which is no small task, we got down to actually taking data. The entire experiment took almost two weeks, though the methane datasets were recorded in about four days.

The last phase was data analysis. There is about five hundred megabytes of data on methane. This dataset must be sorted and calibrated before it can produce useful measurements. Perhaps the most difficult part, and certainly the most time consuming part, of the analysis was the calibration phase. To understand the complexity, one must simply look at the sheer number of parameters that must be determined. Small mysterious discrepancies between predicted values and the data can arise. These discrepancies can lead to vast expenditures of time in an attempt, sometime futilely, to determine their cause. One such case is covered in Section 3.6.4. Another complication is determining the precision needed for each calibration parameter. From a human standpoint, this can be extremely difficult. Being able to make this determination is critical, because nearly an infinite amount of time could be spent calibrating the data otherwise. With these facts in mind, we will embark on a brief explanation of the methods and results that were used to calibrate the experimental data.

3.2   Photon Energy

The ALS is a user facility, and as such, many of its systems are automated for ease of use. While this certainly saves time, it should be treated with the proper skepticism. This brings us to

the first step in the calibration process, which is to determine if the photons are actually of the energy that the beamline reports they are. The photon energy is set by adjusting the gap in the undulator and position of the exit slits in the monochromator. This energy is really the peak in the energy distribution. There are many different ways to calibrate the energy of the photons to accomplish this task, but the one used was to scan the photon energy across the N_2 (N $1s \rightarrow \pi^*$) resonance of molecular nitrogen. This is a sharp line below the N 1s ionization threshold with a well known energy that is easily resolvable. These properties make it useful for calibration. The results of this energy scan are shown in Fig. 3.1.
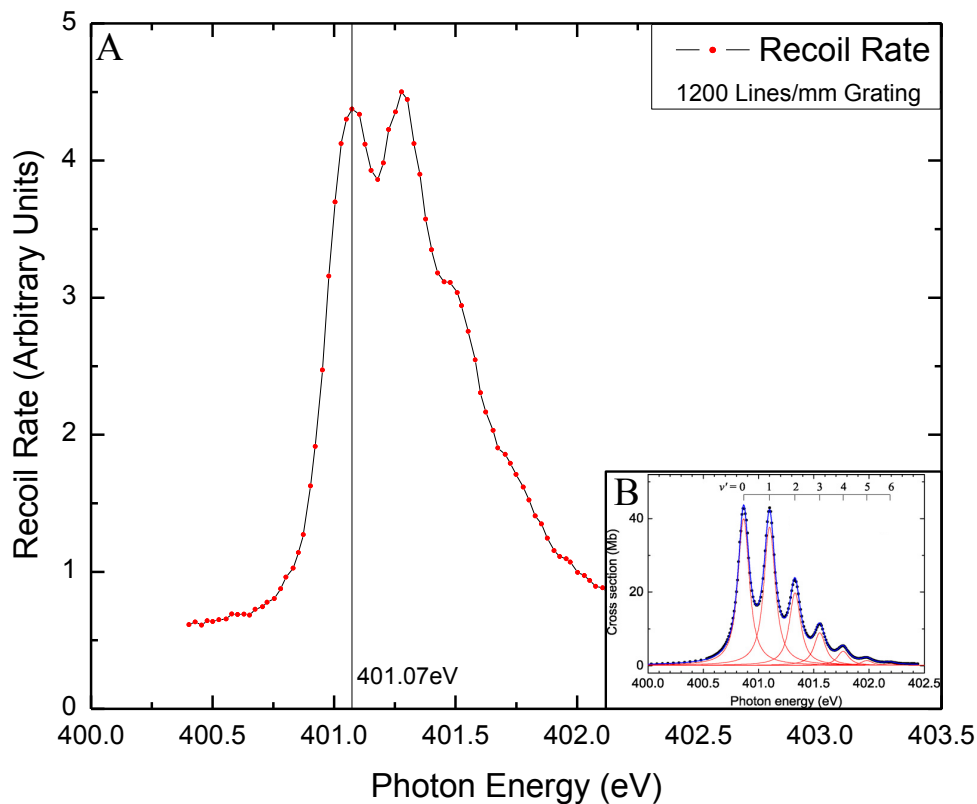
Figure 3.1: Partial ion yield for molecular nitrogen (A). The line marks the peak of the partial ion yield for the N_2 (N $1s \rightarrow \pi^*$) resonance. The inlay graph (B) is taken from N. Saito et al[45]., which is used for calibration.

We determined the value of the first peak to be 401.07eV, but in 1984 Rana N.S. Sodhi and C.E. Brion found it to be at 400.88 ± 0.02eV[46] and in 2007 N. Saito et al. put it at 400.865 ± 0.02eV[45]. This means the peak of the energy distribution reported by the beam line when using the 1200 $^{\text{lines}}/_{\text{mm}}$ grating was off by approximately 0.2eV.

There are two different diffraction gratings available on the beam line, the 1200 $^{\text{lines}}/_{\text{mm}}$ grating and the 150 $^{\text{lines}}/_{\text{mm}}$ grating. The experiment was performed using the 150 $^{\text{lines}}/_{\text{mm}}$, because the flux is much higher on this grating. The flux curves are shown in Fig. 2.5. As a result, it is necessary to calibrate the 150 $^{\text{lines}}/_{\text{mm}}$ grating to the 1200 $^{\text{lines}}/_{\text{mm}}$ grating. To do this we scanned photons from both gratings across the carbon K-edge; the results of which can be seen in Fig. 3.2.
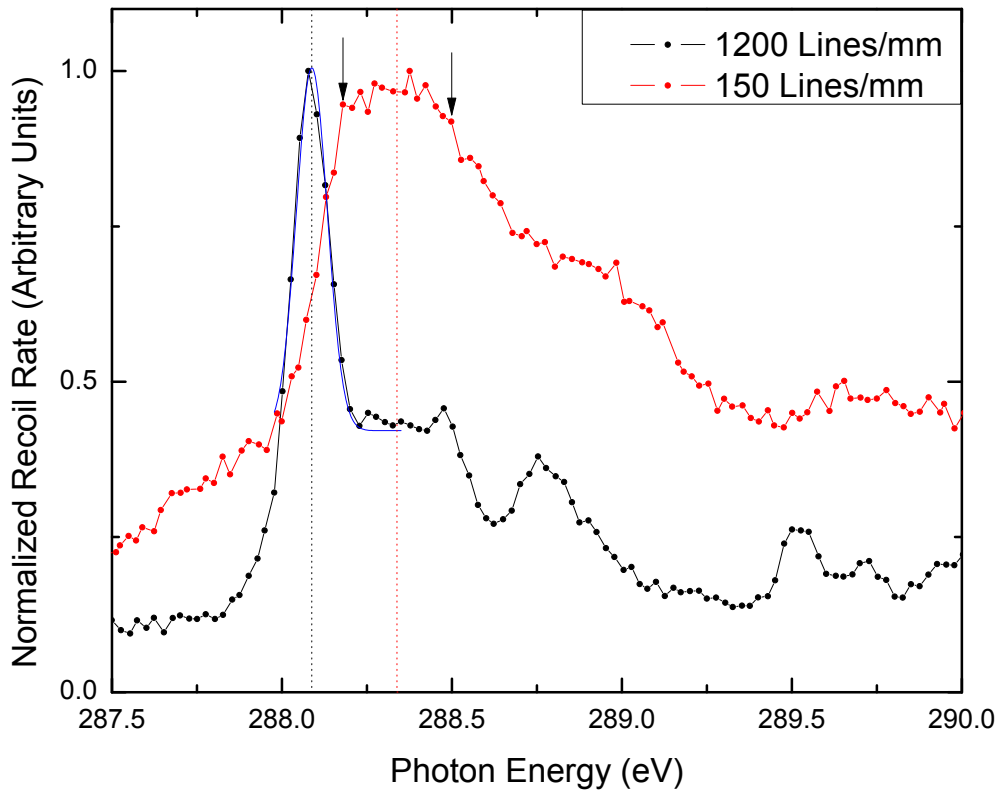
Figure 3.2: Relative Cross-Section of Methane at the Carbon K-edge. This was done using both the 150 $^{\text{lines}}/_{\text{mm}}$ and the 1200 $^{\text{lines}}/_{\text{mm}}$ diffraction gratings. The photon energy is not calibrated. The dotted lines are the estimated peak centroids of 288.088eV (black line) and 288.3388eV (red line).

It is easily visible that the energy resolution of the 1200 $^{\text{lines}}/_{\text{mm}}$ grating is better than the 150 $^{\text{lines}}/_{\text{mm}}$ grating. In Fig. 3.2, the 1200 $^{\text{lines}}/_{\text{mm}}$ data is fit with a Voigt function to determine the centroid, which is 288.088eV. The same peak in the 150 $^{\text{lines}}/_{\text{mm}}$ data is blurred out and thus is not able to be fit reliably. This makes it problematic to determine the center of the peak. The solution we employed is simple and somewhat arbitrary. We picked the two data points on the edge of each side of the peak (denoted by arrows) and averaged their positions. This results in a value of 288.34eV, which certainly should not be trusted to better than a tenth of an electron volt. Using these results, we estimate that the 150 $^{\text{lines}}/_{\text{mm}}$ grating is shifted by approximately 0.25eV from the 1200 $^{\text{lines}}/_{\text{mm}}$ grating.

In the final calibration, we combine the 0.25eV and the previously determined 0.2eV from the 1200 $^{\text{lines}}/_{\text{mm}}$ grating, which yields a total an energy correction of -0.45eV. Using this calibration we determined the photon energy was ~295eV. This is also consistent with the results from Jakubowska et al.[47], where they measured they Rydberg states in methane. While it is important to know the photon energy, it should be noted that the main thrust of this experiment is angular distributions of the photoelectron, which are extremely insensitive to the absolute photon energy calibration.

3.3   Time Zero Calibration

Time of flight for the ions and electrons are determined by measuring the photon pulse in coincidence with the ions and electrons, but our apparatus does not measure the photons pulse directly. We instead utilize the bunch marker signal that is supplied by the ALS. The bunch marker signal simply signals when a electron bunch has passed through the nearest RF acceleration cavity in the storage ring. It is important to note that the bunch marker signal must be generated and travel to our end station, all of which takes time. This leads to a bunch marker signal that does not actually mark the time of the photon pulse, but instead is delayed in time from the true photon

pulse. In this section, we will determine by how much the bunch marker signal is delayed and thus the true time of flight for the ions and electrons.

The method we will demonstrate here is based on the electron's cyclotron frequency. Ejected electrons are subject to parallel electric and magnetic fields. In section 2.4, we examined the equation of motion for a charged particle in an E and B field and noted that the frequency was dependent on only the charge, mass, and magnetic field.

$$f = \frac{qB}{2\pi m} \tag{3.1}$$

One useful technique to facilitate this calibration is to turn up the photon energy, which means that the photoelectrons are more energetic. These energetic electrons have the ability to complete more than one cyclotron rotation before striking the detector depending on the angle
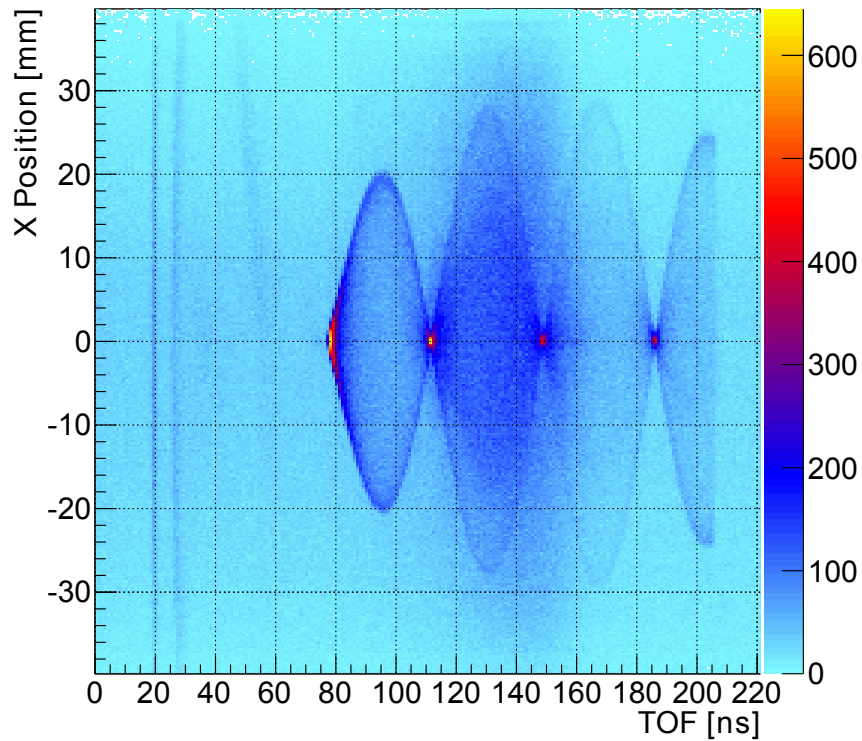
Figure 3.3: Electron X position vs time of flight. The nodes in the electron spectrum are visible as the bright spots. Note that times of flight in this plot have already be corrected.

they are emitted. It is also useful to increase the magnetic field so more nodes are visible. If the emitted electron has a time of flight roughly equal to an integer multiple of the cyclotron frequency, then it will land in the center of the detector regardless of the direction in which it was emitted. These nodes are visible in Fig 3.3 and the time of each node can now be determined from this figure.

Table 3.1: Measured node times for time zero calibration

Node	Time
2	∼9∅ ns
3	123.56 ns
4	16∅.6∅ ns
5	198.∅5 ns
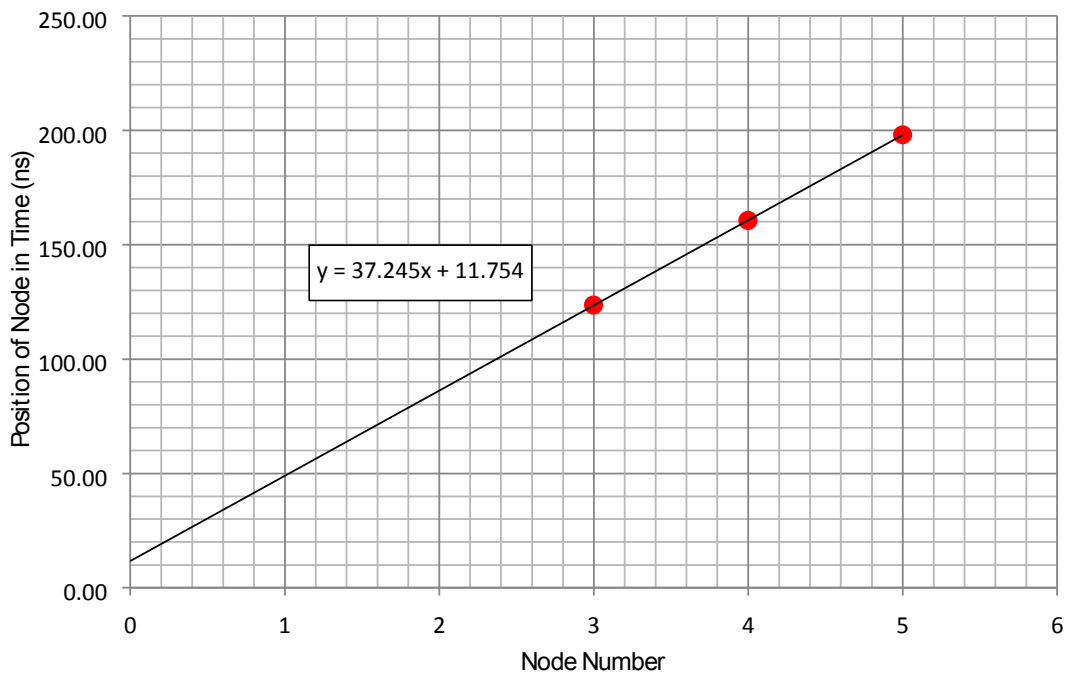
Figure 3.4: Linear regression of nodes in electron position vs. TOF spectrum.

In Fig. 3.3, the first node is not visible and the second is not fully illuminated. For this reason, we used the third, fourth, and fifth nodes. The average period for this magnetic field is 37.24 ns. The first node would appear near 37.24 ns and the second node should be at 2×37.24 ns =74.44 ns. This can easily be demonstrated by linear regression on the data in Table 3.1 as shown

in Fig. 3.4. From this linear fit it can be seen that the electron TOFs are offset by 11.75 ns. All subsequent particle TOFs are subtracted by 11.75 ns to produce the actual flight time.

3.4 Supersonic Gas Jet Velocity

One of the ultimate goals of the calibration is to be able to accurately produce the momentum of each particle. Ideally, we would like to be in the center of momentum frame. The supersonic gas jet is traveling upwards through the chamber at a measurable velocity. The purpose of this section is to determine that velocity, so it can be subtracted from the particle momentum calculation. If done accurately, this should allow us to calculate the momentum relative to the molecule.
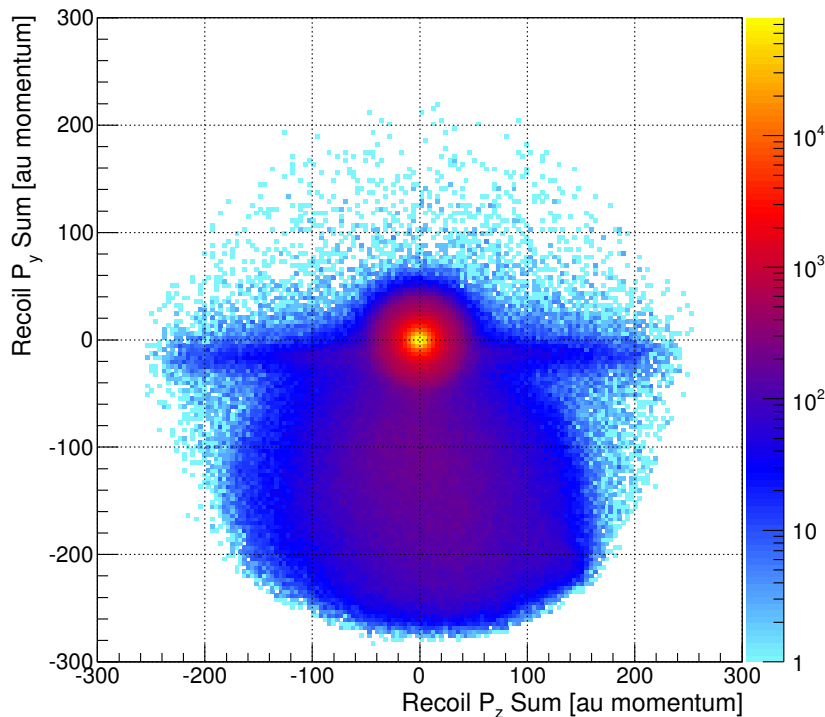
Figure 3.5: Density plot of the momentum sum of CH_3^+ and H^+ ions.

The first step was to calculate the momentum of the ions. We chose the $CH_3^+ + H^+$ breakup channel and summed the momenta of both ionic fragments, which results in Fig. 3.5. The dot in

the center of the density plot is called the jet dot. The jet dot is produced by methane molecules ionized in the supersonic jet. The horizontal line is called the hot gas line and it is from stray room temperature methane in the chamber.

The hot gas line is a projection of the photon beam onto the detector and represents the height of the path that the photons take through the chamber. Molecules in the hot gas line have a velocity in a random direction, and thus the momentum sum spreads out equally in all directions. The methane molecules in the gas jet all have, basically, the same speed and direction. They are all traveling upwards through the chamber.
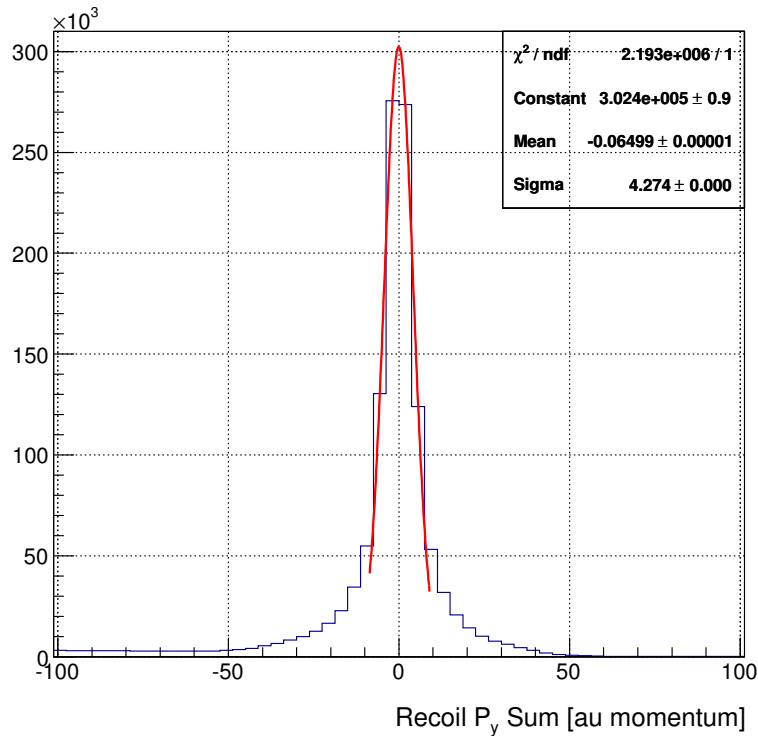
Figure 3.6: Projection of the jet dot from Fig. 3.5 limited to -30 au $\leq x \leq 33.75$ au.

This means the speed of the jet can determine by taking the difference of the jet dot and the hot gas line. This is done by projecting the Fig. 3.5 to the Y axis. The first projection is shown in Fig. 3.6, which is limited to -30 au $\leq x \leq 33.75$ au. From this projection, the vertical position of the jet dot in momentum space can determine by fitting a Gaussian function to it, which is $\sim$-0.064 au. Fig. 3.7 shows the second projection, which is of the hot gas line and is limited to
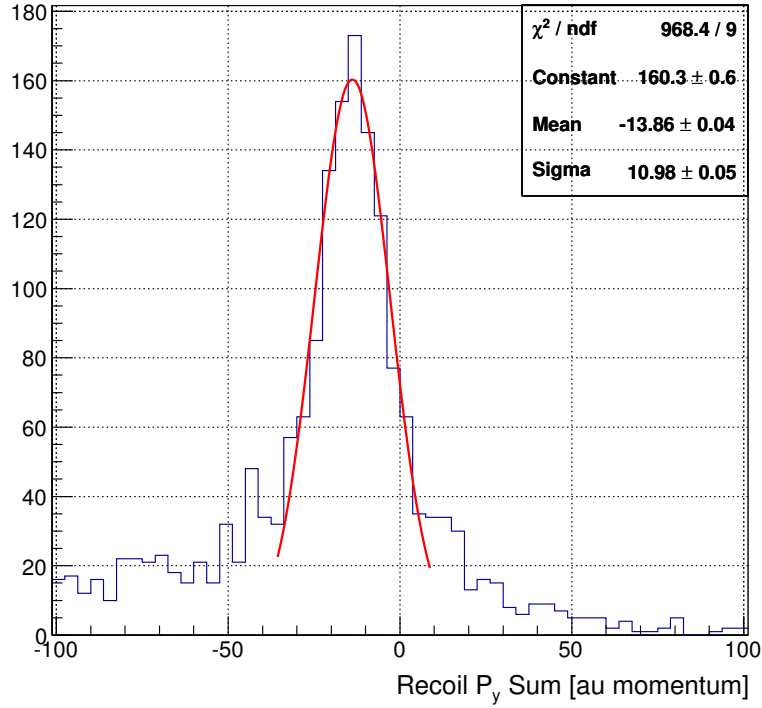
Figure 3.7: Projection of the hot gas line from Fig. 3.5 limited to 168.75 au $\leq x \leq 251.25$ au.

168.75 au $\leq x \leq 251.25$ au. The hot gas line is found in the same fashion and is located at $\sim$ 13.86 au.

The jet velocity was calculated to be $1035 \, ^m/_s$. The value used in the analysis is $1219 \, ^m/_s$, but the version presented here is a more accurate measurement. This error is small compared to the momentum values for the ionic fragments. It is visible from Fig. 3.5 and 3.6 that the momentum is nicely centered on zero; even though there is an error in the jet velocity. In Section 3.6.4 we will see that this error in the jet velocity is almost certainly corrected for by momentum offsets used to correct a lensing issue.

3.5 Detector Orientation

Detector orientation, at first glance, might seem to be a trivial problem, but it can be very difficult. The challenge is to ensure both detectors share a common coordinate system. The

problem is made more difficult in a short molecular spectrometer, because the resolution on the ionic fragments is not sufficient to observe the momentum kick from the electrons (auger or not).
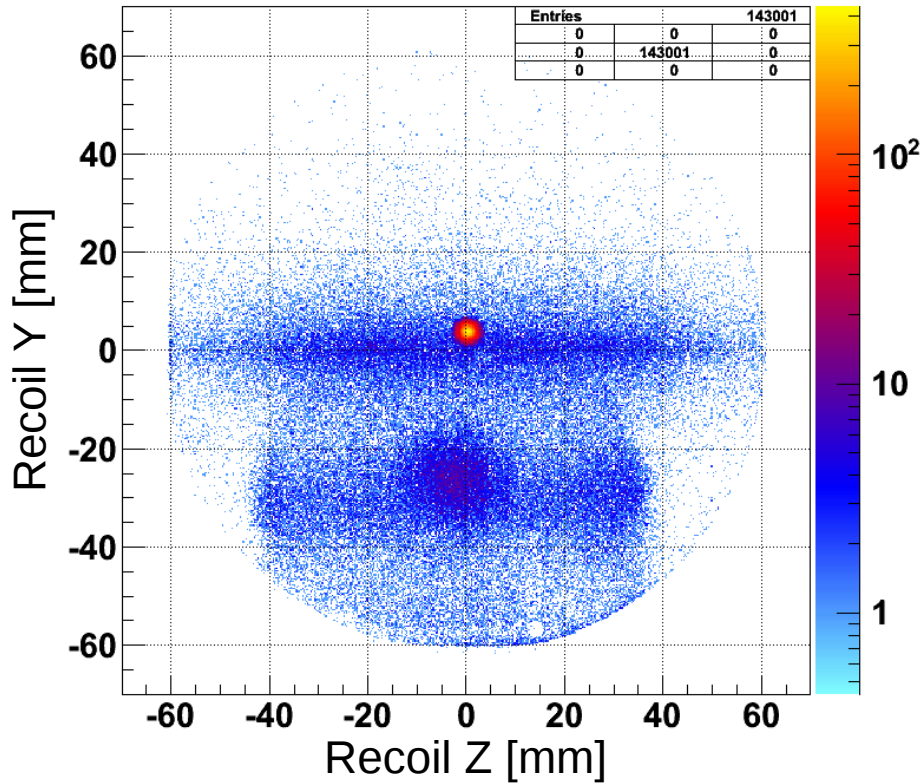
Figure 3.8: Raw recoil position spectrum. The coordinate system is as follows: $\hat{x}$ is in the time of flight direction, $\hat{y}$ is in the gas jet direction, and $\hat{z}$ is in the photon beam direction. This is shown in Fig. 2.2.

The first step is to orientate the recoil detector. This is trivial, because of the hot gas line and the jet dot. The hot gas line is horizontal in the lab. The jet dot should be above the hot gas line, which establishes the up direction in the lab. The lab frame orientation is of no real importance, but it is a convenient coordinate system and thus the one chosen. The recoil detector had to be rotated by 180°, which is shown in Fig. 3.8.

In the bottom half of Fig. 3.8 the reflection of the electron detector is visible. This comes from electrons striking the electron detector's MCP. Most of the time this only produces secondary electrons, but sometimes it produces an ions. This ion is then accelerated by the electric field ($\sim$500 V/cm) in that region toward the recoil detector. It is only visible in the bottom half of

(a) Electron Detector

(b) Unrotated

(c) Electron Detector Flipped and Rotated

(d) Electron Detector Flipped and Rotated (Ungated)
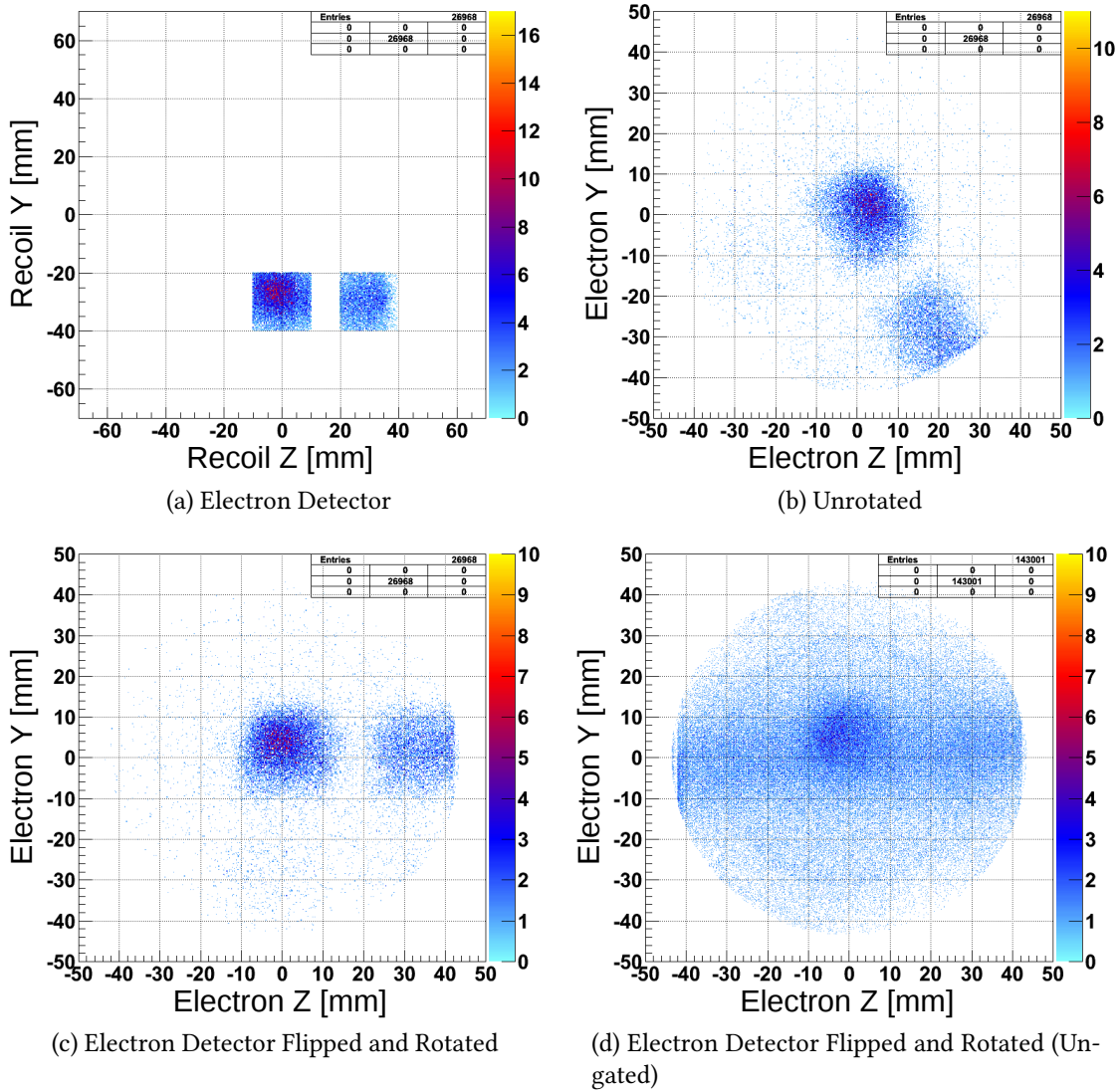
Figure 3.9: Recoil gated electron position spectrum.

the spectrometer, because the channels in the MCP are biased at $\sim 8°$. It is also interesting to note that the electron detector has a diameter of about 80 mm, which is measurable from the reflection in the recoil detector.

The trick to determining the orientation of the electron detector is to gate on the reflection of the electron detector in the recoil. The gates we used are shown in Fig. 3.9a. With these gates in place we examine the electron detector. The gated electron detector is shown in Fig. 3.9a. From this we are able to determine the electron detector's orientation. The electron detector is

first flipped about the z axis and then rotated by -60°; the result of which are visible in Fig. 3.9b and 3.9d.

3.6   Electric and Magnetic Fields

3.6.1   Magnetic Field

In COLTRIMS style experiments, a uniform magnetic field is used to contain the more energetic electrons. The magnetic field strength is set before the experiment begins by adjusting the current flow through the Helmholtz coils. While this allows the magnetic field strength to be set, but it does not allow it set precisely. The actual value of the magnetic field is needed for the electron momentum calculation. To determine the precise magnetic field strength a special data set is taken, where the photon energy is increased and the electric field is decreased. In this case, the photon energy was 306eV and electric field was approximately $5.3^V/cm$. This allows some of the photoelectrons to make a complete cyclotron revolution, which is visible in Fig. 3.10.

$$f = \frac{qB}{2\pi m} \longrightarrow B = \frac{2\pi m f}{q} \tag{3.2}$$

The time it takes to complete one cyclotron revolution is the cyclotron period. The cyclotron period was determined to be 94.75 ns from Fig. 3.10, which is referred to as a "fish" spectrum. Equation 3.1, shown above, can easily be rearranged to yield the magnetic field strength. In this data set the magnetic field strength was found to be 3.77 gauss.

3.6.2   Electric Fields

The spectrometer is a series of plates connected to each other by resistors. Assuming all spectrometer plates are equal distance and the resistors all have the same resistance, or in other
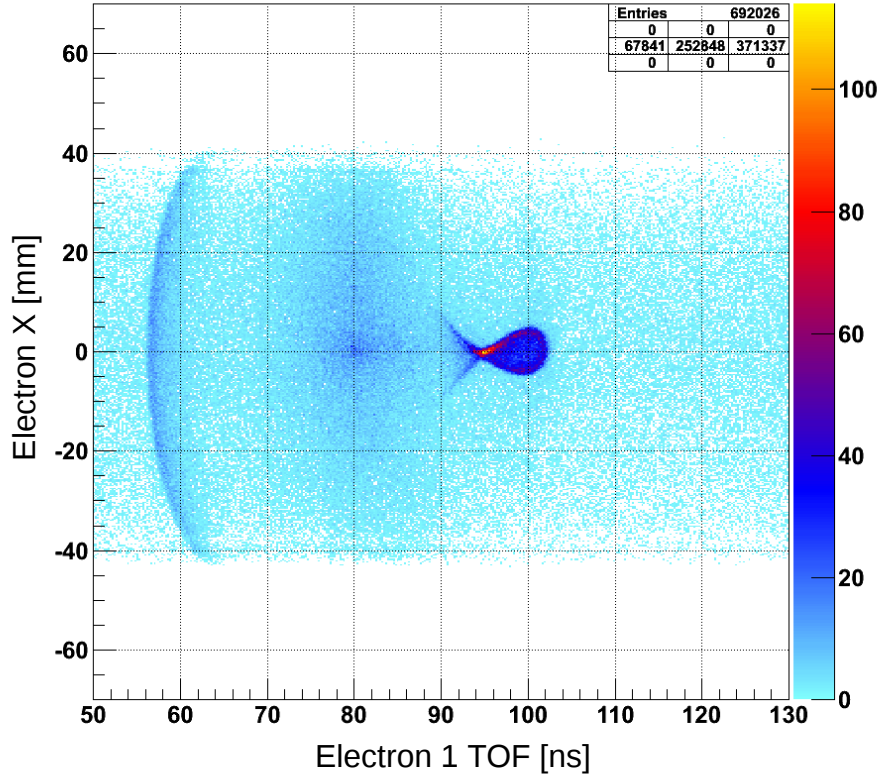
Figure 3.10: Electron X fish plot for the 3.77 gauss data set.

words a constant resistance per unit length, then a uniform electric field can be created by applying a different voltage to each side of the spectrometer. The spectrometer length is known, thus it is easy to set a fairly precise electric field. The acceleration region of the spectrometer is 10.42 cm. On the recoil side of the spectrometer we applied -78 V and grounded the middle and electron side of the spectrometer. This achieved an electric field of $\sim 7.48 ^V/_{cm}$.

The high voltage power supplies used for the spectrometer are Stanford Research Systems PS300 Series. These power supplies are stable and accurate. They typically have a ± 1 volt set accuracy[42]. This ± 1 volt in spectrometer voltage would translate into a $\pm 0.1 ^V/_{cm}$ swing in the electric field. In an attempt to pin down the exact value a ROOT macro was written to predict the photo-ion photo-ion coincidences (PIPICO) for given mass pairs in TOF.

This PIPICO macro begins with the time to momentum algorithm given in Appendix D. The macro is given the mass and charge of both fragments and the electric fields and lengths in each
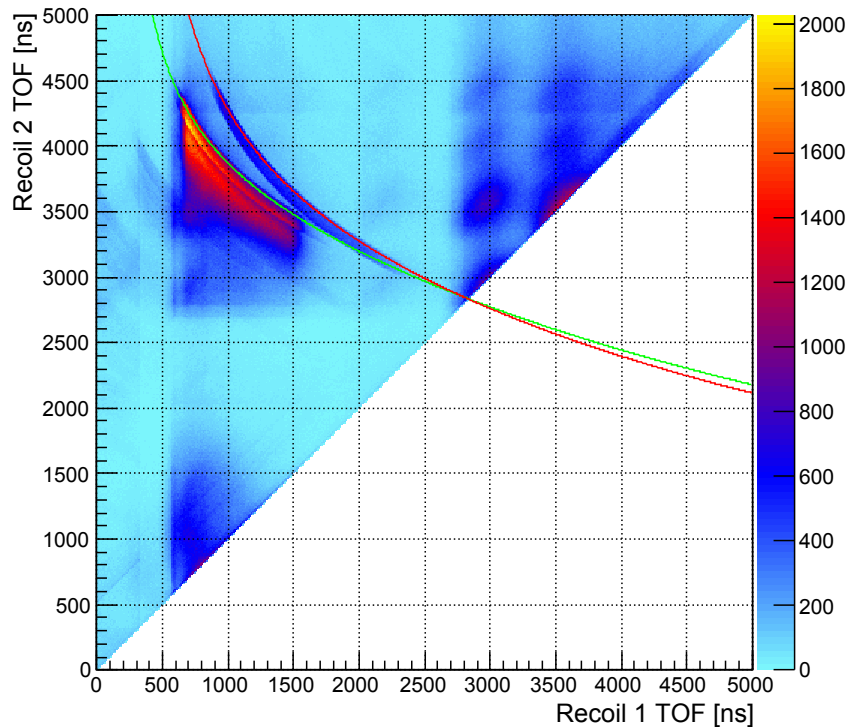
Figure 3.11: Photo-ion photo-ion coincidence (PIPICO) plot. Simulated PIPICO lines are shown on top of the experimental data. The green curve represents the simulated CH_3^+ and H^+ channel and the red curve represents the simulated CH_2^+ and H_2^+ channel.

region. The macro was executed when a PIPICO plot was displayed. The macro takes the x axis range from the PIPICO plot and then cuts that range up into 1000 points. At each of these points the macro starts by calculating what the momentum (in the TOF direction) of the first fragment would be if it had that particular value for the TOF. This macro assumes a two body breakup, which means the second fragment's momentum should be equal and opposite. From this, it then calculates what the TOF would be for the second fragment.

The results of the simulated PIPICO lines can be seen in Fig. 3.11. For this simulation, we used $\sim 7.48^V/cm$. It is clear from Fig. 3.11 that the simulated lines are slightly higher than the experimental data. Much time and effort was put into trying to understand why the two didn't match. This discrepancy is explained in Section 3.6.4.

3.6.3 $\vec{E} \times \vec{B}$ Drift

We have now determined the strength of the electric and magnetic fields. In the previous chapter we stated that the electric and magnetic fields were parallel, but life is rarely that simple. The apparatus is fitted with vertical and horizontal trim coils in addition to the main Helmholtz coils. These trim coils are used in an attempt to align the two field vectors, but it is not perfect.
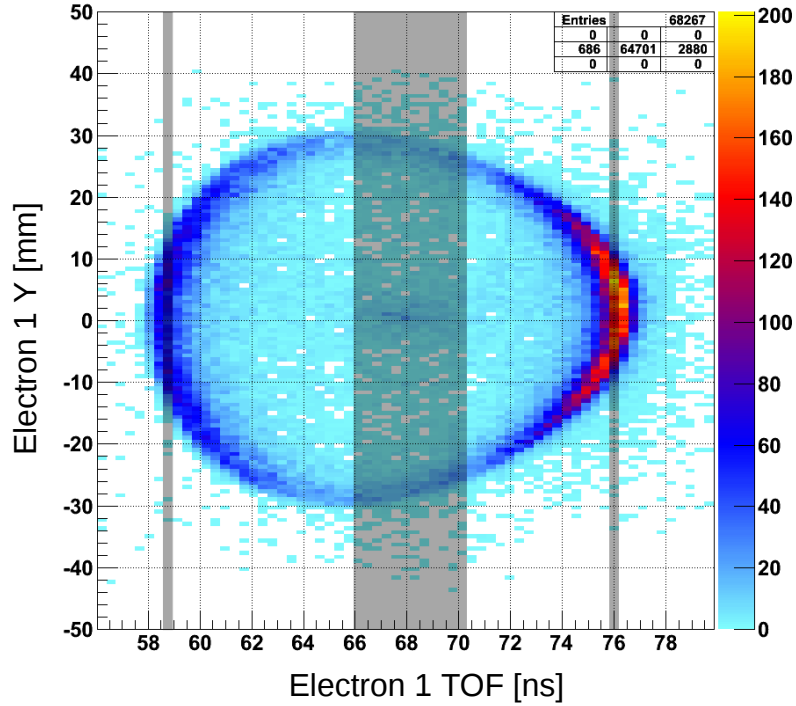
Figure 3.12: Electron first hit Y fish plot, which is limited in the Z position to ± 1 mm. The gray areas were projected to determine the centroid of the distribution at those points in time.

This $\vec{E} \times \vec{B}$ drift results in a constant drift velocity given by Equation 3.3[48]. This constant velocity can be measured and corrected for, which is the purpose of this section. This correction is small and could probably be ignored, but we did carry out this correction, so it is presented here for completeness.

$$v_D = \frac{\vec{E_{\perp}} \times \vec{B}}{B^2} \tag{3.3}$$
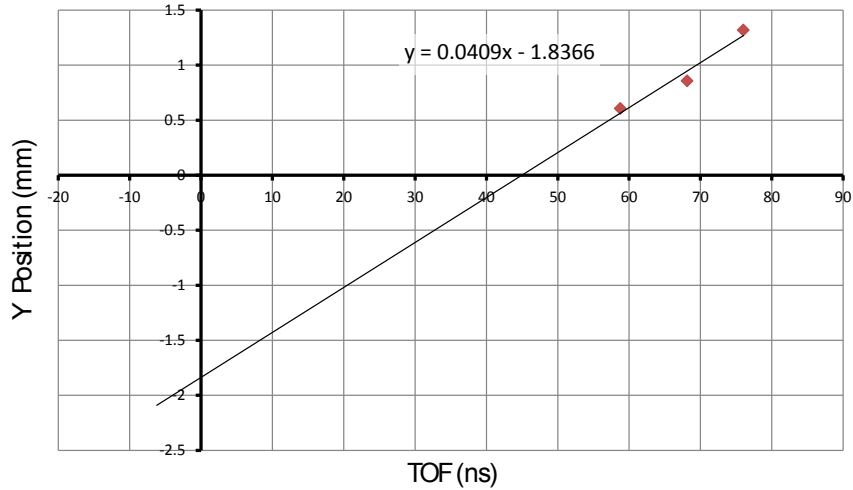
Figure 3.13: Electron Y fish linear regression.
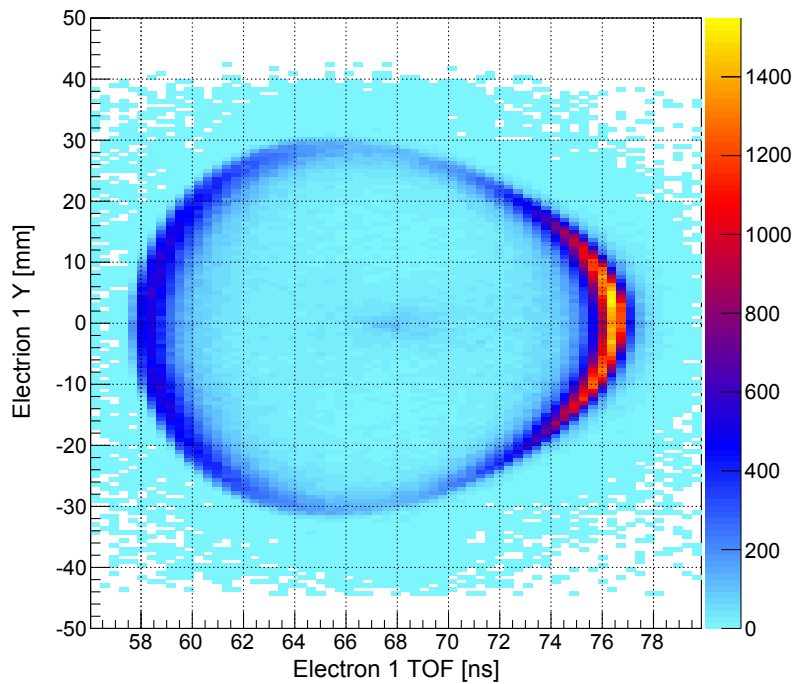
Figure 3.14: Electron first hit Y fish plot, which is limited in the Z position to ± 1 mm.

The $\vec{E} \times \vec{B}$ drift[b] can be seen in Fig. 3.12. It manifests itself as a twist distribution in the electron fish spectrum. The gray areas in the figure were projected and fitted to determine the centroid of the distribution at the point in time. The center projection was fit with a Gaussian

---

[b]One might consider using Fig. 3.3, but that data was taken with a $\sim 1.3^V/_{cm}$ electric field and a ~ 10 gauss magnetic field. As Equation 3.3 reveals, that this would produce a different drift velocity.

function and the two end projections were fit with a linear combination of two independent analytic approximations of the Heaviside step function, which is given in 3.4. The values from the projections are plotted and fitted with a line in Fig. 3.13. From the linear regression we determined the drift velocity in the Y direction is $v_{Dy} = 0.04\,{}^{mm}/_{ns}$ with a position offset of -1.83 mm. In the Z direction, we determined the drift velocity to be $v_{Dz} = -0.06\,{}^{mm}/_{ns}$ with a position offset of 4.49 mm. These values are used to center the electron distribution about the center of the electron detector, which is shown in Fig. 3.14. This is a small correction, but it leads to a more accurate momentum space distribution.

3.6.4 Lensing Correction

The reason for the mismatch that was seen in Section 3.6.2 was found by chance when the spectrometer was being disassembled in preparation for the next experiment. There was an extra 400 kΩ resistor between the recoil grid and the first spectrometer plate. This caused the electric field to be nonuniform, which created an electrostatic lens for the electrons and ions. Fig. 3.15 shows the Simion simulation of the electric field lensing.

The electro static lensing changes where and when the ionic fragments landed on the detector. To properly convert the position and TOF information into an initial momentum vector the lensing must be understood. This led to the creation of a series of simulations and tools to analyze the effects of this distortion. The main tool used was the software package Simion 8[49], which was used to simulate the electric field in a realistic fashion and determine the ion trajectories. The second piece used was a custom written Lua script that exported the data from Simion into Excel. The other main function of the Lua script was to call a custom written DLL file that calculated the momentum of the fragments from the final position and TOF as determined by Simion. The DLL used exactly the same routines to calculate momentum as those used in the analysis of the experimental data.
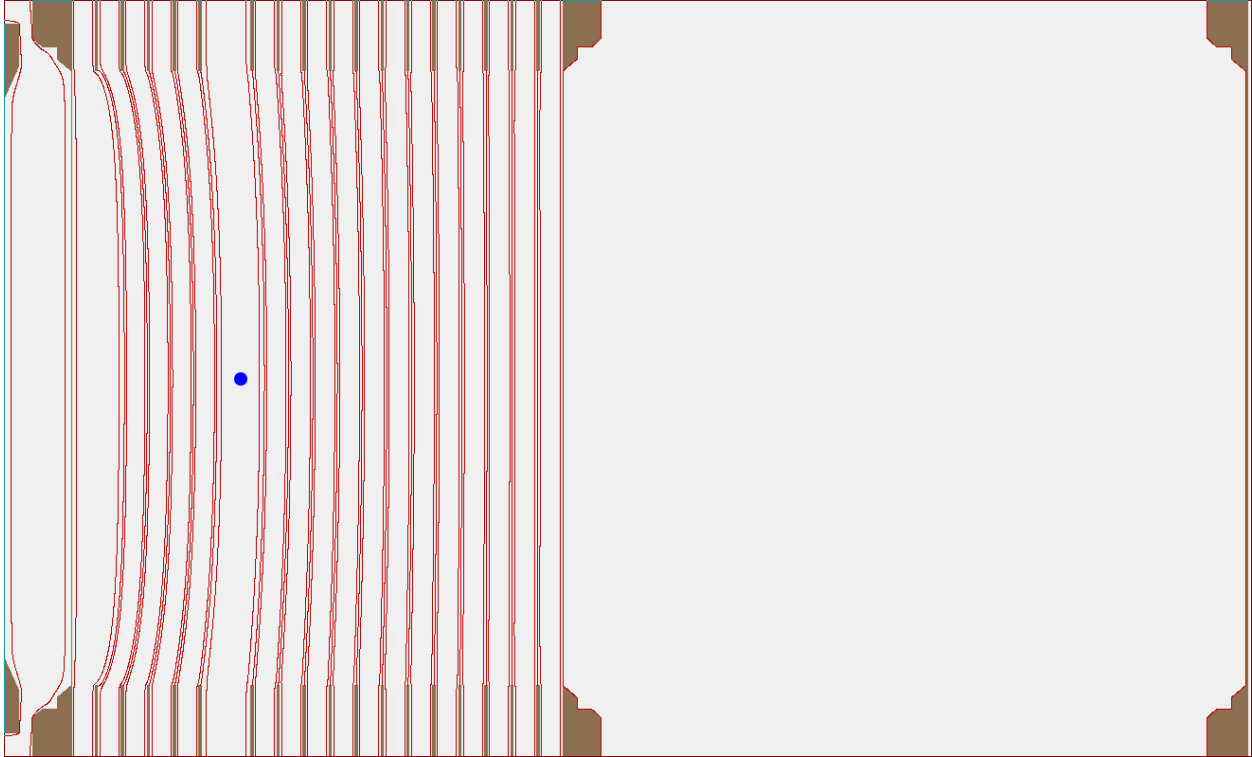
Figure 3.15: Spectrometer with simulated electric field lines. This simulation was carried out with Simion. The blue dot indicates the position of the interaction region

The spectrometer was simulated in Simion with the resistors that were actually installed in the spectrometer. The initial momentum was calculated from the results of the simulation. In the simulation, the true initial momentum of the fragments is known. The two different momentum values were then compared to see the type and extent of the distortion that resulted. In Fig.3.16 the two values are plotted and fitted. The lens caused a shift in the calculated P_x momentum. The calculated P_y momentum shows a similar, but less substantial trend.

This simulation does include the jet velocity in an attempt to be as realistic as possible. In the experiment, the photon beam does not pass through the center of the spectrometer; this is by design, but it is not included in the simulation. This is one of the reasons that the simulation does not yield the true correction values, but it does give the type of correction needed. The actual correction values used were found empirically from the raw momentum distributions of each
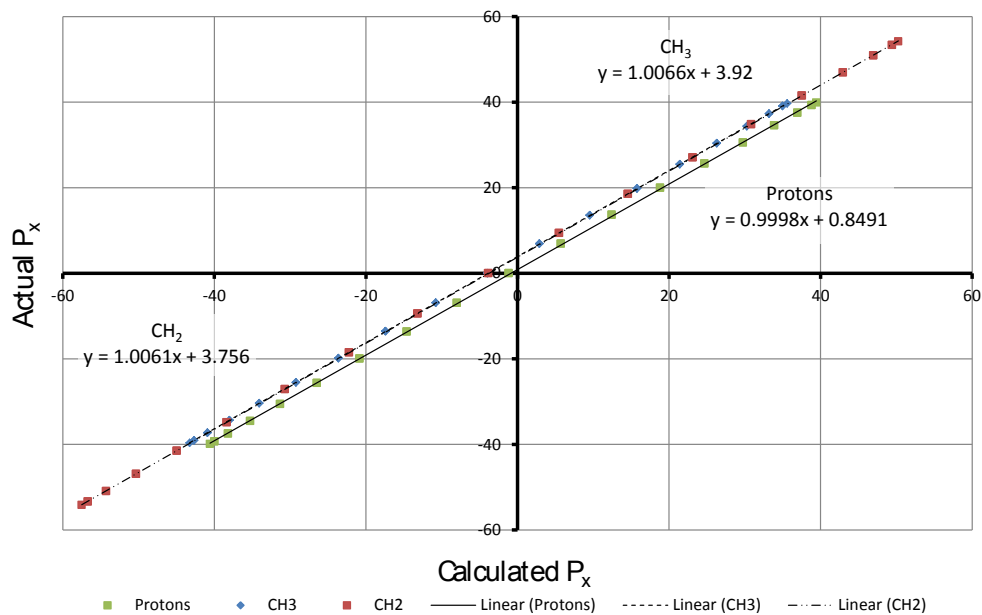
Figure 3.16: P_x momentum correction plot for selected ionic fragments. This is a comparison between the true initial momentum values used in the simulation and the calculated initial momentum, which were found from the final position and TOF from the simulation.
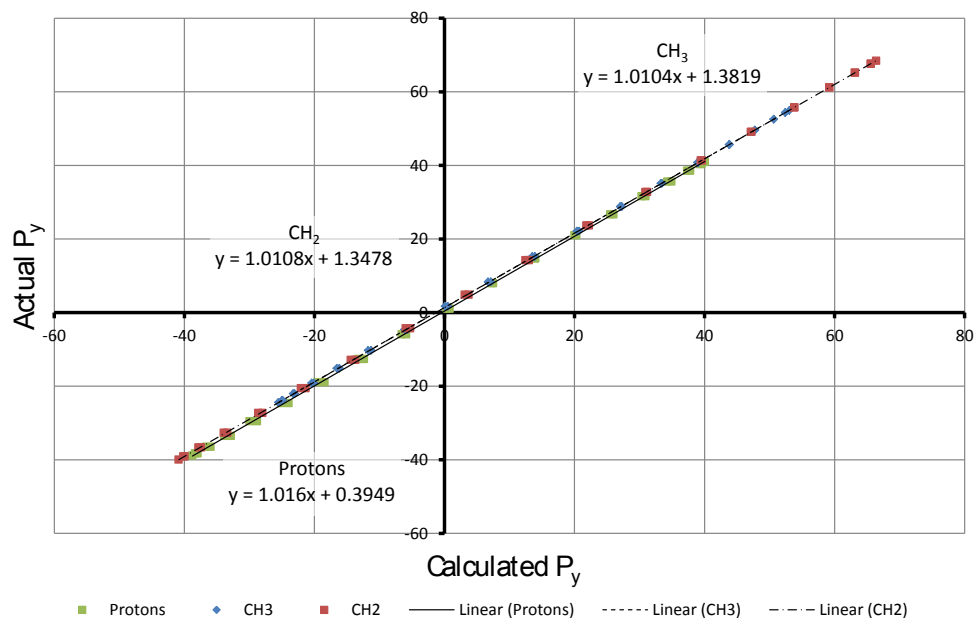
Figure 3.17: P_y momentum correction plot for selected ionic fragments. This is a comparison between the true initial momentum values used in the simulation and the calculated initial momentum, which were found from the final position and TOF from the simulation.
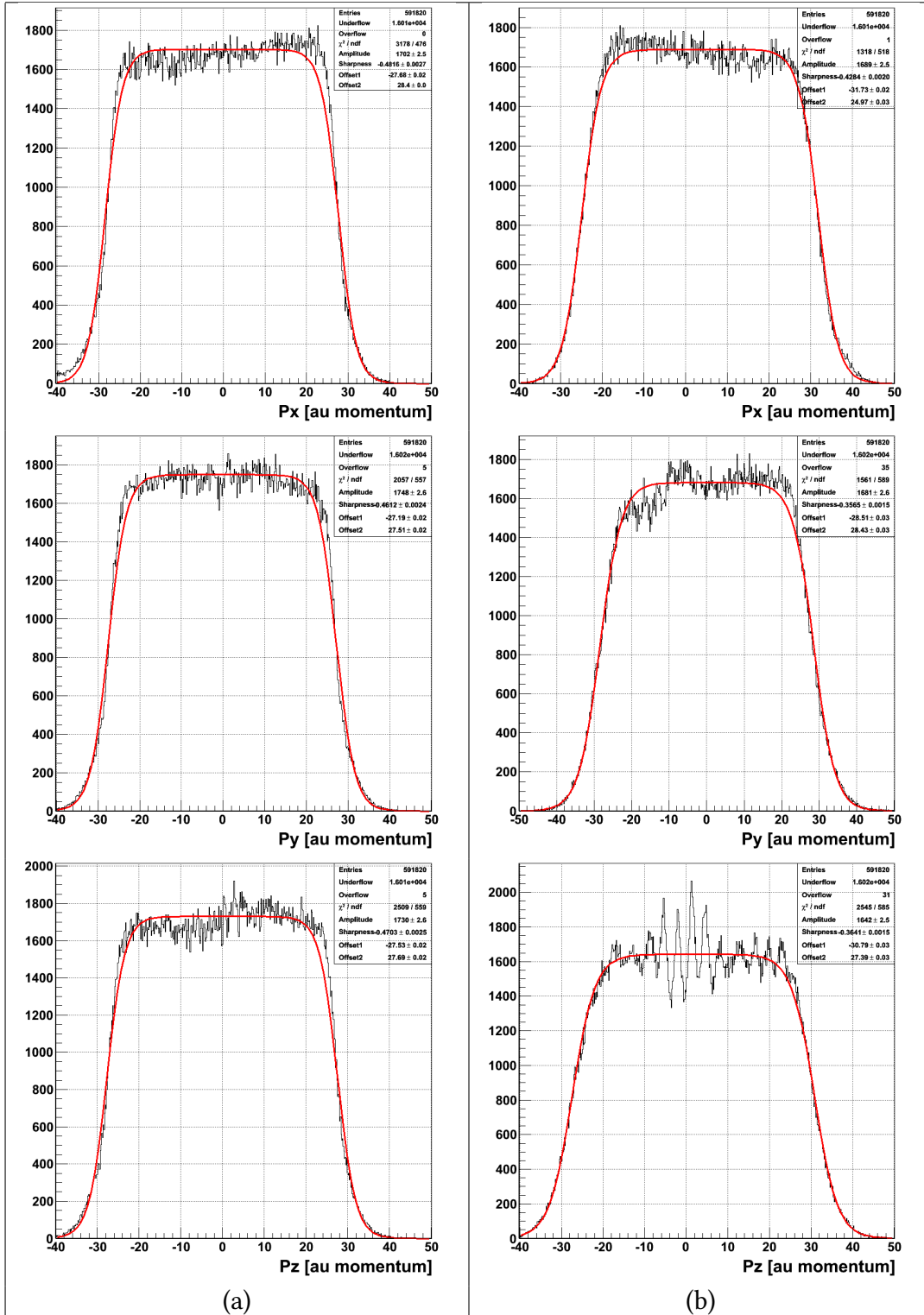
Figure 3.18: (a) Momentum Correction Plots for H^+ ion fragments from the $[H^+, CH_3^+]$ channel (b) Momentum correction plots for CH_3^+ ion fragments from the $[H^+, CH_3^+]$ channel.
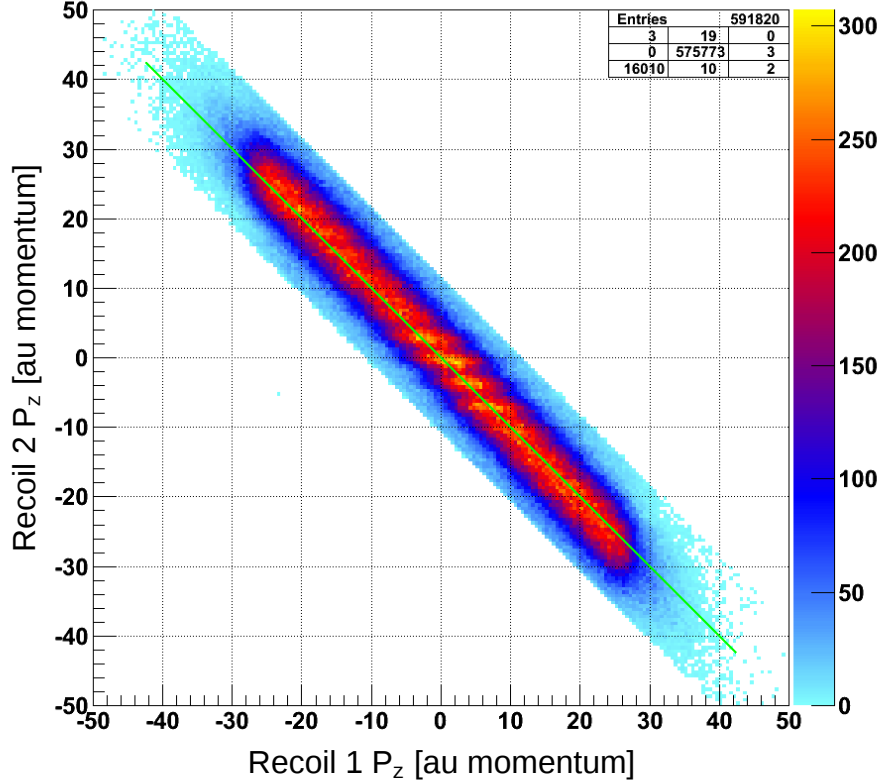
Figure 3.19: Corrected P_z momentum plot for the $[H^+, CH_3^+]$ channel. The green line is drawn through the origin at a -45° angle.

ionic fragment. Each distribution was fitted with a linear combination of two independent analytic approximations of the Heaviside step function, which is shown in Fig. 3.18. The momentum offset was found from the fitted function by averaging $x_{\circ 1}$ and $x_{\circ 2}$.

$$H(x) \approx A \left(\frac{1}{1 + e^{-k_1/2(x-x_{\circ 1})}} - \frac{1}{1 + e^{-k_2/2(x-x_{\circ 2})}} \right) \tag{3.4}$$

An example of the results can be seen in Fig. 3.19. This procedure was carried out for each fragmentation channel to determine the individual offset parameters.

This procedure produces acceptable results for the ions, but the electrons are more heavily distorted. The results from the simulation are shown in Fig. 3.20. This simulation suggests that a linear correction would be sufficient, but it could also be fit with a third order polynomial. The simulation indicates that there is no distortion in the P_y and P_z directions, at least for the 4.25 eV
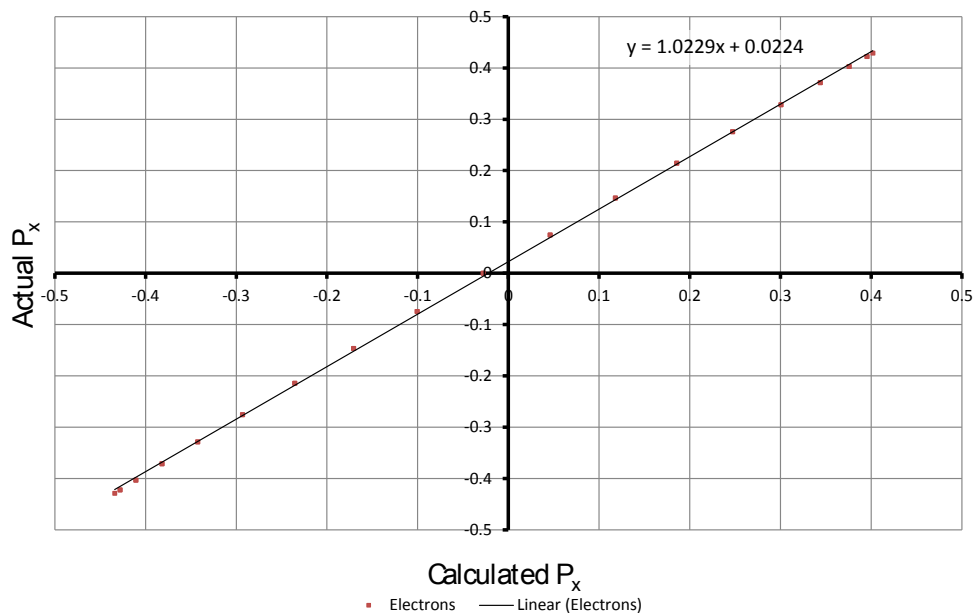
Figure 3.20: P_x momentum correction plot for electrons. This is a comparison between the true initial momentum values used in the simulation and the calculated initial momentum, which were found from the final position and TOF from the simulation.

photoelectrons. This does not actually appear to be true, as is visible in Fig. 3.23, but it is a small effect, and thus ignored.

Again the simulation does not produce valid correction values, but instead is used only to determine the type of correction that is necessary. The procedure used to determine the actual correction values is outlined below. Figure 3.21 is produced by requiring the electrons plotted to lie in the P_{yz} momentum plane. We next attempted to determine the edges of the P_x momentum distribution. This was done by projecting Fig 3.21 to make Fig. 3.22; these projections were limited to ±0.56 au in P_z. The projections were then fit with a Gaussian function, but it should be noted that this is a somewhat arbitrary fitting and we could have easily just picked the maximum. Projections were also done in the P_z directions to determine the undistorted radius of the momentum distribution, which is 0.55 au. This was also checked in the P_y and the two values agree to within four decimal places. This yields two equations and two unknowns, which when solved gives the following values,
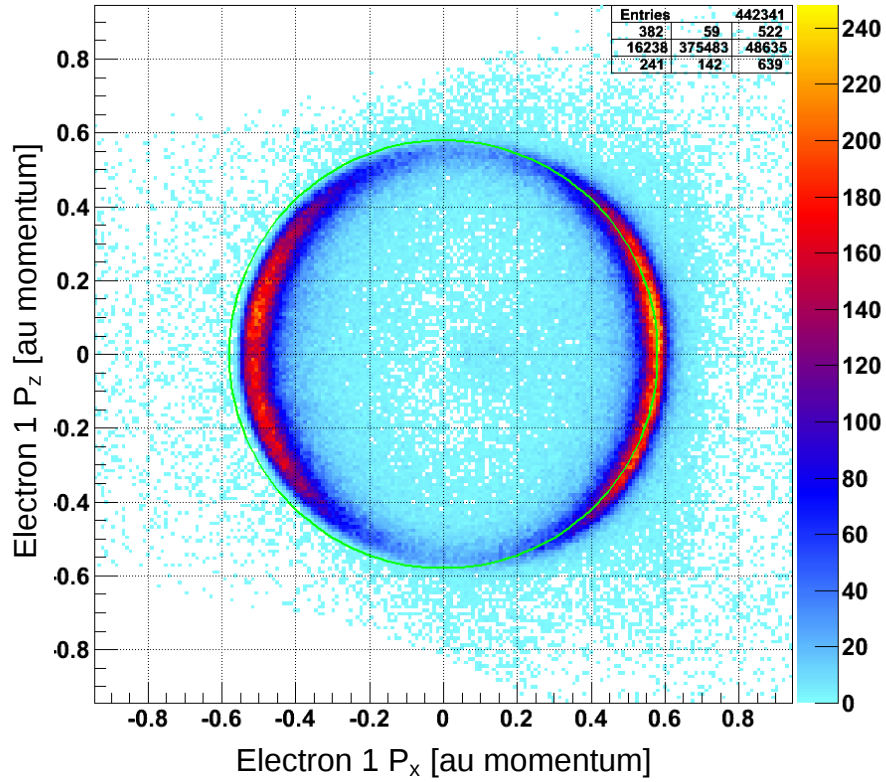
Figure 3.21: Plot of the first electron hit P_z vs. P_x, which is gated such that they lie in the XZ momentum plane. The green circle is centered on the origin and draw with a radius of Ø.57 au.

(a) Left Side

(b) Right Side
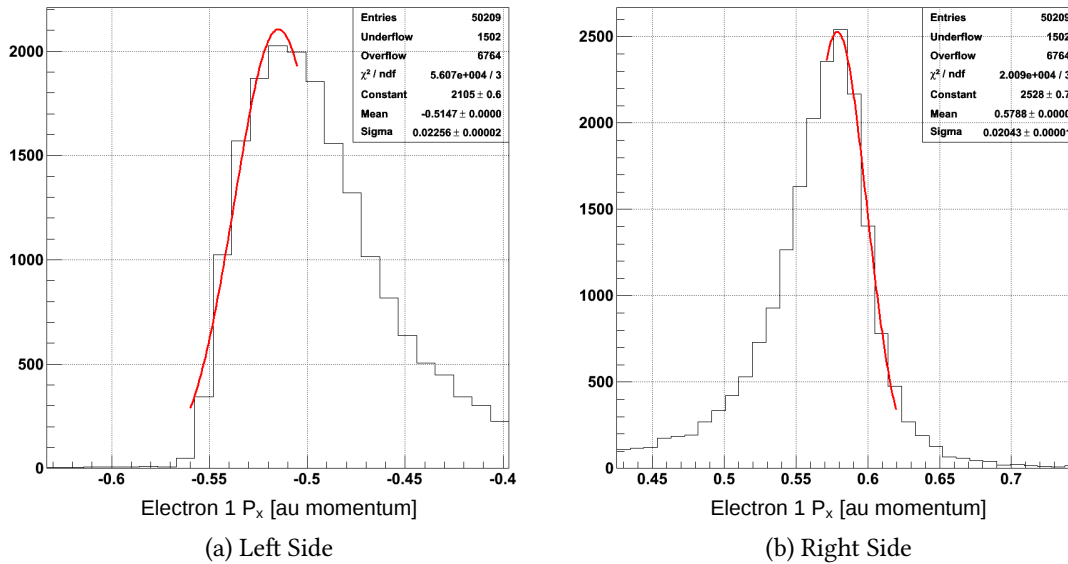
Figure 3.22: Projection of Fig. 3.21 limited to ±Ø.56 au P_z.
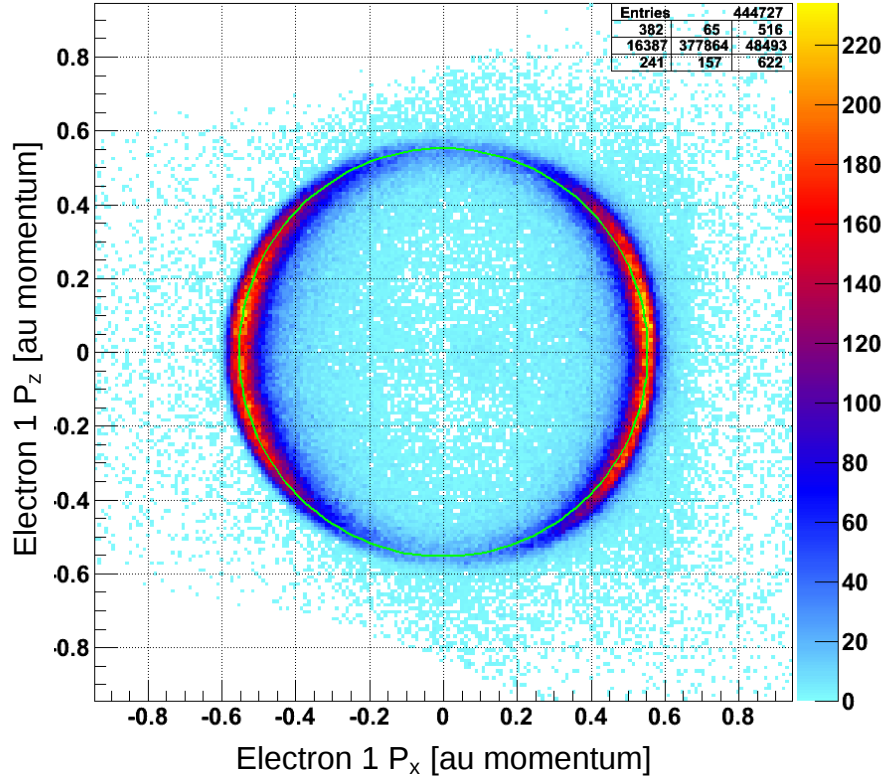
Figure 3.23: Plot of the corrected first electron hit P_z vs. P_x, which is gated such that they lie in the XZ momentum plane. The green circle is centered on the origin and draw with a radius of 0.55275 au.

$$\left.\begin{array}{l} 0.55275 = \text{M}(0.5788) + \text{B} \\ -0.55275 = \text{M}(-0.5147) + \text{B} \end{array}\right\} \longrightarrow \left(\begin{array}{l} \text{M} \to 1.01097 \\ \text{B} \to -0.0324017 \end{array}\right).$$

The corrected spectrum is shown in Fig. 3.23, which is a significant improvement over the uncorrected version. Note, the electric field distortion becomes worse the closer the electron approaches the ion side of the spectrometer. Electrons with positive P_x momentum values exhibit this effect. This electric field distortion causes the P_y and P_z to also be distorted, which can be seen in Fig. 3.23. This could also be corrected, but it was not worth the time costs necessary to correct it. This problem becomes more pronounced in the 15.25 eV data set, but again a correction to P_x was deemed sufficient.

Chapter 4

Results I: Molecular Imaging and Three Dimensional MFPADs

"There is a single light of science, and to brighten it anywhere is to brighten it everywhere."

—Isaac Asimov

4.1 Introduction

Imaging molecular structure is a critical challenge in chemical physics recently highlighted by the emergence of techniques that, like ultrafast electron diffraction[50] or X-ray diffraction[51], have the potential to be taken to the time domain and thereby ultimately be used to make "movies" of chemical reactions on their natural timescale. Of particular interest is the development of such techniques that can be applied to the dynamics of isolated molecules. Here, we report on a major step forward in one such approach, namely photoelectron diffraction. We present three-dimensional images of a polyatomic molecule measured with this technique, including evidence that demonstrates a general trend of low energy photoelectrons directly imaging the molecular potential and bond structure.

Photoelectron diffraction is a process where an electron wave is launched by photoabsorption at an inner shell. The outgoing photoelectron wave is then diffracted by the aggregate potential of the molecule. The final angular distribution of these electrons in the body fixed frame of the molecule (MFPADs) are exquisitely sensitive probes of molecular structure and initial electronic state, which has been recently argued and demonstrated[52,53]. However observing MFPADs at

high resolution requires accurate orientation of the molecule in the gas phase. Three-dimensional laser alignment[6,8] can accomplish such orientation prior to photoionization but is limited to molecules with an asymmetric polarizability. In the case of simple diatomic molecules, orientation can also be accomplished by detecting the photoelectron in coincidence with positively charged fragments that emerge following prompt Auger decay and dissociation[1]. Progress has also been made toward three-dimensional MFPAD measurement using coincidence detection and velocity map imaging[30]. Here we present photoelectron imaging of methane molecules, where *both* the photoelectron momentum and corresponding body-frame of the polyatomic molecule are fully determined in all three dimensions.

4.2   Single Auger Decay vs. Simultaneous Double Auger Decay

For many molecules including CH_4, core ionization opens a strong simultaneous double Auger decay channel that produces a trication that then can dissociate promptly to three positively charged fragments. Momentum imaging of those three fragments with the photoelectron in coincidence provides a direct and unambiguous measurement of the MFPAD for a polyatomic molecule through the simultaneous orientation of three axes for every ionization event detected. We demonstrate this concept here using K-shell photoionization [54] of the methane molecule as a prototype. We find the surprising result that for photoelectron energies below about 10 eV the photoelectron tends to be focused along the bond directions, and that when the MFPAD is averaged over all polarization directions the result can effectively image the geometry of the molecule.

We can verify that the $[H^+, H^+, CH_2^+]$ channel is the result of simultaneous double Auger decay by measuring the momentum distributions of the ejected electrons in coincidence with the ions. In Fig. 4.1 the bright rings correspond to photoelectrons, and in the channel $[H^+, H^+, CH_2]$ we see discrete lines corresponding to Auger decay into different electronic channels, while in channel corresponding to the breakup of the trication, $[H^+, H^+, CH_2^+]$, we see the energy sharing
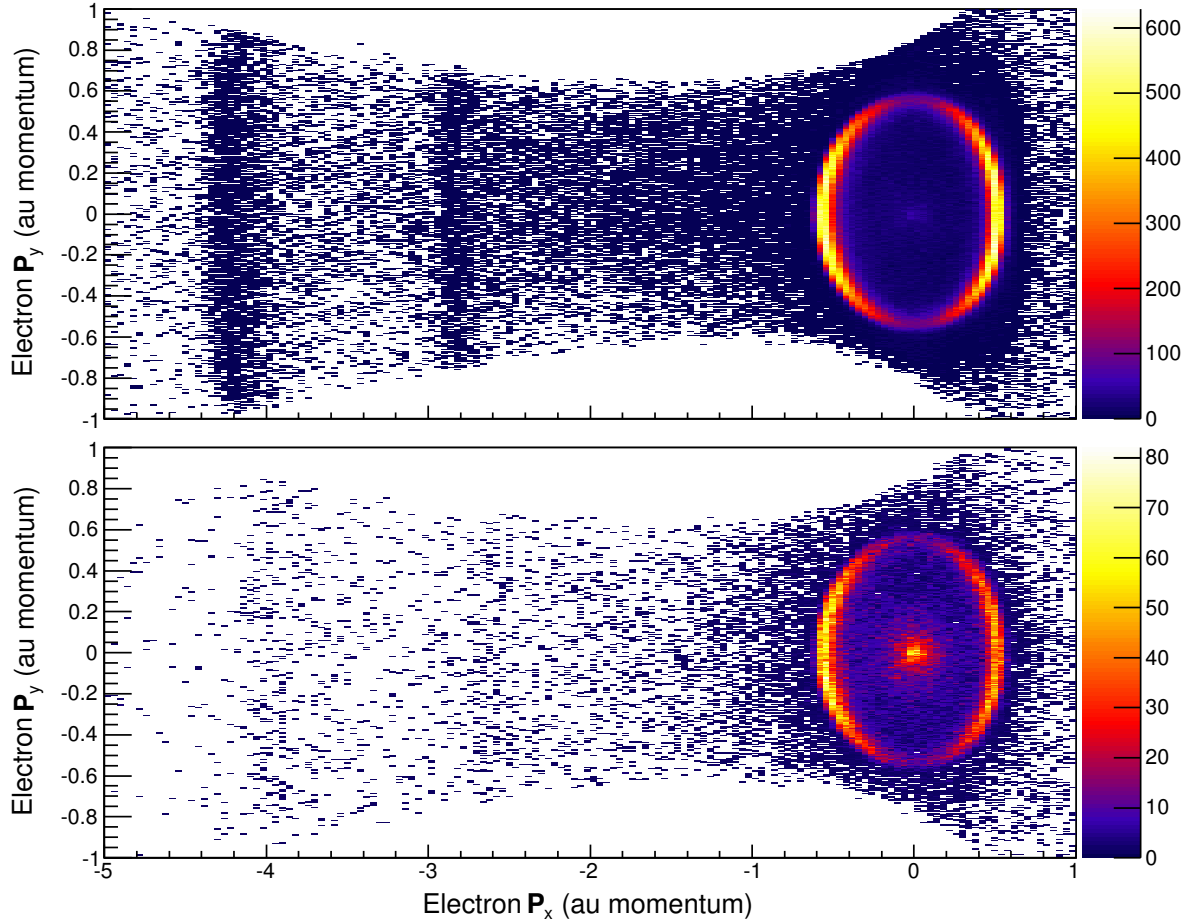
Figure 4.1: 2-dimensional electron momentum distributions with polarization along the x-axis. Top: measured in coincidence with the $[H^+, H^+, CH_2]$ channel and Bottom: measured in coincidence with $[H^+, H^+, CH_2^+]$ channel. Low energy electron signature at $p_x = 0$ from simultaneous double Auger decay is visible in lower panel, while upper panel shows discrete lines from single Auger decay at $p_x \simeq -4$.

between two simultaneously ejected electrons. In that case the energy sharing distribution is smooth but highly asymmetric[55] and peaks with one electron having nearly zero momentum (the bright dot at the center of the ring) and the other carrying most of the available energy corresponding to the decay to a particular electronic state of the trication.

4.3 MFPADs from the [H^+, H^+, CH_2^+] Following Simultaneous Double Auger Decay

In the cases of core ionization of methane the determination of the three dimensional orientation of the molecule has been greatly aided by the presence of direct double Auger decay that forms a triply charged cation within a few femtoseconds of the primary ionization event, and the prompt subsequent dissociation of the molecule into three charged fragments.

$$CH_4 + h\nu \quad \rightarrow \quad CH_4(1s^{-1}) + e^- \tag{4.1}$$

$$CH_4(1s^{-1}) \quad \rightarrow \quad CH_2^+ + H^+ + H^+ + 2e^-$$
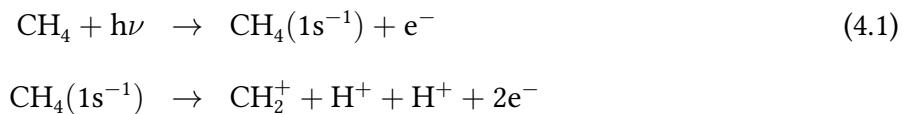
The observation of three ionic fragments in coincidence with the photoelectron using the cold target ion momentum spectroscopy (COLTRIMS) method[56,57] can then yield the angular dependence of photoejection in the molecular frame. The power of this approach when the simultaneous double Auger decay channel is observable has been demonstrated forcefully in the case of methane, and, with velocity map imaging, in the case of water.

Our collaborators, C.W. McCurdy, C. Trevisan and T. Rescigno, have calculated the theoretical MFPADs for methane shown here. The calculation of MFPADs requires a description of both the initial neutral electronic state of the molecule and the electron-ion scattering wave function for an electron scattering from the core-hole cationic state of the molecule. They used the complex Kohn variational method outlined in refs.[58,59] to calculate these MFPADs. This is covered in greater detail in Appendix B.1.

In order for coincidence measurements to reveal the orientation of a molecule following an ionization event, its dissociation must be prompt and essentially along the directions of the bonds that are ruptured by the loss of valence electrons. In the case of core or inner-shell photoionization followed by a single Auger decay, two valence electrons are lost in the final state and this
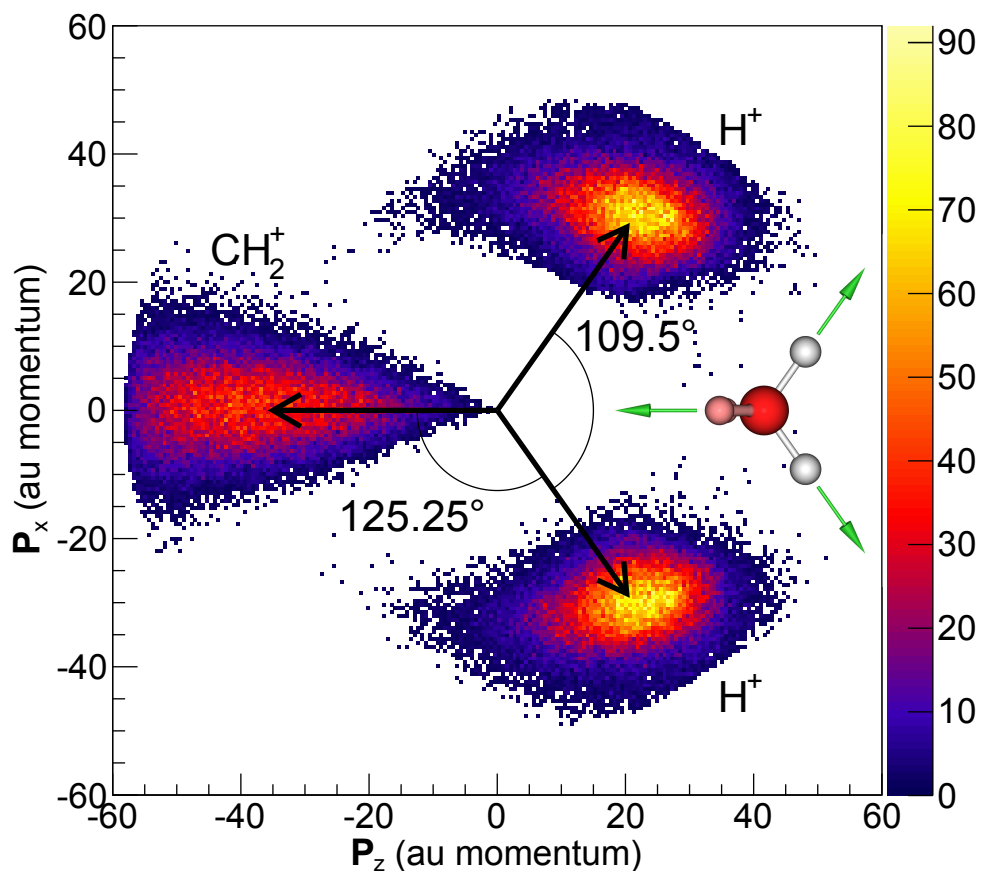
Figure 4.2: Fragment ion momenta in the $[H^+, H^+, CH_2^+]$ dissociation channel following simultaneous double Auger decay of core ionized CH_4^+.

condition, called "axial recoil" for diatomics may or may not be satisfied[2]. However because simultaneous double Auger decay is a strongly populated decay channel in methane, a substantial fraction of photoionization events produce a CH_4^{+++} trication from which three bonding electrons are missing. This highly unstable arrangement causes prompt dissociation dynamics where molecule fragments are directed along the ruptured bonds, as can be clearly seen in Fig. 4.2. The momentum vectors of the three fragments measured in coincidence peak very nearly along the bond angles for the H^+ fragments and bisecting the bond angle for CH_2^+. In this case, sequential Auger decay would proceed through the excited dication state with configuration $1a_a^2 1t_2^6$, but Hartree Fock calculations suggest that this pathway is energetically forbidden. Calculations at that level suggest a similar situation in NH_3 but not in water, where nonetheless simultaneous
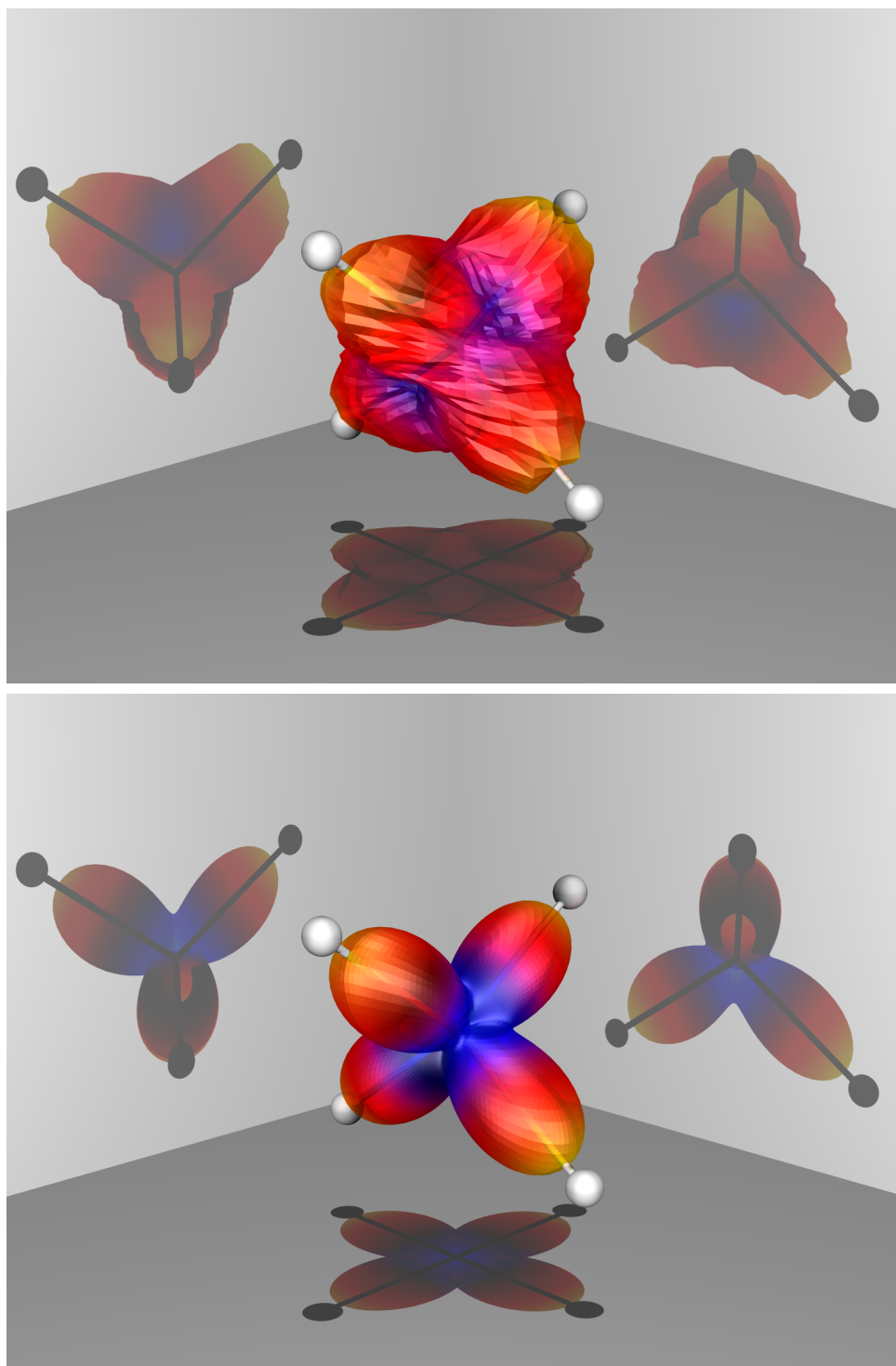
Figure 4.3: Methane imaged via the MFPAD for K-shell photoelectron. Equilibrium geometry shown to indicate molecular frame. Top: The experimental MFPAD obtained from the [H^+, H^+, CH_2^+] decay pathway. Bottom: Calculated MFPAD at 4.35 eV integrated over all polarization directions.

double Auger decay has apparently been observed[30]. Even in cases where simultaneous double Auger competes with Auger cascade, it may still be detectable in a coincidence measurement by

Figure 4.4: Theoretical (right) and experimental (left) MFPADs for particular orientations of the polarization axis in the molecular frame. Left Column: Polarization axis aligned to a C_2 symmetry axis. Middle Column: Polarization axis perpendicular to a C_2 axes and in the plane of two hydrogen bonds. Right Column: Polarization axis perpendicular to a C_3 axes along one bond and in plane with another bond.

selecting on ion momenta corresponding to direct breakup like those shown in Fig 4.2. Thus the class for which complete 3D MFPADs are measurable with these techniques is likely to include many small molecules.

Each row of panels in Figure 4.4 and Figure 4.7 corresponds to experiment (left) and theory (right) for the MFPADs arising from specific orientations of the molecule relative to the polarization axis. The top row corresponds to the polarization axis along the C_2 axis of symmetry, bisecting two hydrogen bond axes. In the middle row the polarization axis is perpendicular to C_2 axes and constrained to the plane of two hydrogen bonds. In the bottom row the polarization axis is perpendicular to C_3 axes and is in the plane with a hydrogen bond. Even at this higher level of differentiation, we still find excellent qualitative agreement with the theoretical calculations, giving us confidence that we can use the calculations as a tool to elucidate fragmentation dynamics in more complicated dissociation pathways.

4.4   High resolution MFPADs from observation of photoelectron in coincidence with two protons

One of the measured channels corresponded to the detection of two H^+ ions in coincidence with no third fragment. The possible dissociation pathways that give rise to this are either (1) the $[H^+, H^+, CH_2^+]$ double-Auger channel where the third fragment wasn't detected or (2) the more probable $[H^+, H^+, CH_2^0]$ single-Auger channel where the neutral fragment is always lost. Figure 4.5 shows the momentum space distribution of the two hydrogen ions in the frame defined by their momentum sum. The horizontal and vertical axes correspond to the perpendicular and parallel components respectively. The data for the first hit on the detector is shown in the upper half of the figure, and the data for the second hit is shown on the lower half. There are clearly two islands separated by slightly more than the neutral ground state bond angle of $109.5°$. We

interpret this result to be due to ejection along the bond axes along with broadening of the angle due to the Coulomb repulsion of the two ions. Also evident in the figure are the gates set around these islands in order to discriminate against contaminant random events (background). These gates were set broad enough to include the locus points where the island edges met the background.

Because of the high symmetry of CH_4, we were able to fully determine the orientation of the molecule with only these two vectors. This allowed the determination of the molecular frame angular distributions (MFPADs) shown in Figs. 4.6 and 4.7. These figures show the angular distribution in three dimensions by displaying intensity as both the radial coordinate and as a color map range from weak or blue to strong or orange. In each case we present a comparison between the complex Kohn variational calculation and the experimental result, and in all cases,
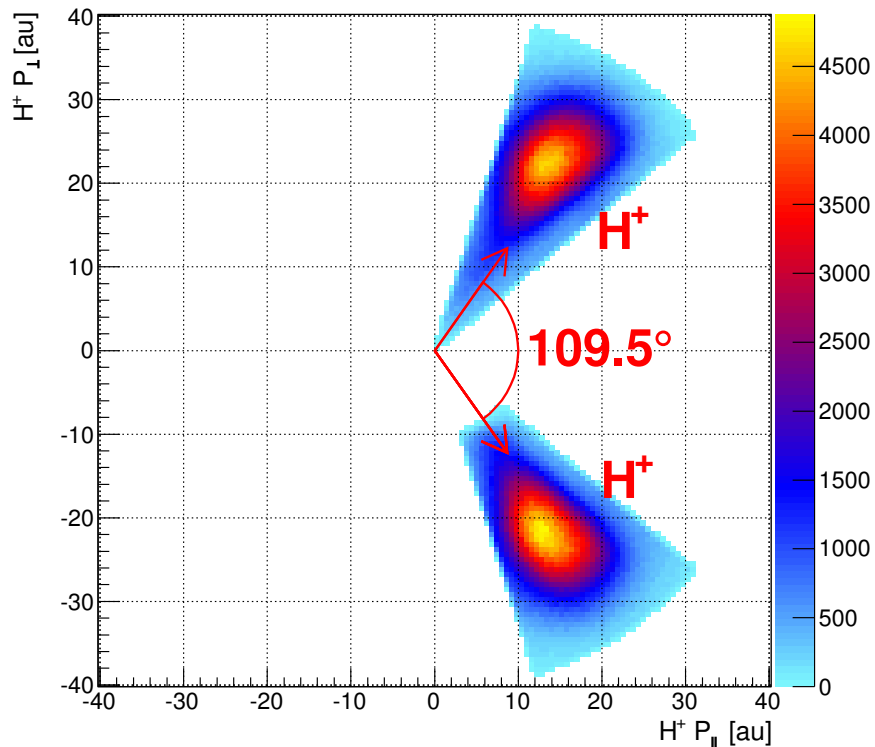
Figure 4.5: Ejected H^+ fragment momenta plotted in the frame defined by the vector components parallel and perpendicular to the momentum sum or C_2 axis of symmetry. Gates were placed around these two "islands" in order to discriminate signal from background.
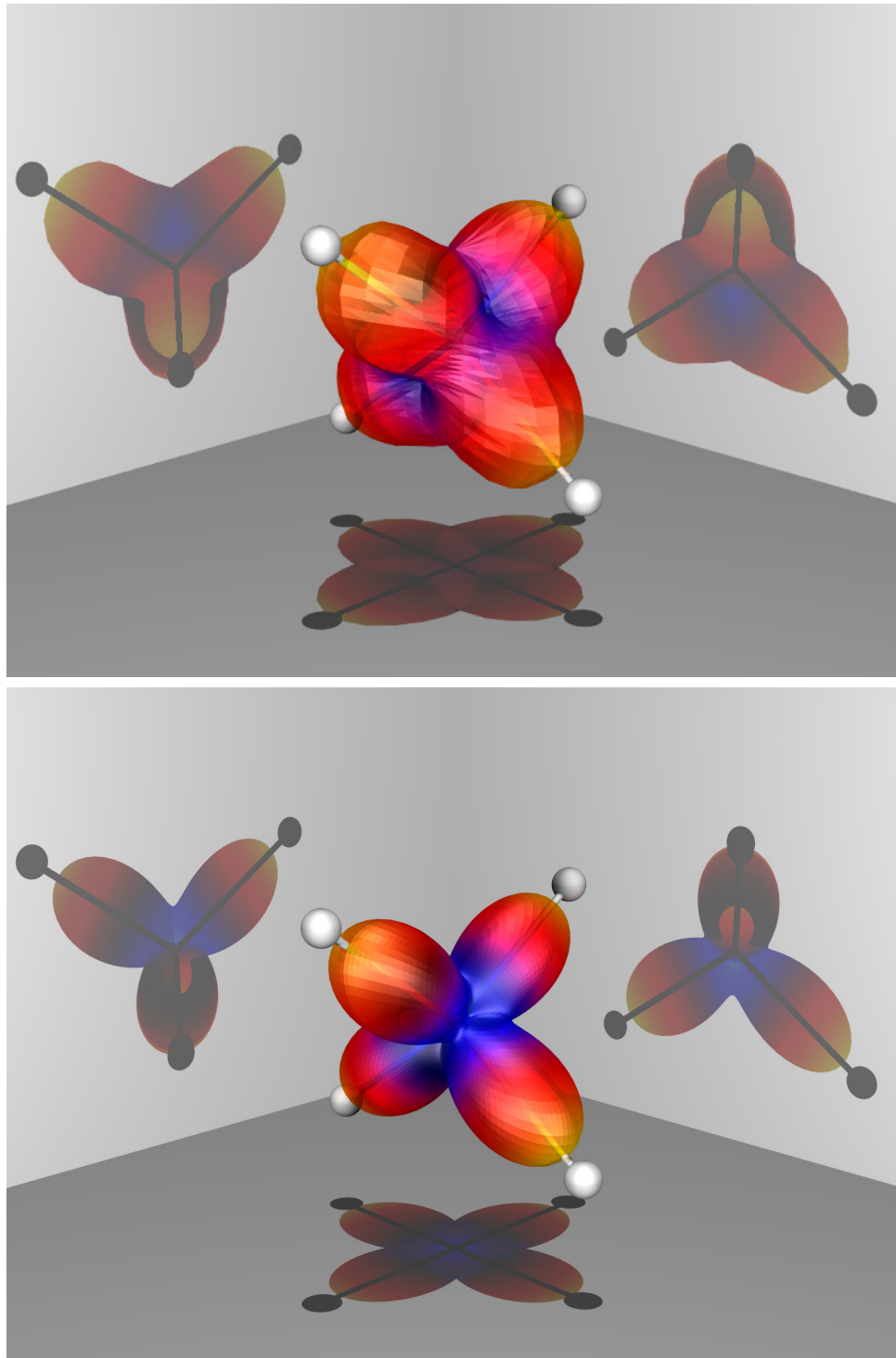
Figure 4.6: MFPAD for K-shell ionization in CH_4 observed (top) in coincidence measurement with $H^+ + H^+$ following Auger decay, and calculated (bottom) using the complex Kohn variational method. Data and theory are integrated over all orientations of the polarization vector.

the agreement is excellent. The discrepancy arises due to a combination of (1) the broad gating and binning of the statistics limited experimental data, (2) the quite complicated angular resolution of the measurement due to the variation of the momentum resolution through the momentum space and (3) the zero-point vibrational motion of the molecule. There is no clear way to unfold all of these, so we have chosen to present the theoretical and experimental as they stand, which we consider sufficient for a insightful comparison.

Figure 4.6 shows the MFPAD where we have integrated over the polarization direction revealing only the contribution of the molecular potential to the electron angular distribution. If there were no influence of the molecular potential, then this distribution would be isotropic. However, we see here the striking result that for this photoelectron energy, the ejected electrons tend to emerge along the bond axes. The mechanism for this apparent focusing of the outgoing electron wave by the bonds is not fully understood at this time, but it has been predicted in two isolectronic molecules, NH_3 and H_2O, by complex Kohn variational calculations like those presented here[60].

4.5   Results & Conclusions

At photoelectron kinetic energies below about 10 eV, however, we find more than just the symmetry of the molecule in both the experimental and theoretical MFPADs for methane shown in Fig. 4.3 and Fig. 4.6; we find an image of the geometry of the molecule revealed by apparent focusing of the outgoing electrons towards the protons. If the MFPAD in Eq.(B.1) is integrated over all polarization directions the resulting photoelectron distribution in the molecular frame must show the symmetry of the molecule. This surprising result is also suggested by Kohn variational calculations of the MFPADs for core ionization of ammonia (not shown), and we speculate that for sufficiently low kinetic energies core ionization MFPADs may provide a general way to monitor the geometry of small molecules at the time of photo-ejection. Fig. 4.3 shows the results
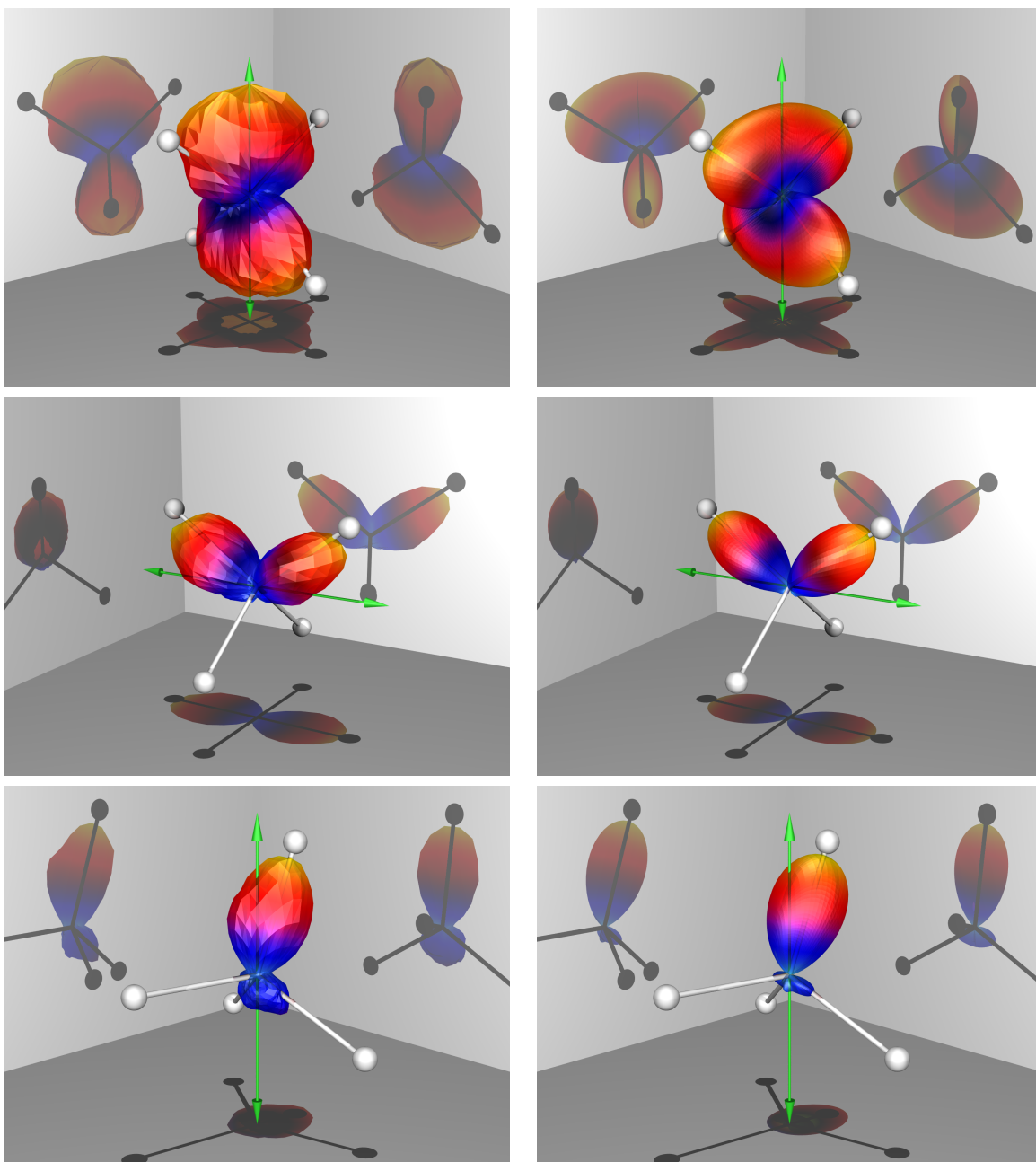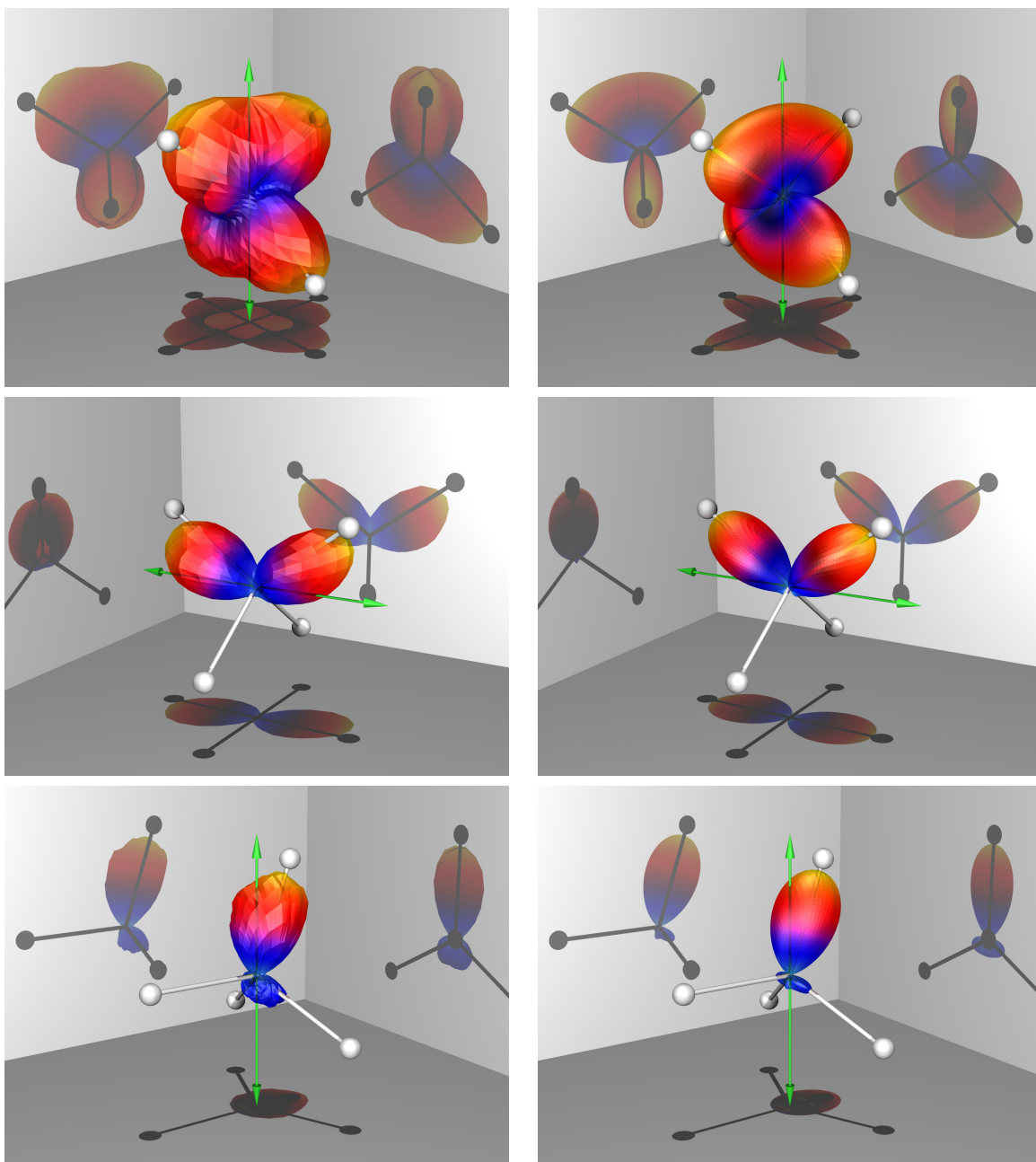
Figure 4.7: Theoretical (top row) and experimental (bottom row) MFPADs for particular orientations of the polarization axis in the molecular frame. The experimental data for the $[H^+, H^+, CH_2]$ two-body channel. (Left Column) The polarization axis is aligned to the C_2 symmetry axis. (Middle Column) The polarization axis is perpendicular to C_2 axes and constrained to the plane of two hydrogen bonds. (Right Column) The polarization axis is perpendicular to C_3 axes and is along another hydrogen bond.

of measurement of the MFPAD in the trication channel, $[H^+, H^+, CH_2^+]$, which is the general procedure we propose for 3D MFPAD measurements when simultaneous double Auger decay can be

detected. At this resolution we must ask what causes the remaining small differences between theory and experiment, and the apparent answer is that the nodes in the theoretical MFPAD (computed at the equilibrium geometry only) are filled in by changes in the MFPAD due to zero point vibrational motion of the molecule.

Low energy (4.35 eV) MFPADs with the polarization at various angles relative to the molecule shown in Fig. 4.4 demonstrate a competition between two effects that primarily determine the shapes of the MFPADs. The first is the evident focusing of the outgoing electrons in the directions of the bonds by the molecular potential. The second is the initial $1s \rightarrow \epsilon p$ transition that sends the electron out along the axis of polarization. More specifically, the cross sections are each coherent combinations of the x, y, z components of the dipole transition amplitude in Eq.(B.1), and as such are expected to be even more sensitive to the molecular geometry than the incoherent sum that determines the MFPAD in Fig. 4.3. Nonetheless, the agreement between theory and experiment is nearly exact, and this fact suggests that it may be generally sufficient to apply the relatively simple approximation used here in which the scattering wave function for the ejected core electron can be computed by a single channel, static-exchange treatment – even though the interesting energy range is below 10 eV.

We see additional evidence for the energy dependent influence of the molecular potential in Fig. 4.8, which shows the MFPAD for 15.2eV photoelectron energy for a molecule oriented relative to the polarization axis. The distribution is essentially dipole in nature, indicating that the molecular potential has little apparent influence over the photoelectron emission for this case.

The results presented here suggest that 3D MFPADs from core ionization can be used as a probe of molecular geometry in ultrafast time-dependent measurements of molecular dynamics, whether the molecule is laser aligned or oriented by coincidence measurements following simultaneous double Auger decay. The dissociation dynamics following simultaneous double Auger
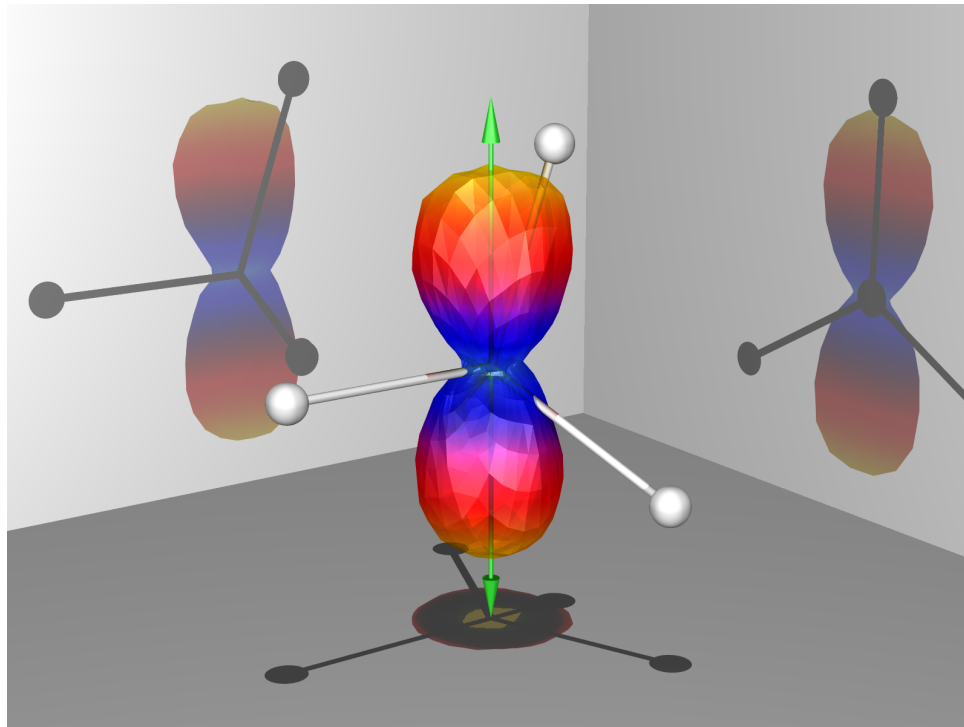
Figure 4.8: MFPAD for the case of large photoelectron energy ($\simeq 15.2$eV) following simultaneous double Auger decay of core ionized CH_4^+. Here the molecular potential has little influence on the dipole distribution of the photoelecton.

decay leading to a trication with three missing valence electrons can be expected to more frequently be direct and prompt than the case of single Auger decay and therefore provide a general tool for 3D molecular orientation.

Chapter 5

Results II: Dissociation dynamics of H^+ + CH_3^+ following Auger decay

"Some dreamers demand that scientists only discover things that can be used for good."

—John Charles Polanyi

5.1 Introduction

The measurement of molecular frame photoelectron angular distributions (MFPADs) promises to become a general technique to probe molecular and electronic dynamics in ultrafast experiments. It is important therefore to develop an understanding of the various ways in which MFPADs can be sensitive to both a molecule's structure and its electronic state. Both theoretical and experimental studies are exploring this question[52,53], and in the previous chapter that in some cases the MFPAD for core electron photoejection, averaged over all photon polarizations, can effectively image the geometry of a polyatomic molecule in three dimensions, with the outgoing electron effectively focused along the bond directions.

In this chapter we pursue the question of how the measurement of MFPADs for polyatomic molecules in momentum imaging experiments can reveal aspects of molecular dynamics when the photoionization event is followed by dissociation of the molecule. To measure an MFPAD, the gas phase molecule must be oriented accurately in the lab frame. Such orientation can be accomplished prior to the ionization by laser alignment[6,8]. The orientation of the molecule at the time of photoionization can also be determined in the case of core or inner shell ionization

by detecting the photoelectron in coincidence with positively charged fragments that emerge following prompt Auger decay and dissociation of the molecule[1]. For polyatomic molecules the complete determination of molecular orientation has recently allowed the measurement of three dimensional MFPADs in the cases of methane[61] and perhaps water[30].

The single Auger decay process, which in this case can yield other ionic dissociation channels,

$$
\begin{aligned}
CH_4(1s^{-1}) \quad &\rightarrow \quad CH_2 + H^+ + H^+ + e^- \\
&\rightarrow \quad CH_3^+ + H^+ + e^- \\
&\rightarrow \quad CH_2^+ + H_2^+ + e^-
\end{aligned}
\tag{5.1}
$$
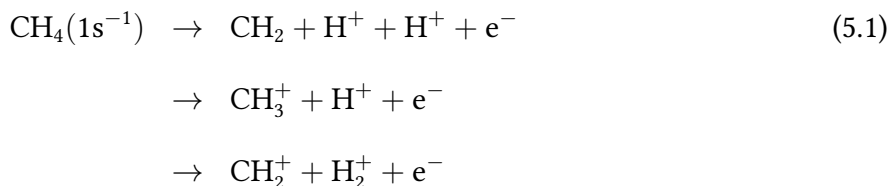
etc., can also yield MFPADs as well as information about the dynamics of these dissociation pathways. These decay channels and many others have been studied before in experiments that observe the Auger electron in coincidence with the ionic fragments[22,62,54]. In this study we build particularly on the previous work of Kukk et al.[22] as we focus here on the first two of these processes following core ionization of methane.

The central question that determines if coincidence measurements in these channels yield information on the orientation of the molecule is whether or not the dissociation dynamics are prompt and the fragmentation occurs essentially along the directions of the bonds in the molecule. This condition, called "axial recoil" for diatomics may or may not be satisfied, even for diatomic molecules[2] which can rotate before dissociating in some cases. Polyatomic molecules can bend or rearrange bonds during dissociation, and such dynamics have been seen in COLTRIMS and other momentum imaging measurements[63,64,65]. Thus polyatomic molecules have many more ways to fail the test of prompt and direct dissociation along the bonds being ruptured. Even in those cases, however, COLTRIMS measurements of the apparent MFPADs, combined with their theoretical prediction, can help elucidate the mechanisms of ionic dissociation.

The second channel in Equation (5.1) displays direct dissociation along a bond at some values of the kinetic energy release (kinetic energy of the fragments in the center of mass frame of the molecule) but not at others. Nonetheless the combination of experimental observations of the apparent MFPAD in that channel, combined with theoretical calculations using the Complex Kohn variational method and quantum chemical calculations of the potential curves for dissociation of CH_4^{++} in various electronic states yields strong evidence for how the dissociation in that channel occurs and which electronic states are involved.

5.1.1 Evidence for different dissociation mechanisms and dynamics at different kinetic energy releases

The measured channel corresponds to the two-body fragmentation of the CH_4^{2+} dication into the $[CH_3^+, H^+]$ dissociation pathway. The momentum measurement of this channel only defines a single axis, so we are limited to comparing experiment to theory where we have integrated the calculation about the azimuthal angle relative to the broken bond axis. Doing so produced the surprising result found in Figure 5.1, where recoil frame photoelectron angular distributions (RFPADs) in the hydrogen recoil frame show an essentially dipole distribution for low KER and agreed better with theory for high KER. We attribute this result to the contribution to this fragmentation channel from at least the two decay pathways described in Section 5.1.2 below. If in one of the pathways (low KER) the molecule is distorted or the dication lives for a long time, then the direction of the ejected H^+ momentum will not correspond to the H bond axis. These observations lead us to the conclusion that the axial recoil approximation (in the sense of prompt dissociation along the bond being ruptured) appears to be valid for the high KER part of this channel but not for the sharper lower energy feature in the KER spectrum.

The 3D MFPADS from the $[CH_2^0, H^+, H^+]$ channel seem consistent with that interpretation also, since the same MFPAD seen in this channel (averaged over rotations of CH_3^+ fragment
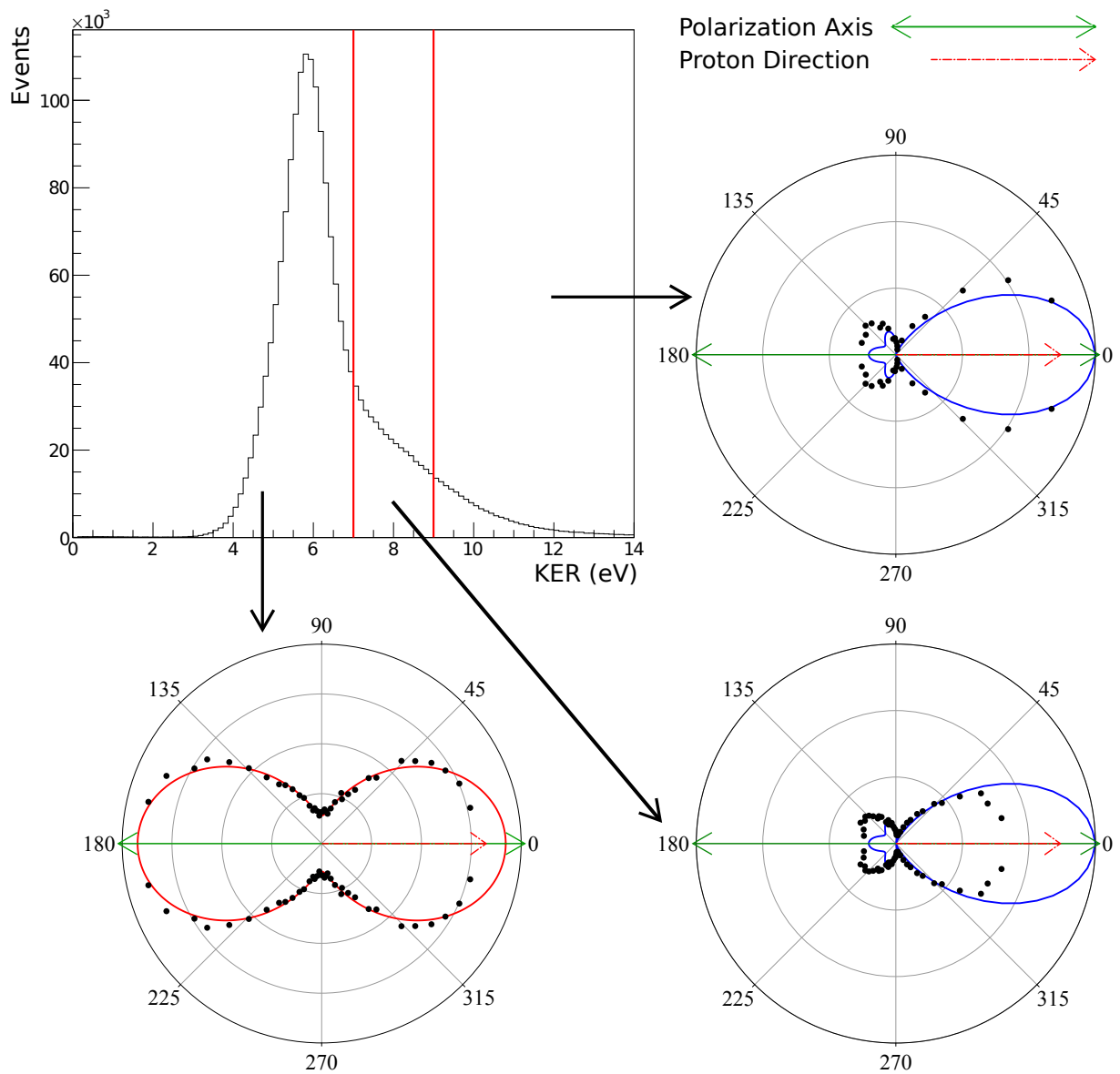
Figure 5.1: KER spectrum and RFPADs from measurements in $[CH_3^+ + H^+]$ channel with polarization along the recoil axis. The data are gated into three regions of KER: (I) less than 7 eV, (II) between 7 and 9 eV, and (III) above 9 eV. Using data for KER less than 7 eV produces the symmetric dipole shaped RFPAD at the left, indicating a severe breakdown of the axial recoil approximation. For increasing values of KER, the measured RFPAD shows improving agreement with theoretical prediction.

around the C_3 axis) can be extracted from that channel as well. The question is: why does axial recoil apply only to the high KER portion of the process? Comparisons between theory and experiment, using the theory plots collected in Figure 5.2 and Figure 5.3 will be part of that discussion.
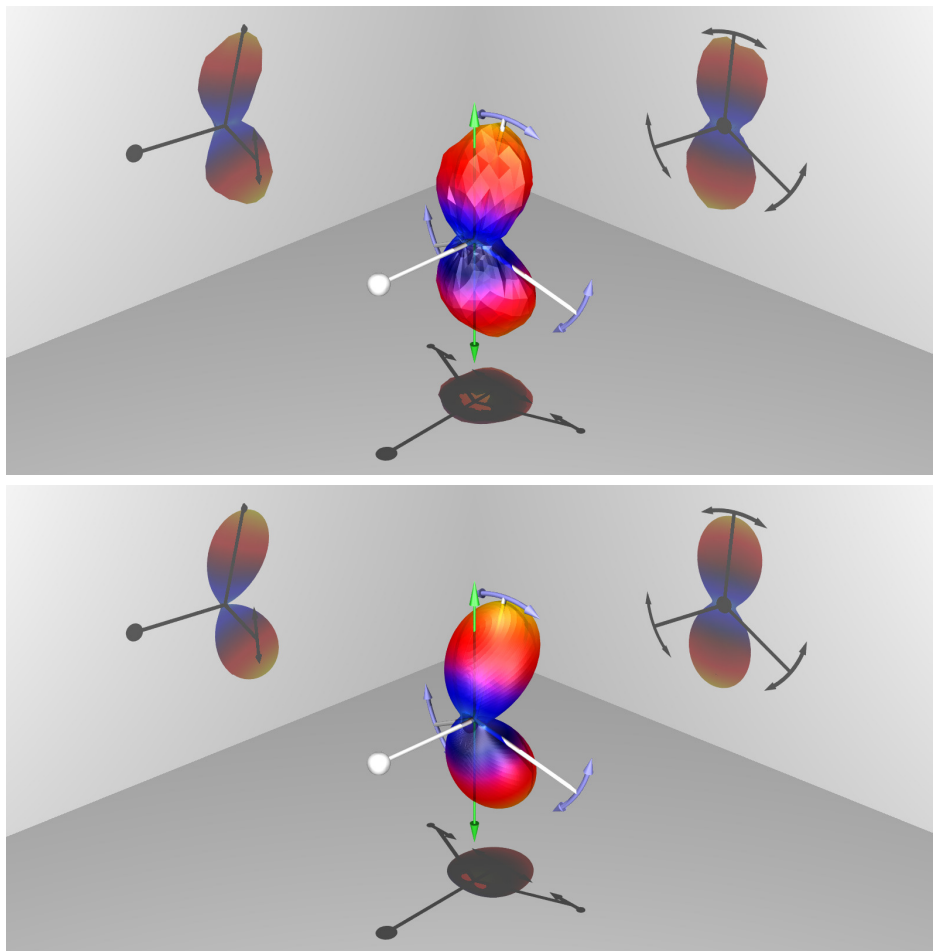
Figure 5.2: Experimental (top) and theoretical (bottom) MFPADs from complex Kohn variational calculations, averaged around C_3 axis of methane. Green arrows denote the direction of polarization. The orientation average was performed around the CH bond which projects to the left in each panel, and thus the three hydrogens to the right were rotated around that bond to produce the averaged MFPADs (RFPADs) shown here. Graphs shown here are form the 4.2 eV electron energy dataset and gated on the higher KER region.
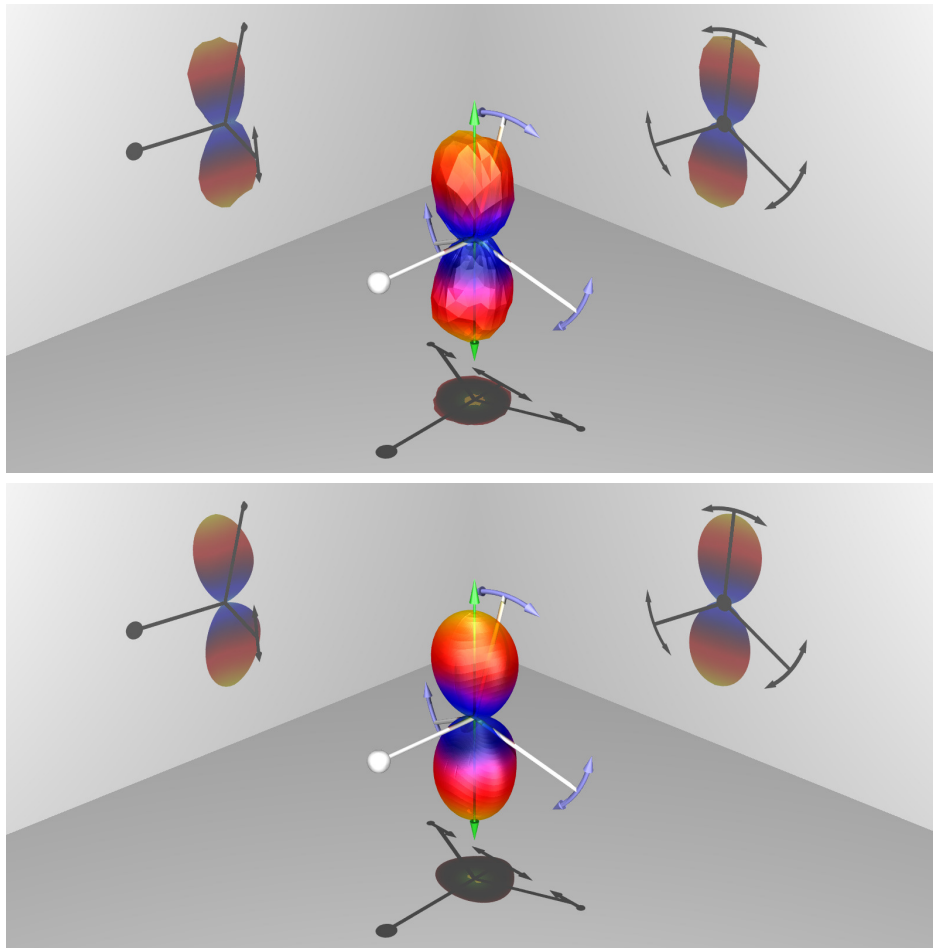
Figure 5.3: Experimental (top) and theoretical (bottom) MFPADs from complex Kohn variational calculations, averaged around C_3 axis of methane. Green arrows denote the direction of polarization. The orientation average was performed around the CH bond which projects to the left in each panel, and thus the three hydrogens to the right were rotated around that bond to produce the averaged MFPADs (RFPADs) shown here. Graphs shown here are form the 16 eV electron energy dataset.

5.1.2 Electronic structure calculations and the identification of pathways to dissociation in states of CH_4^{++}

The RFPADs observed in the breakup leading to $[CH_3^+ + H^+]$ shown in Figures. 5.2 and 5.3, along with Figure 5.1, immediately raise the questions: Why does the axial recoil approximation evidently break down for KER values near the peak near 6 eV, while for higher KER values in the same arrangement the dissociation is apparently prompt and does satisfy axial recoil? And also,

what states of the product CH_3^+ are being produced? To at least partially answer those questions our collaborators, C.W. McCurdy and C. Trevisan, have performed calculations of portions of the potential surfaces for relevant states of the CH_4^{++} ion that can be produced by Auger decay.

Our point of departure is a result of Kukk et al.[22]. By measuring the energies of Auger electrons in coincidence with the ionic fragments, these workers were able to give compelling evidence in 2007 that the the CH_3^+ fragment originates from the ^{1}E state of CH_4^{++} in tetrahedral geometry and that the same state produces CD_3^+ from dissociation of CD_4^{++}. The C(1s^{-1}) hole state of the molecule is created with a vibrational progression with only the symmetric stretch appreciably populated that has been observed to include the v = 0, 1, and 2 vibrational states[21,20]. So we can assume that core photoionization and subsequent Auger decay occur in our experiments near the tetrahedral geometry of the neutral methane molecule.

In the tetrahedral (T$_d$) equilibrium geometry of neutral methane, far from the planar equilibrium geometry of the dication[66], the dominant electronic configuration of CH_4^{++} is 1a$_1^2$ 2a$_1^2$ 1t$_2^4$. This configuration gives rise to four states with the term symbols ^{3}T$_1$, ^{1}E, ^{1}T$_2$, and ^{1}A$_1$. Figure 5.4 shows the results of state-averaged multiconfiguration self consistent field (MCSCF) calculations for a number of electronic states of the methane dication as one CH bond is stretched while the rest of the molecule remains in the equilibrium geometry of the neutral. The vertical line marks the point of T$_d$ symmetry and the four dication states are labeled near where they intersect that line. The details of these calculations are discussed in Appendix B.2, so here we focus on the calculated potential curves and what they suggest about the dynamics of the dissociation of the methane dication.

When one C-H bond in CH_4^{++} is stretched the symmetry of the molecule is reduced to C$_{3v}$ and the 9 individual spatial components corresponding to the ^{3}T$_1$, ^{1}E, ^{1}T$_2$ and ^{1}A$_1$ states in T$_d$ symmetry split into ^{3}A$_1$, a ^{3}E, two ^{1}A$_1$ and two ^{1}E states in C$_{3v}$ symmetry. Figure 5.4 shows that three of those states rise in energy as one CH bond is stretched and thus cannot, at least directly,

dissociate into the $CH_3^+ + H^+$ channel. The remaining three, of ^{1}E, ^{3}E and ^{1}A$_1$ symmetry are dissociative.
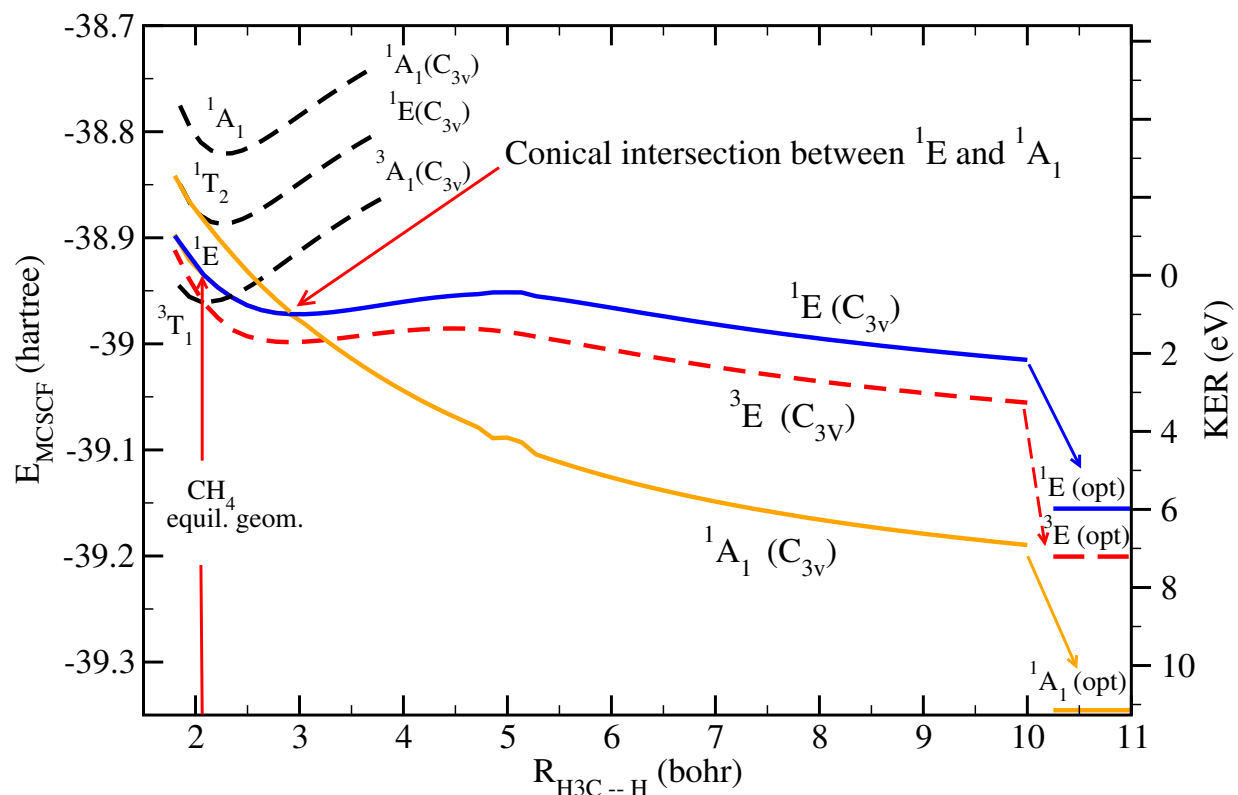
Figure 5.4: Potential energy curves from MCSCF calculations for the dissociation $CH_4^{++} \rightarrow CH_3^+ + H^+$ channel. Curves are with CH_3^+ fragment fixed at the geometry of methane. Asymptotes indicated by arrows are with CH_3^+ in the minimum energy geometry for each state. The kinetic energy release values on the right are for dissociation beginning on the ^{1}E state at the tetrahedral equilibrium geometry of neutral methane indicated by a red arrow. The black dashed curves that are not dissociative.

We see from Figure 5.4 that the ^{1}E state identified by Kukk et al.[22] to be responsible for this dissociation can dissociate directly, by passing over the slight barrier in the calculated curves, but that it has a symmetry allowed crossing (conical intersection) with the ^{1}A$_1$ state that is also dissociative. The dissociative curves in Figure 5.4 are calculated with the CH_3^+ fragment frozen in the geometry of the neutral molecule so they do not limit to the lowest energy configurations of CH_3^+ in its ^{1}E, ^{3}E and ^{1}A$_1$ states. Therefore to calculate the kinetic energy release predicted by

Table 5.1: Equilibrium geometries of states of the methyl cation from MCSCF calculations. For the E states, the lower of the components from Jahn-Teller splitting is given.
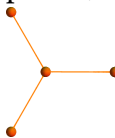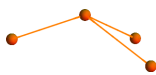
State	Geometry & Symmetry	Angles	Bond Distances (Å)
$^1A_1$	planar, D_{3h}	$\angle$ HCH = 120°	R_{CH} = 1.095
^3E	Jahn-Teller, C_s	$\angle$ H′CH″ = 123.0° $\angle$ H″CH″ = 61.0°	$R_{CH'}$ = 1.092 $R_{CH''}$ = 1.193
^1E	Jahn-Teller, C_s	$\angle$ H′CH″ = 131.7° $\angle$ H″CH″ = 76.0°	$R_{CH'}$ = 1.090 $R_{CH''}$ = 1.204

Table 5.2: Kinetic energy release values from MCSCF calculations: Energy(^1E of CH_4^{++} in T_d symmetry) - Energy(CH_3^+ optimized geometries in Table 5.1)

State	KER from ^1E of CH_4^{++} (eV)
$^1A_1$	11.25
^3E	7.31
^1E	6.08

this level of theory we require the energies of those minimum energy geometries. We therefore optimized the geometries of these states of the methyl cation as described in Appendix B.2 at the same level of MCSCF calculations (same active space) and in the same basis set used for the calculations on the dication, CH_4^{++}. Since both systems, CH_3^+ and CH_4^{++} have the same number of electrons, those calculations are therefore as nearly consistent with the ones producing the curves in Figure 5.4 as is possible at the MCSCF level.

The ^1E and ^3E states are distorted by the Jahn-Teller effect, and the ground $^1A_1$ state of the methyl cation is planar. The optimized geometries are given in Table 5.1. These states were also calculated by Flammini et al.[54], but the geometries they found at an apparently different level of MCSCF were somewhat different. However that work did show that the asymptotic energies of

these states compared with the energies of the corresponding states of CH_4^{++} in T$_d$ symmetry suggested that there must be an intersection between the ^{1}E and ^{1}A$_1$ states which is the one visible in Figure 5.4.

The resulting values of the kinetic energy release for a dissociation beginning on the ^{1}E state of the dication are given in Table 5.1. The energies of these states are lowered considerably by distortion into their optimum geometries. Those asymptotes are the ones that define our best estimate of the kinetic energy release from these calculations, and the resulting KER values are summarized in Table 5.2.

These KER values are consistent with the experimental observations in Figure 5.1 if we identify the two processes contributing to this dissociation channel as

1. ^{1}E of CH$_4^{++}$ in T$_d$ symmetry $\rightarrow$ conical intersection $\rightarrow$ the ^{1}A$_1$ ground state of CH$_3^+$, with a maximum kinetic energy release of $\approx$ 11 eV.

2. ^{1}E of CH$_4^{++}$ in T$_d$ symmetry $\rightarrow$ directly to the lower component of the Jahn-Teller distorted state ^{1}E of CH$_3^+$, with maximum kinetic energy release of $\approx$ 6 eV .

The KER curve shown in Figure 5.1 shows a peak at about 6 eV tailing off to lower KER, and these calculations identify that part of the spectrum with the ^{1}E state of the CH_3^+ fragment . The higher energy part of that KER spectrum can be identified with dissociation to the ground state of CH_3^+. Because that state is planar, far from the geometry of the CH_3 portion of methane in its initial tetrahedral geometry, it can be expected that the ^{1}A$_1$ state of CH_3^+ is produced with high vibrational excitation, particularly in the out-of-plane bending modes.

The difference in the apparent MFPADs measured using the high and low KER portions of the spectrum separately is further evidence of the presence of two distinct dissociation pathways. Comparison with the theoretically calculated MFPAD, averaged over orientations of the CH_3 fragment around the dissociating CH bond direction, indicate that dissociation with high KER

satisfies the axial recoil condition, while dissociation with lower KER in the 6 eV peak does not. That comparison is definitive, because the same amplitudes appearing in Equations (B.1) and (B.3) that produce nearly perfect agreement between observed and calculated MFPADs from other channels are the ones that produce these MFPADs averaged over CH_3 orientations.

While we can confidently assign the two regions of KER in Figure 5.1 to these two mechanisms, we have not explored the complete 9-dimensional potential surfaces of the states involved to understand exactly why the dynamics of dissociation on the ^{1}E surface involves either significant distortion of the molecule away from the direct dissociation path, or even more complicated and longer lived dynamics. We can only say that calculated barrier to dissociation for that state in Figure 5.1 is only 0.45 eV starting from the equilibrium geometry of methane. Thus if Auger decay places the system wave packet at a range of different bond distances at least some of the initial wave packet for dissociation it might be effectively below it. However, the path through the conical intersection to the ^{1}A$_1$ state is calculated with considerable confidence to be steeply downhill to ground state products.

5.2 Conclusion

We have demonstrated the usefulness of molecular frame photoelectron angular distributions from a polyatomic molecule. Complex Kohn calculations of these MFPADs are consistent with experimental data for those cases where the bond axes coincide with the measured ion fragment momenta. Using MFPADs and RFPADs as a foundation, we can explore the dynamics of systems where this is not the case, furthering our understanding of this complicated dissociation processes. Ultimately we anticipate that such calculations and measurements will become a valuable general tool for studying questions such as core-localization dynamics in larger symmetric molecules or the time-dependent measurements of conformation changes using attosecond pulses from next generation light sources.

Appendix A

Multimedia

This appendix contains the MFPADs presented in Chapter 4 in a multimedia fashion. Fig. A.1 contains a movie of the MFPAD integrated over all polarization angles, which was shown in Fig. 4.6. Fig. A.2 contains the same MFPAD in an interactive format. To be able to view either, the document will need to be viewed with Adobe Reader (at least at the time of writing).
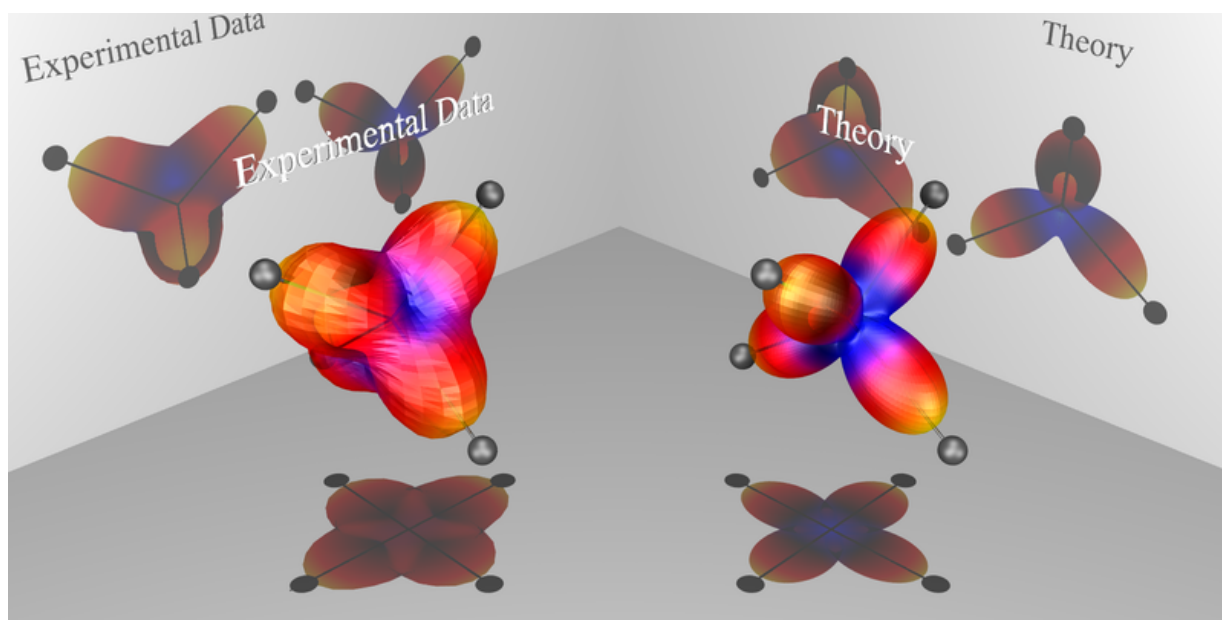
Figure A.1: MFPAD Theory and experiment comparison movie. At the time of writing Adobe Reader is needed to view this content.
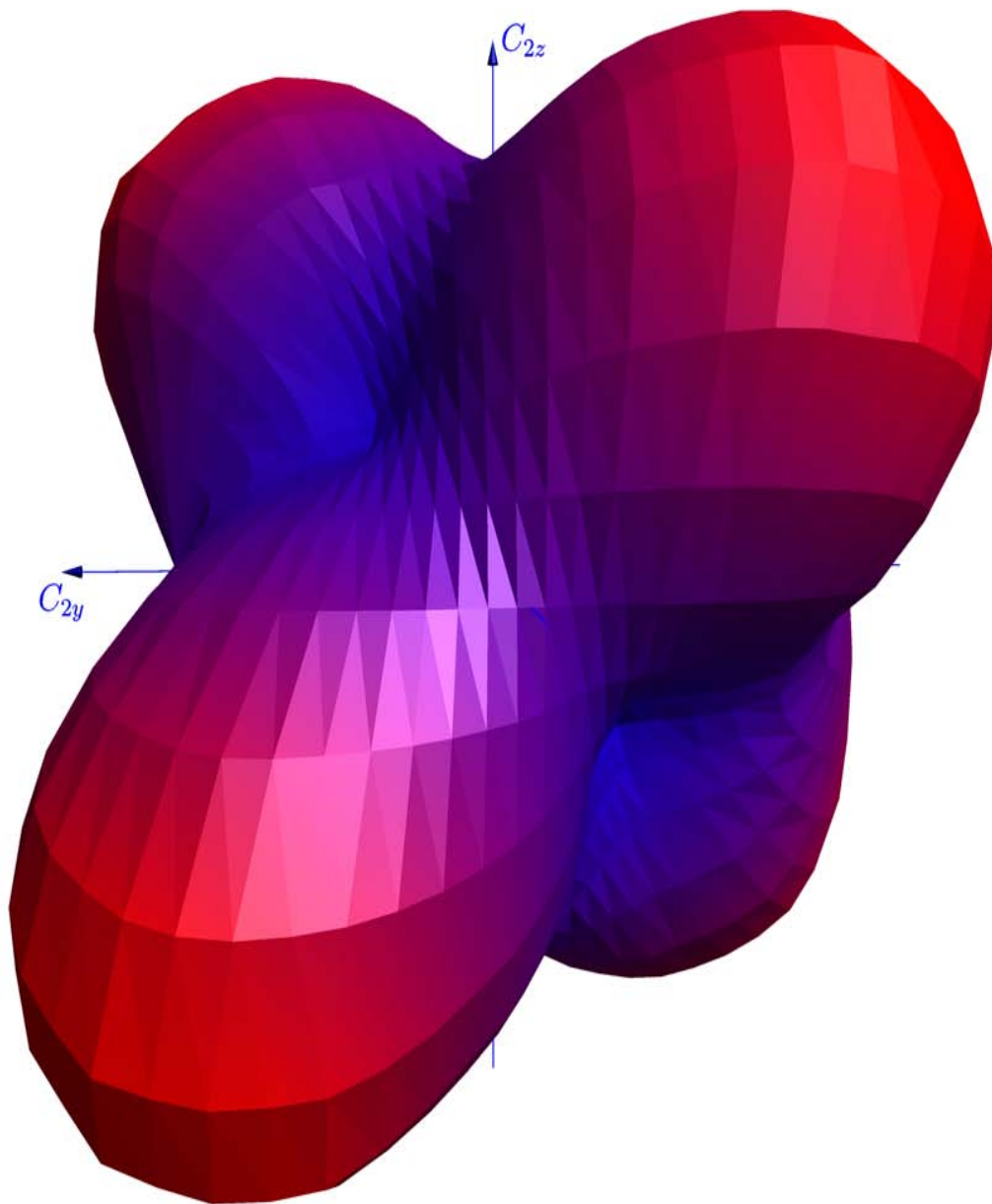
Figure A.2: Interactive 3D MFPAD. At the time of writing Adobe Reader is the only viewer known to support this content.

Appendix B

Theoretical Support

The results from this experiment would have been a mere shadow of what is found here if not for the guidance we received from C.W. McCurdy, C. Trevisan and T. Rescigno. Their help went far beyond performing calculations, which is no small task in an of itself. They provided help with data analysis, which was the foundation of the results presented in Chapter 5. They also provided many of the physical interpretations presented there. The following sections are excerpts from two papers we published together, which explain complex Kohn variational calculations of MFPADs, and Multi-Configuration Self Consistent Field (MCSCF) calculations.

B.1   Complex Kohn Variational Calculations of MFPADs

The calculation of MFPADs for core hole ionization requires a description of both the initial neutral electronic state of the molecule and the electron-ion scattering wave function for an electron scattering from the core-hole cationic state of the molecule. The well established complex Kohn variational method for electron-molecule scattering can be applied to electron scattering from molecular ions (including coupling between electronic states of the ion) and can thereby provide the final state wave function for such a calculation. The application of the complex Kohn method to photoionization has been described in some detail previously[58,59,60], and so we omit those details here.

The MFPAD for a fixed direction of the polarization vector is defined by the dipole matrix element in the equation,

$$\frac{d^2\sigma^{\Gamma_0}}{d\Omega_{\hat{k}}d\Omega_{\hat{\epsilon}}} = \frac{8\pi\omega}{3c}\left|\hat{\epsilon}\cdot\left\langle\Psi_0|\hat{\mu}|\Psi^-_{\Gamma_0,\vec{k}_{\Gamma_0}}\right\rangle\right|^2 \tag{B.1}$$

which defines the cross section for polarization $\hat{\epsilon}$ and ejected electron momentum $\vec{k}_{\Gamma_0}$ leaving the ion in state Γ_0. The target wave function for the electron-ion calculation is constructed as a single configuration using the natural orbitals from the averaged density matrices of the ion and neutral molecules, effectively applying what is known as "Slater's transition state approximation"[67] for the photoionization process. The neutral initial state wave function, Ψ_0, is constructed as a single configuration from those natural orbitals. The complex Kohn scattering calculation then employs the static-exchange approximation with the target cation wave function constructed as a single configuration of the same natural orbitals, and completes the calculation of the final state $\Psi^-_{\Gamma_0,\vec{k}_{\Gamma_0}}$.

In this study we also measure and calculate the MFPAD in Equation (B.1) integrated over polarization directions but with the molecule still in a fixed orientation. It is instructive to note the difference between the information contained in the two kinds of measurements, with $\hat{\epsilon}$ fixed or averaged over its orientations.

In terms of the cartesian components of the dipole operator we can write

$$I_{\vec{k}_{\Gamma_0}\hat{\epsilon}} = \hat{\epsilon}\cdot\left\langle\Psi_0|\hat{\mu}|\Psi^-_{\Gamma_0,\vec{k}_{\Gamma_0}}\right\rangle = \hat{\epsilon}\cdot\vec{M}_{\vec{k}_{\Gamma_0}} \tag{B.2}$$

Integration over the directions of $\hat{\epsilon}$ then gives

$$\int\frac{d^2\sigma^{\Gamma_0}}{d\Omega_{\hat{k}}d\Omega_{\hat{\epsilon}}}d\Omega_{\hat{\epsilon}} = \frac{8\pi\omega}{3c}\frac{4\pi}{3}\left(|M^x_{\vec{k}_{\Gamma_0}}|^2 + |M^y_{\vec{k}_{\Gamma_0}}|^2 + |M^z_{\vec{k}_{\Gamma_0}}|^2\right) \tag{B.3}$$

and we see that while the three components of the transition dipole amplitude are combined coherently in Equation (B.1) to produce a wide variety of shapes of the MFPAD for different

94

polarization directions, the experiment that measures the MFPAD averaged over polarization directions measures an incoherent sum of the same three amplitudes.

In these studies we also calculated MFPADs averaged around one of the C_3 axes of the CH_4 molecule but with the polarization vector fixed at particular angles to that axis. These averages were accomplished by performing separate calculations of the MFPAD on grids of directions of electron directions $\hat{k}$ for a set of orientations of the molecule and using Shepard interpolation[68] to evaluate the average.

B.2   MCSCF Calculations

The MCSCF calculations we report here were performed with the COLUMBUS 7.0 quantum chemistry code[69]. All the calculations we report were performed with the cc-pvtz (correlation consistent plus polarization triple zeta) basis sets for carbon and hydrogen. Complete active space (CAS) state-averaged MCSCF calculations were performed for the dissociative curves of C_4^{++} shown in Fig 5.4 that included all five components of the $^1A_1$, ^1E, and ^3E states. The $1a_1$ ($\approx$ C 1s) orbital was held doubly occupied and the remaining six electrons were distributed in a CAS space of 10 orbitals, giving a total of 2688 configurations in those calculations, which were performed in C_s symmetry so that the CAS space contained 7 a' and 3 a" molecular orbitals. The geometry of the CH_3 fragment was fixed in the tetrahedral geometry of methane with a CH bond distance of 2.05 bohr.

The other curves in that figure (in particular the black dashed curves that are not dissociative) are from similar state-averaged MCSCF calculations, but using the all 9 components of the $^3T_1$, ^1E, $^1T_2$, and $^1A_1$ states which split as indicated in C_{3v} symmetry.

Geometry optimizations for the states of CH_3^+ were performed using the same CAS space of 10 orbitals as follows: The energy of the $^1A_1$ state was minimized in an MCSCF with a single state

using no symmetry, so that there were 4950 configurations in those calculations. The ^{3}E state geometry was optimized in state-averaged MCSCF calculations that included both Jahn Teller components with 6930 configurations made from the same CAS space. The ^1E state is not the lowest singlet state, and so its geometry was optimized in state-averaged MCSCF calculations that included the lowest two singlets with 4950 configurations.

Appendix C

Normal Modes of Methane

These normal modes where calculated by C.W. McCurdy using the COLUMBUS 7.∅ quantum chemistry code[69]. There are nine normal modes and this section attempts to give the reader an understanding of the zero point vibration. In the following pages each normal mode is plotted independently . The top table gives a quantitative representation of the normal mode. The top row plots the radial position of the carbon (left) and the four hydrogen atoms (right). The second row plots θ and ϕ in degrees for all atoms. All of the atoms are always plotted, but they are not always visible because their markers may lie on top of one another.

The bottom table attempts to show the actual movement of each hydrogen atom in the molecule as a function of time. This is difficult to show in a static picture, so the time has been encoded by changing the color of the sphere that represents the hydrogen atoms. On the non-diagonal panels, the camera is located on a C_2 axis. The camera position is always the sum of the vector position of two hydrogens. The particular two vectors used in each panel can be determined by examining the top and left columns.

Normal Mode 1

Normal Mode 2

Normal Mode 3

Normal Mode 4

Normal Mode 5

Normal Mode 6

Normal Mode 7

Normal Mode 8
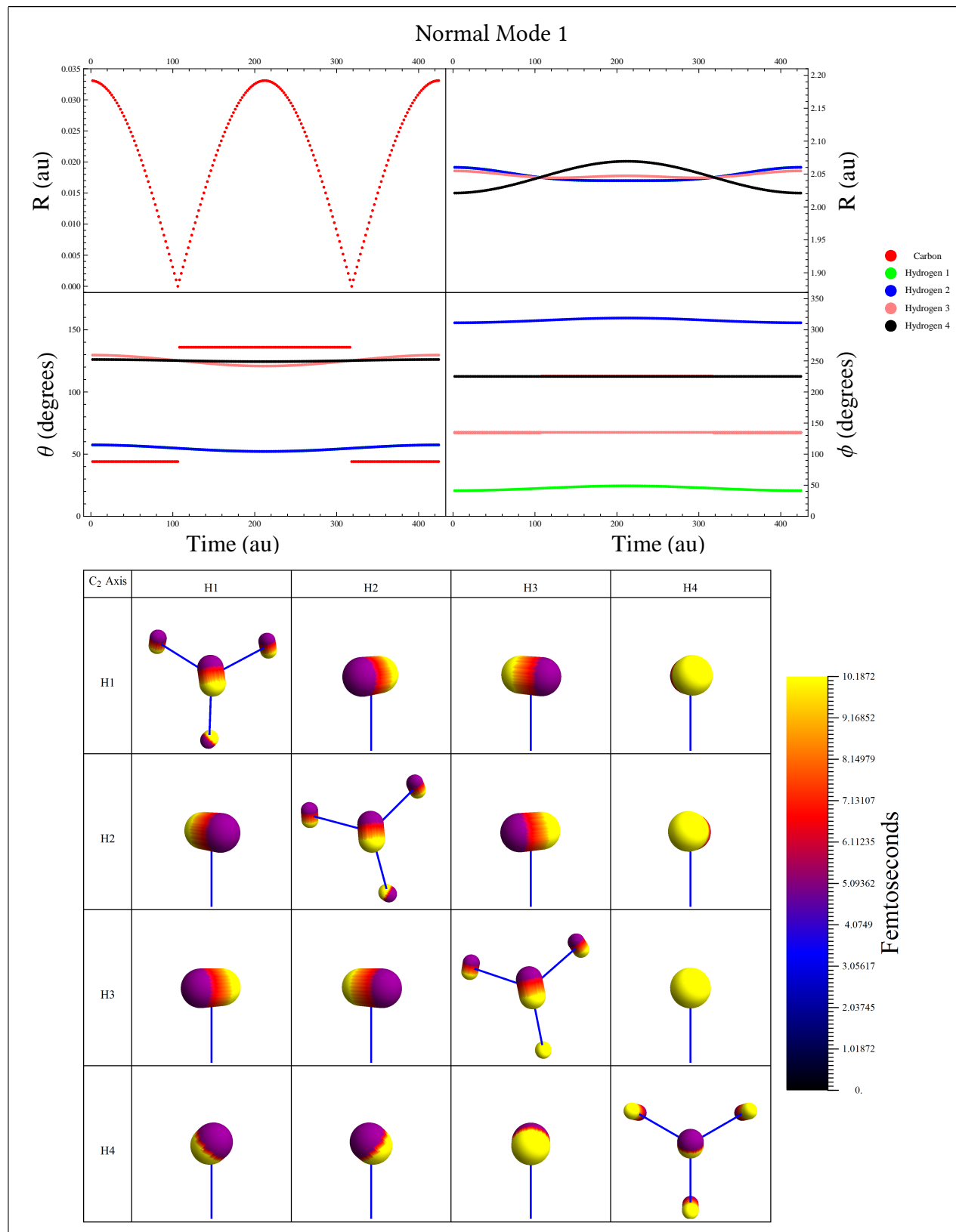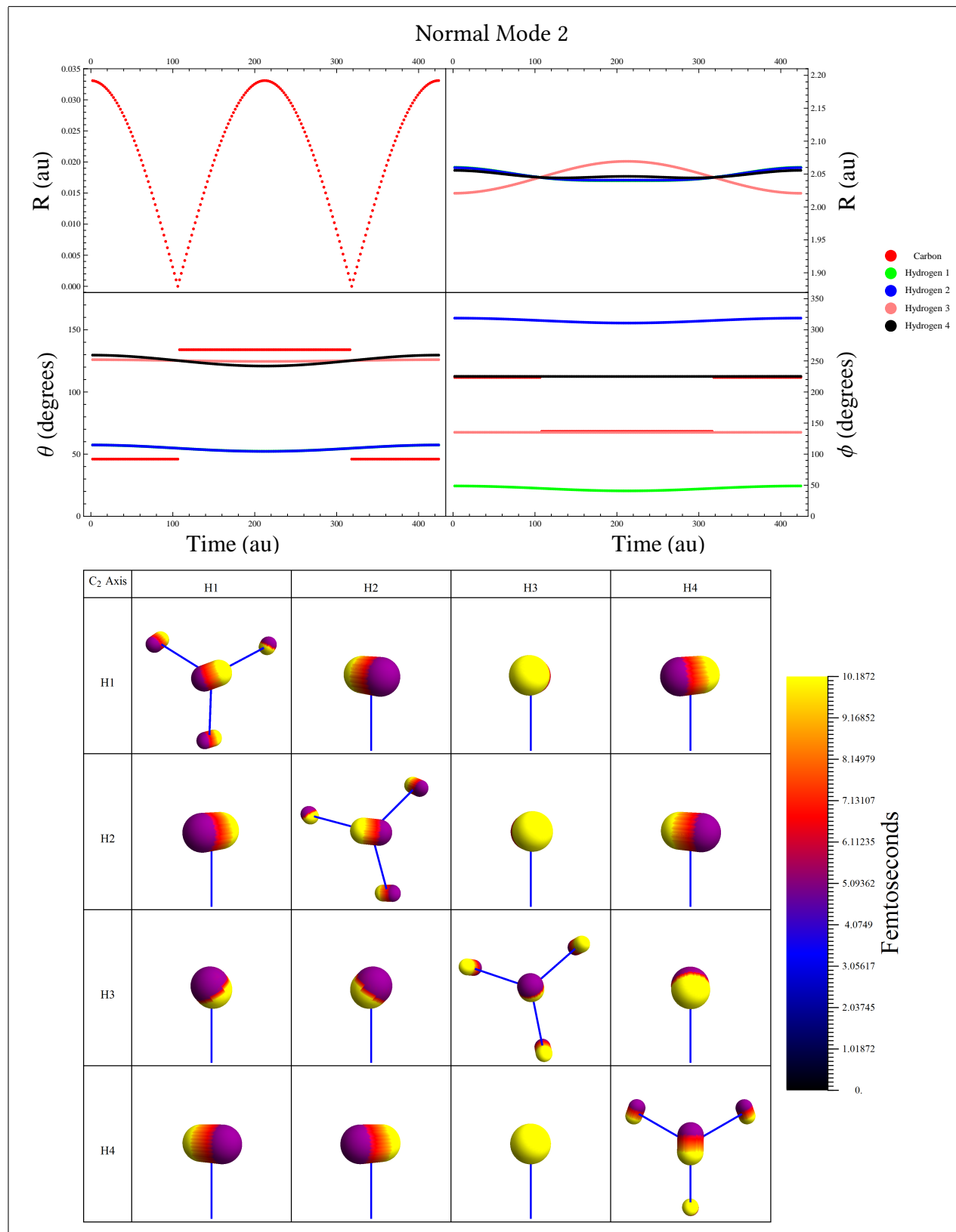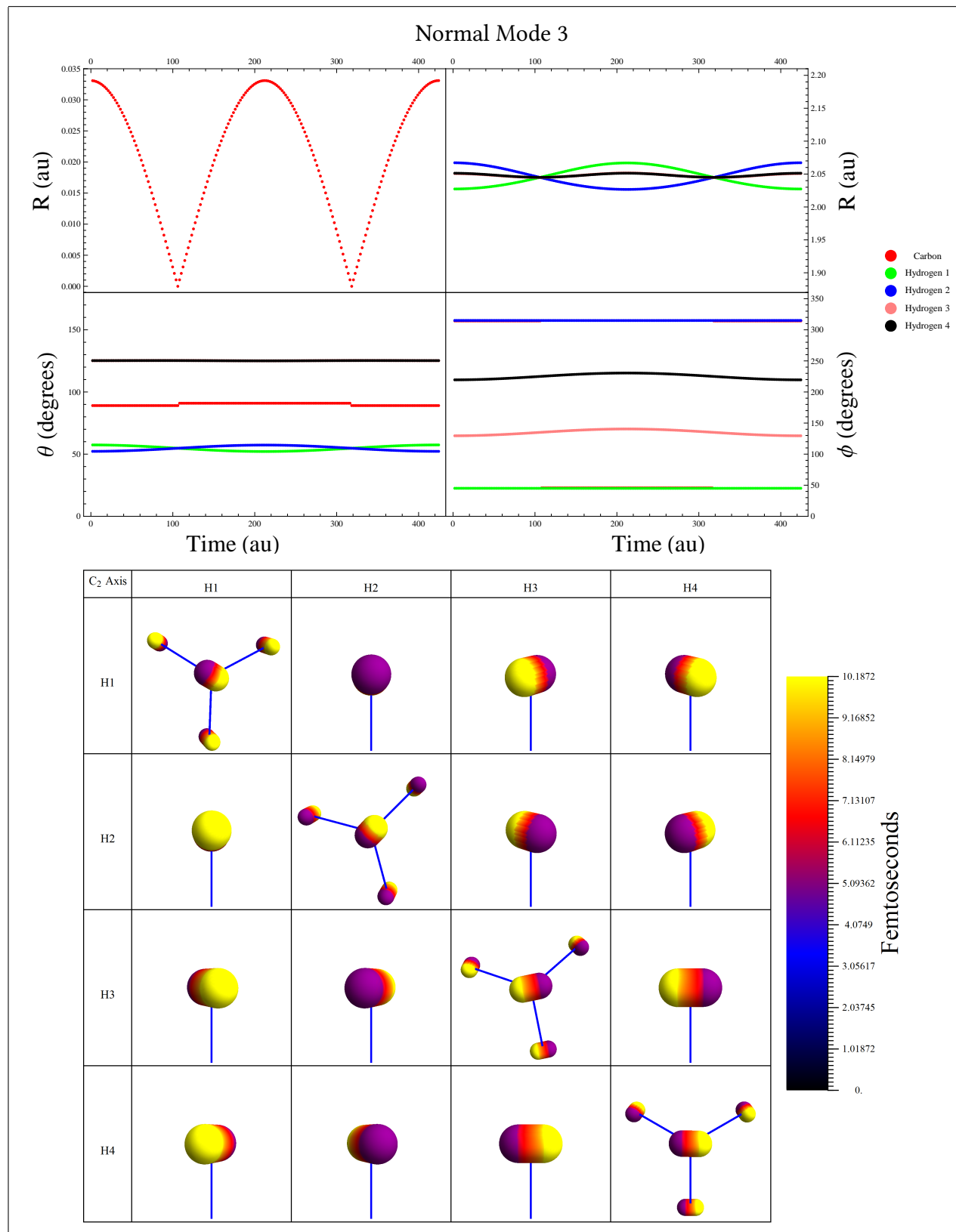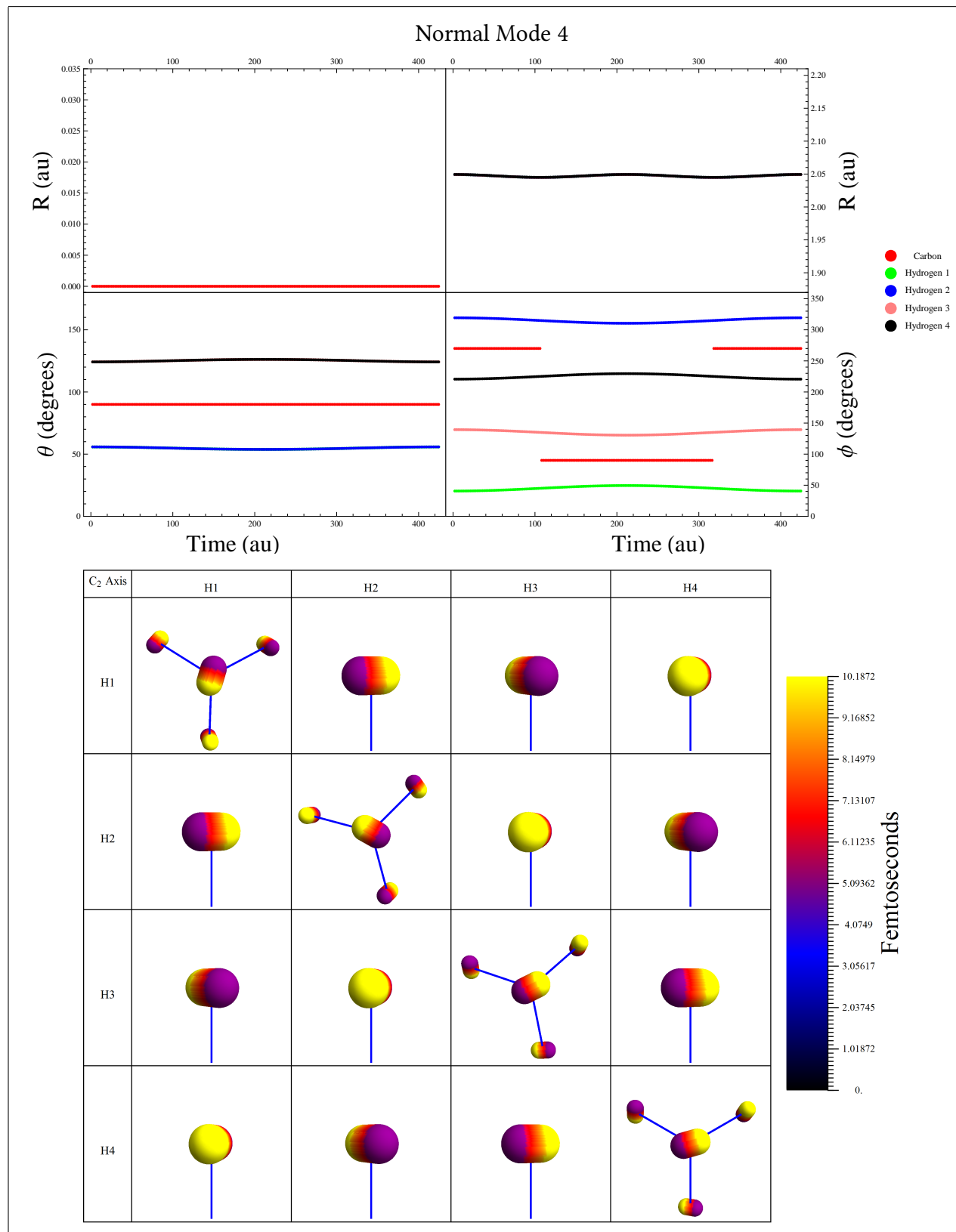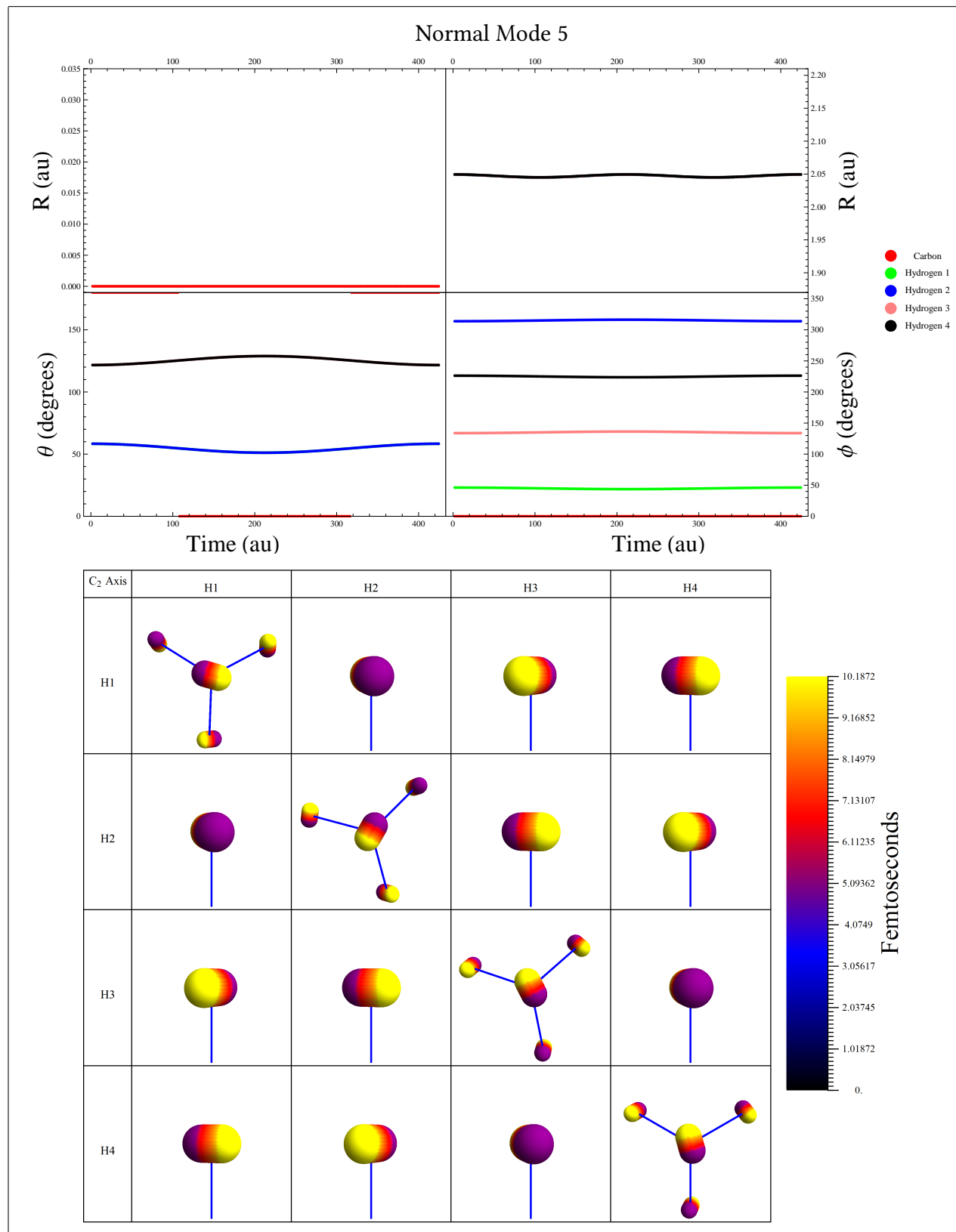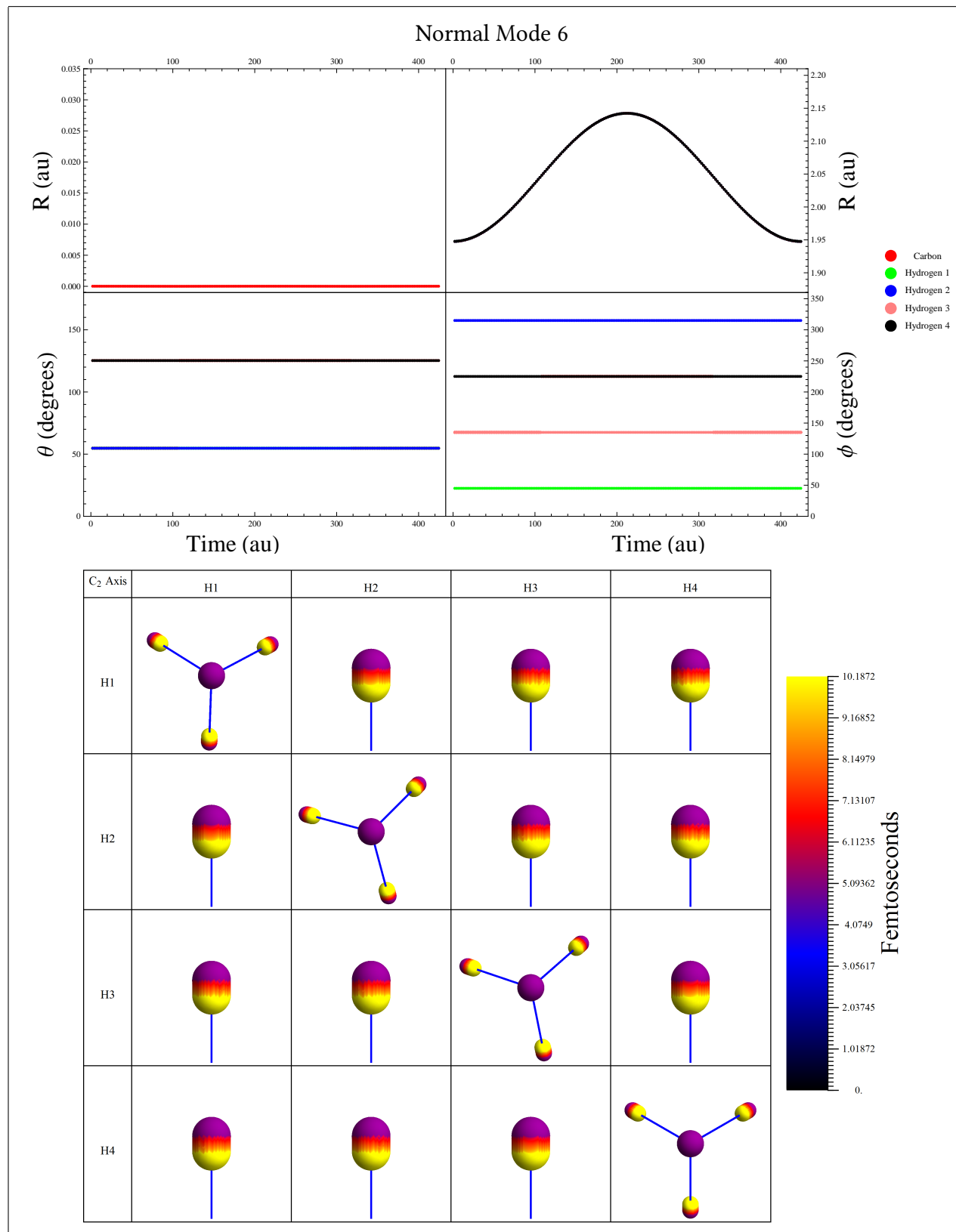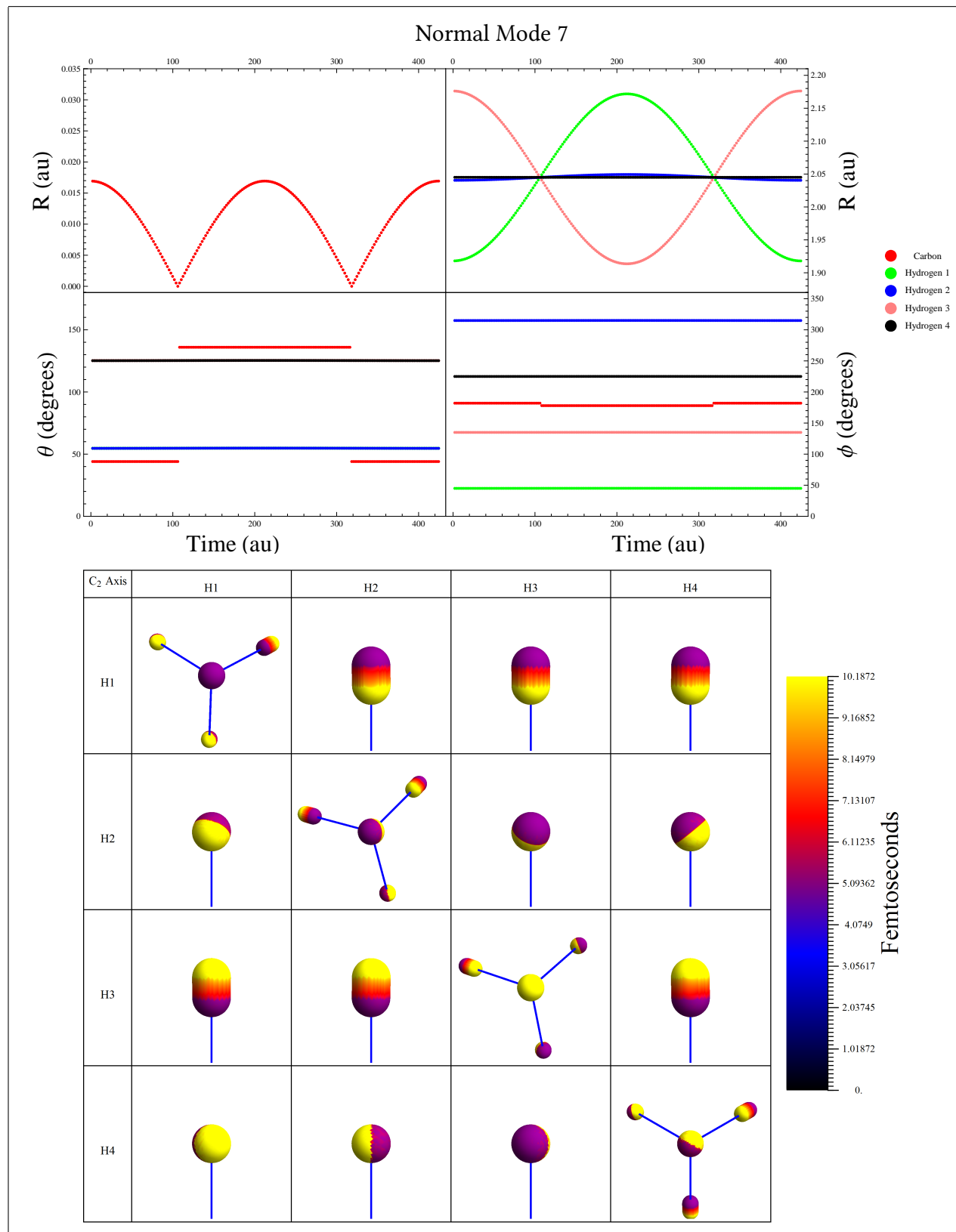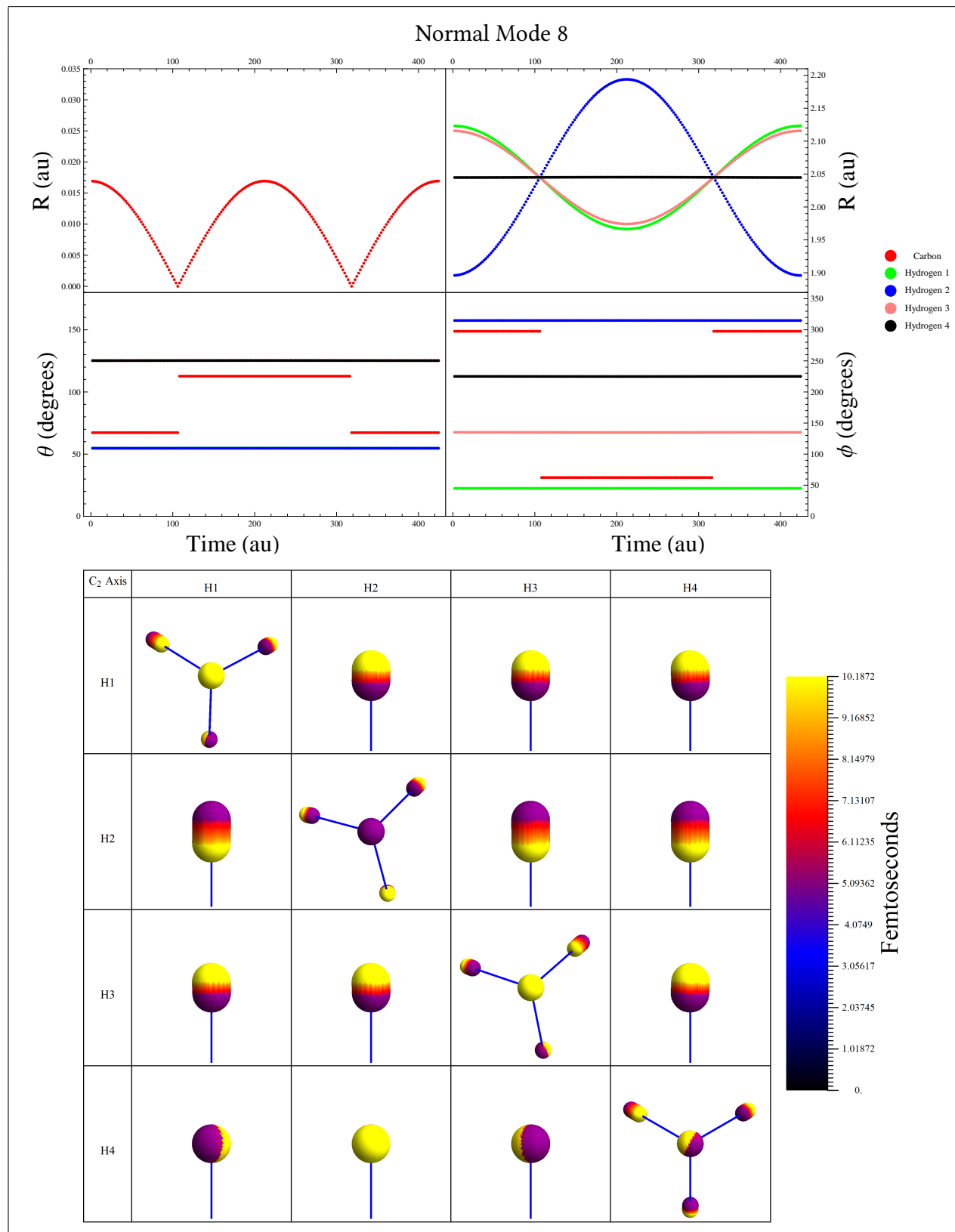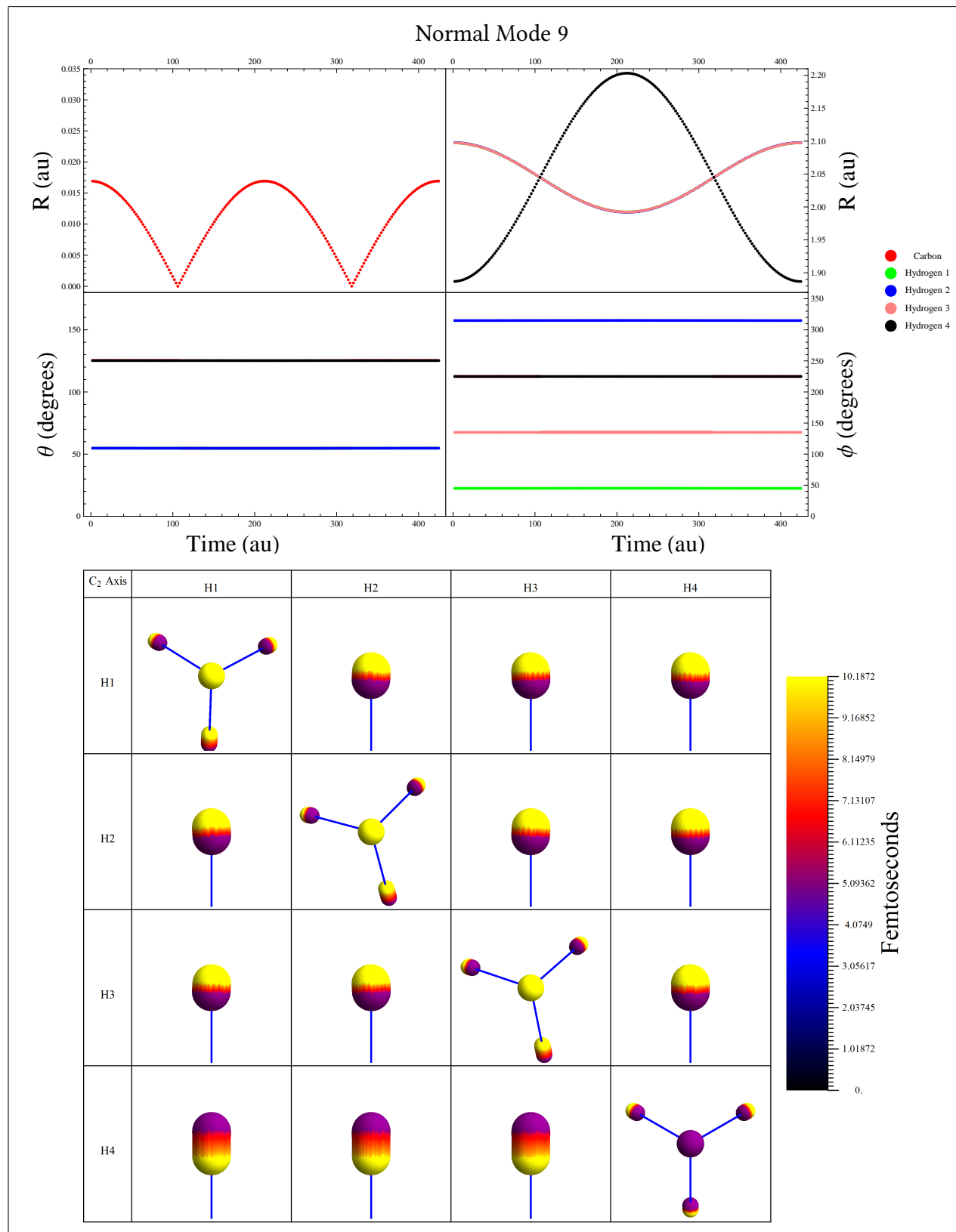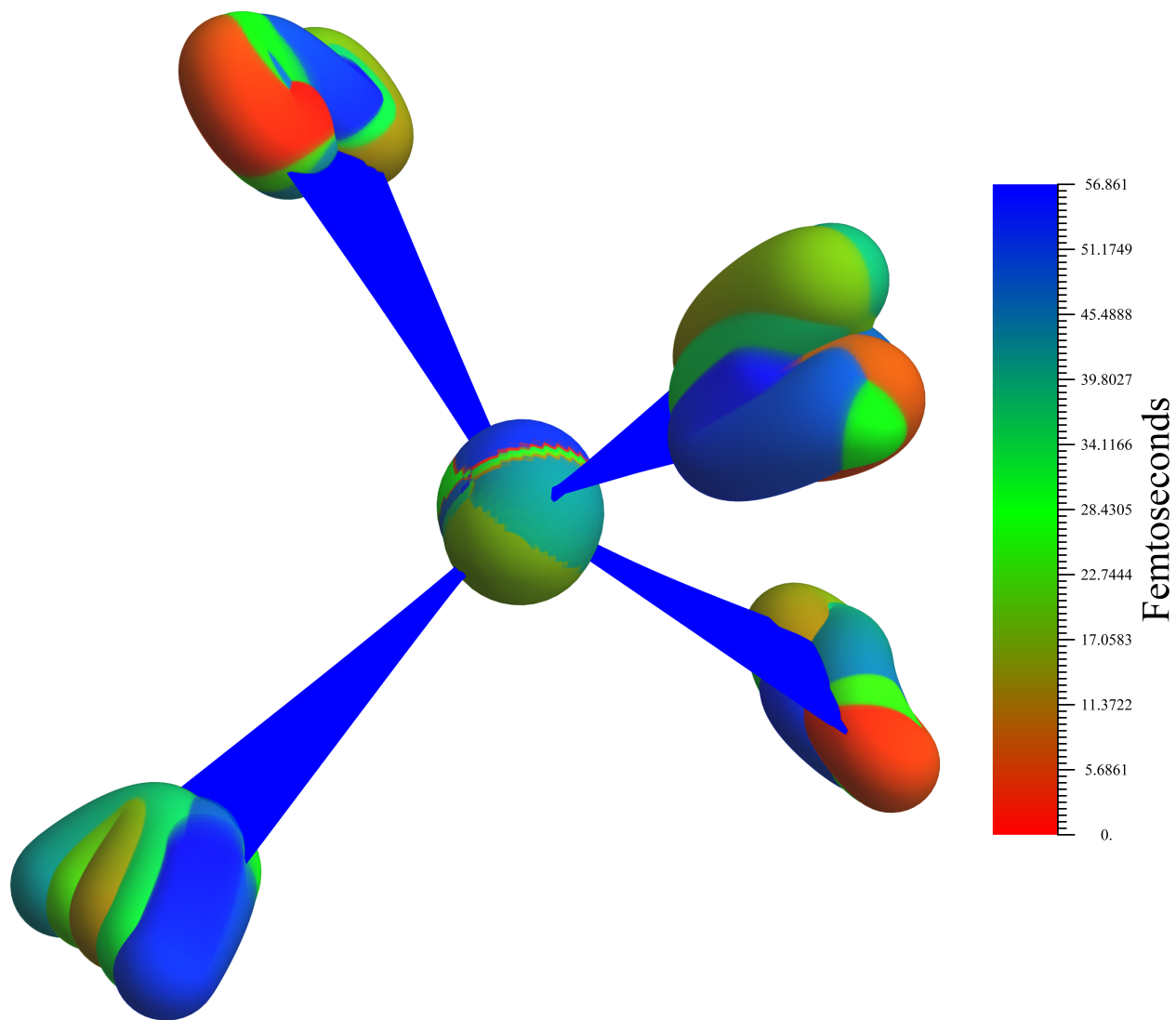
Normal Mode 9

Figure C.1: Zero point motion of all nine normal modes of methane.

Appendix D

Time to Momentum: Three Acceleration Regions

```c
// **************************************************************
// **
// ** momentum calculation for time of flight direction for 3
// ** accel. regions of any size.  This function uses newton's
// ** method to solve the problem.  Returns P in Au.
// **
// ** By Joshua Williams
// **************************************************************
double tof2mom_3accel(double tof_ns, double acc1mm, double acc2mm, double
    acc3mm, double Efield1_Vpcm, double Efield2_Vpcm, double Efield3_Vpcm,
    double charge_au, double mass_amu){

  if (tof_ns > 0.1){ //don't try to find P if the time of flight is negative

    int i;

    //convert to SI units
    double t = tof_ns * 1e-9;

    double mass = mass_amu *  1.660538782e-27;
    double q = charge_au * 1.602176487e-19;
    double Psi_to_Pau = 1 / 1.992851565e-24;

    double acc1m = acc1mm * .001;
    double acc2m = acc2mm * .001;
    double acc3m = acc3mm * .001;
    double Efield1_Vpm = Efield1_Vpcm * 100.0;
    double Efield2_Vpm = Efield2_Vpcm * 100.0;
    double Efield3_Vpm = Efield3_Vpcm * 100.0;

    //find accel. for each region
    double acc1 = (Efield1_Vpm * q)/ mass;
    double acc2 = (Efield2_Vpm * q)/ mass;
    double acc3 = (Efield3_Vpm * q)/ mass;

    double  acc2_zero_bool = 0.;
    double  acc3_zero_bool = 0.;

    double v =10000000.0;
    double t_function = 0.;
    double Dt_function_dv = 0.;
```

108

```
double new_v = 100000000.;

double a2_term = 0.0;
double a3_term = 0.0;
double v1 = 0.0;

//int limit = 10;

for( i =0; i < 25; i ++){
   // Newton's method x1 = x0 - f(x0)/f'(x0)
   /*
   t_function =  -t + (-v + sqrt (2.0* acc1 * acc1m + v*v))/ acc1 +
           ( (-sqrt (2.0* acc1 * acc1m + v*v) + sqrt (2.0* acc1 * acc1m +
              2.0* acc2 * acc2m + v*v))/ acc2 )+
           (( (-sqrt (2.0* acc1 * acc1m + 2.0* acc2 * acc2m + v*v) +
               sqrt (2.0* acc1 * acc1m + 2.0* acc2 * acc2m + 2.0* acc3 * acc3m +
               v*v))/ acc3 );

   Dt_function_dv =   (-1.0 + v/ sqrt (2.0* acc1 * acc1m + v*v))/ acc1 +
           ( (v*(-(1.0/ sqrt (2.0* acc1 * acc1m + v*v)) +
               1.0/ sqrt (2.0* acc1 * acc1m + 2.0* acc2 * acc2m + v*v)))/ acc2 )+
           ( (v*(-(1.0/ sqrt (2.0* acc1 * acc1m + 2.0* acc2 * acc2m + v*v)) +
               1.0/ sqrt (2.0* acc1 * acc1m + 2.0* acc2 * acc2m + 2.0* acc3 * acc3m
               + v*v)))/ acc3 );
   */

   //Need to figure out which case we have and how each term reduces

   if (acc2 != 0. &&  acc2m != 0.){
     a2_term = (- sqrt (2.0* acc1 * acc1m + v*v) + sqrt (2.0* acc1 * acc1m +
        2.0* acc2 * acc2m + v*v))/ acc2;
   }
   else if (acc2m != 0. && acc2 == 0.){
     a2_term = acc2m/ sqrt (2.* acc1 * acc1m + v*v);
   }
   else{
     a2_term = 0.0;
   }
   if (acc3 != 0. &&  acc3m != 0.){
     a3_term = (- sqrt (2.0* acc1 * acc1m + 2.0* acc2 * acc2m + v*v) +
        sqrt (2.0* acc1 * acc1m + 2.0* acc2 * acc2m + 2.0* acc3 * acc3m +
        v*v))/ acc3;
   }
   else if (acc3m != 0. && acc3 == 0.) {
     a3_term = acc3m/ sqrt (2.* acc1 * acc1m + 2.* acc2 * acc2m + v*v);
   }
   else{
     a3_term = 0.0;
   }

   t_function =   -t + (-v + sqrt (2.0* acc1 * acc1m + v*v))/ acc1 + a2_term +
       a3_term;

   v1 = v *(1.01);
```

```c
      if ( acc2 != 0. &&  acc2m != 0.){
        a2_term = (−sqrt(2.0*acc1*acc1m + v1*v1) + sqrt(2.0*acc1*acc1m +
            2.0*acc2*acc2m + v1*v1))/acc2;
      }
      else if (acc2m != 0. && acc2 == 0.){
        a2_term =acc2m/sqrt(2.*acc1*acc1m + v1*v1);
      }
      else{
        a2_term = 0.0;
      }

      if (acc3 != 0. &&  acc3m != 0.){
        a3_term = (−sqrt(2.0*acc1*acc1m + 2.0*acc2*acc2m + v1*v1) +
            sqrt(2.0*acc1*acc1m + 2.0*acc2*acc2m + 2.0*acc3*acc3m +
            v1*v1))/acc3;
      }
      else if (acc3m != 0. && acc3 == 0.) {
        a3_term = acc3m/sqrt(2.*acc1*acc1m + 2.*acc2*acc2m + v1*v1);
      }
      else{
        a3_term = 0.0;
      }

      Dt_function_dv =( (−t + (−v1 + sqrt(2.0*acc1*acc1m + v1*v1))/acc1 +
          a2_term + a3_term) − t_function )/ (v1 − v);


      new_v = v −  t_function / Dt_function_dv;


      if ( fabs((new_v * mass * Psi_to_Pau − v * mass * Psi_to_Pau)/ (v *
          mass * Psi_to_Pau)) < 1e−3) {
        /*printf("i=%i\n", i);*/
        i = 500;
      }
      v = new_v;
    }

    return (v * mass * Psi_to_Pau );

    }

  else{
    return −100000.;
  }
}
```

Appendix E

Three Dimensional Momentum Sort

E.1 Overview

The [H^+ ,CH_3^+] fragmentation pathway presented the difficult challenge of separating it form the adjacent [H^+ ,CH_2^+ ,H^+] channel. The [H^+ ,CH_3^+] fragmentation pathway is one of the curves visible in Figure E.1, but it is not isolated from the surrounding channels. The [H^+ ,CH_3^+] channel is located between 500 and 1500 ns on the recoil 1 TOF axis and 3300 and 4500 ns on the recoil 2 TOF axis and is visible as a bright curve located on the top of the stack.

(a) PIPICO Spectrum

(b) Enlarged PIPICO Spectrum
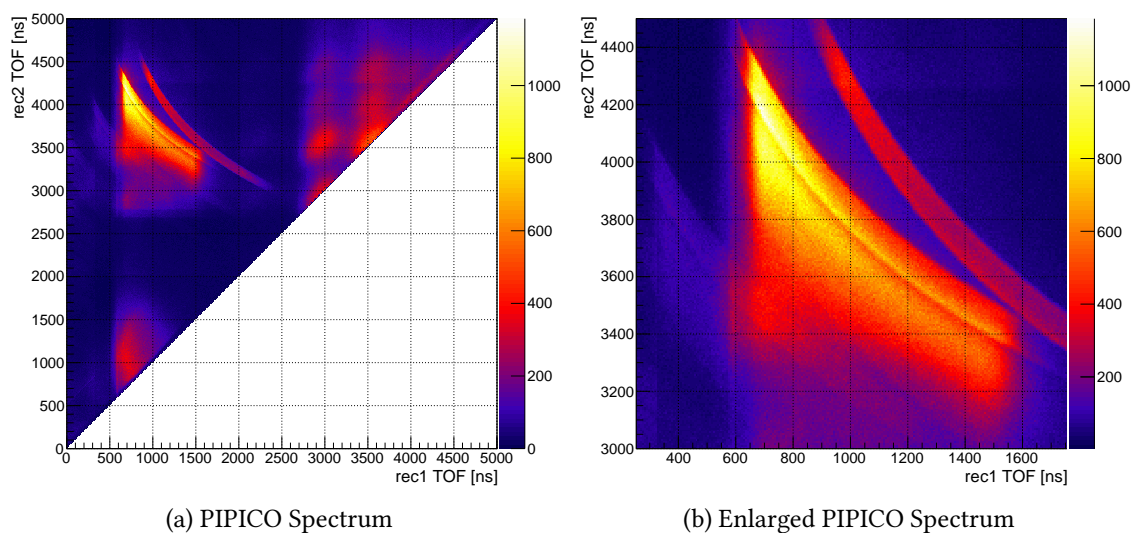
Figure E.1: Raw PIPICO Spectrum.

To overcome this challenge a momentum sort routine was written. This routine is called for every event[a] in the dataset. It then calculates the momentum of both particles. It is given

---

[a] Actually it is only called when there is at least two recoils and one electron in the event.

a test mass, which in this case is 1 and 15 amu, along with the electric field and lengths of the spectrometer. Most of the particle pairs in the dataset are not actually be H^+ and CH_3^+ and therefore this routine calculated the momentum incorrectly. The actual H^+ and CH_3^+ events conserve momentum and were then marked by the routine as belonging to the $[H^+, CH_3^+]$ fragmentation pathway.

(a) Momentum in the TOF direction of the first recoil verse the second recoil

(b) X Momentum (photon propagation)

(c) Y Momentum (jet direction)
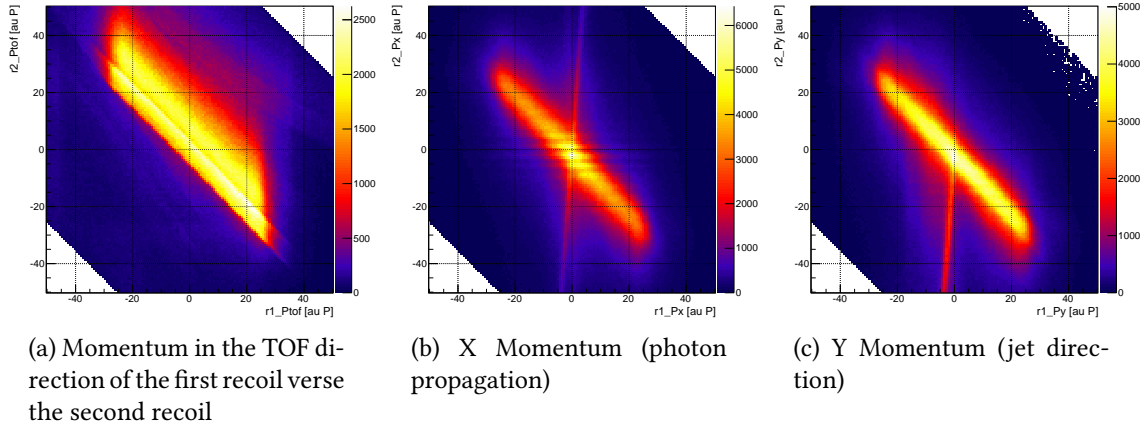
Figure E.2: Momentum conservation spectra with a wide gate.

Momentum conservation can be seen in Figure E.2 as a diagonal line. The momentum sort routine also takes as input the width of the allowed deviation from absolute conservation. In Figure E.2 the gate in the TOF direction is set to be not more that 75au. That means the sum of the two recoils momentum in TOF direction must be less the ±75au. This is a very large gate and it is clear that many other channels are also included. But this is an important step, because it lets you verify that the detector position offsets and electric field are approximately correct. Once the input parameters are correct the gates can be narrowed to filter out the other channels. This can be seen in Figure E.3, where the momentum gate in the TOF direction is 4au wide and the momentum gate in the X and Y directions are 11au wide. Most of the artifacts in the initial plots are no longer visible when the gate is tightened.

(a) Momentum in the TOF direction of the first recoil verse the second recoil

(b) X Momentum (photon propagation)

(c) Y Momentum (jet direction)
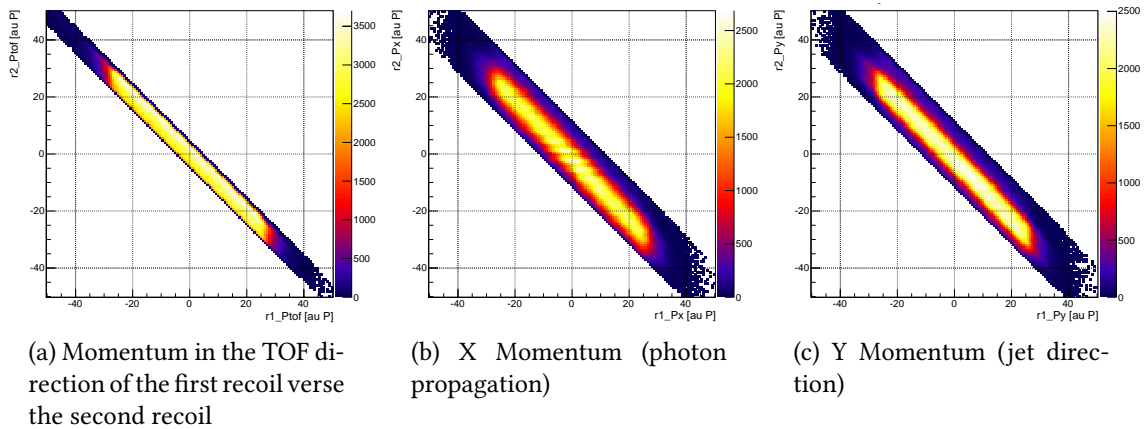
Figure E.3: Momentum conservation spectra with a narrow gate.

E.2   Source Code

```
//  ************************************************************
//  ** This is a sorting routine that checks to see if the momentum of a
     particle pair is conserved.
//  **    The data is returned via two arrays (recoils[10][10] and
     electrons[10][10]) that have to be passed into the function.
//  **    These arrays should be empty when it is passed (all values set to
     -99999 or something like that).
//  ** This function will return 0 if momentum is not conserved and 1 if it is.
//  **
//  **
//  ** Format of the returned data. The arrays should be 10x10 and they should
     be initialized to some nonzero (large) value.
//  **   recoils[recoil#][0]  = tof ns
//  **   recoils[recoil#][1]  = x
//  **     recoils[recoil#][2]  = y
//  **     recoils[recoil#][3]  = Ueber.rec.method[k]
//  **   recoils[recoil#][4]  = mass
//  **   recoils[recoil#][5]  = charge
//  **     recoils[recoil#][6]  = recoil_Ptof
//  **     recoils[recoil#][7]  = recoil_Py
//  **   recoils[recoil#][8]  = recoil_Px
//  **
//  **   electrons[electron#][0]  = tof ns
//  **   electrons[electron#][1]  = x
//  **     electrons[electron#][2]  = y
//  **     electrons[electron#][3]  = Ueber.rec.method[k]
//  **   electrons[0][9] = reaction_flag;   \\ this reaction_flag is passed in
     and is a marker for you to be able to identify which mass pair it was
     later.
//  **
```

113

```
// ** electrons[0][9] has .1 added to the reaction_flag number for every
   "good" electron that is found
// **
// **    mass1 is in AMU
// **    charge1 is in a.u.
// **    momentum_halfwidth is in a.u. of momentum and is used in the
   directions that are parallel to the detector
// **    momentum_halfwidth_tof is in a.u. of momentum and is used in the
   direction that is the field direction
// **    el_tof_center is in ns
// **    electron_halfwidth is in ns
// **    reaction_number is a label so that you can mark each reaction
// **    jet_velocity_SI in in meter/sec and will be subtracted from the y
   momentum
// **
// ** Example code to call this function;
// **    // REACTION FLAG 2: CH3+ and H+ with electrons
// **       //—————————————————————————————
// **    if (    (Ueber.rec.number_of_reconstructed_hits >1)
// **        && (Ueber.elec.number_of_reconstructed_hits >0)
// **        && (cnt[bunchmarker_channel]>0)
// **        && (filling < 1)
// **        &&  parameter[500] > 0  )
// **    {
// **        reaction_flag = 2.0; // change this number to indicate which
   reaction this is
// **
// **        mass1 = parameter[501];
// **        mass2 = parameter[502];
// **        charge1 = parameter[503];
// **        charge2 = parameter[504];
// **        momentum_halfwidth_tof = parameter[505];
// **        momentum_halfwidth = parameter[506];
// **
// **        filling = momentum_sort( Ueber, parameter, tdc_ns,
   bunchmarker_channel, recoils, electrons,  mass1,  mass2, charge1,
   charge2,  momentum_halfwidth_tof, momentum_halfwidth, e_tof_center,
   electron_halfwidth , reaction_flag, jet_velocity_SI);
// **    }
// **
// **    By Joshua Williams
// ***************************************************************
int momentum_sort(Ueberstruct &Ueber, double  parameter[], double
   tdc_ns[][NUM_IONS], int bunchmarker_channel,
  double recoils[10][10], double electrons[10][10], double mass1, double
     mass2, double charge1, double charge2,
  double momentum_halfwidth_tof, double momentum_halfwidth, double
     e_tof_center, double electron_halfwidth , double reaction_flag, double
     jet_velocity_SI){

// ** Please note that you will need to add parameters to your config file to
   tell it how long each section of the spectrometer is.
  const double bunchspacing = 328.226;
```

```cpp
    const double R_accel_length = parameter[1200]; // mm
    const double R_accel_length_2 = parameter[1201]; // mm
    const double R_accel_length_3 = 0.0; //parameter[]; // mm

    const double E_field_Vpcm = parameter[1070]; // v/cm
    const double Ion_E_field_Vpcm_2 = parameter[1202]; // v/cm
    const double Ion_E_field_Vpcm_3 = 0.0; //parameter[]; // v/cm
// **


    const double Kg_over_AMU = 1.660538782e-27;
    const double AUmass_over_AMU = 1.660538782e-27/9.10938215e-31;
    const double M_over_CM = 1.0/100.0;
    const double M_over_MM = 1.0/1000.0;
    const double S_over_nS = 1.0/(pow(10.0,9.0));
    const double eV_over_J = 1.0/(1.60217*pow(10.0,-19.0) );
    const double KgMpers_over_Pau = 1.992851565e-24;
    const double MperS_over_auVelocity = 2.1876912633e6;

    int filling = 0;
    int array_length = 10; //this is the lenght of both the electrons[][] and
        recoils[][] arrays

    double recoil_tof_1 = 0;
    double electron_tof_1 = 0;
    double recoil_tof_2 = 0;

    //momentum
    double recoil_Ptof_1 = -1000;
    double recoil_Ptof_2 = -1000;
    double recoil_Ptof_1_reversed = -1000;  //if the mass1 is really mass2 and
        charge1 is really charge2
    double recoil_Ptof_2_reversed = -1000;  //if the mass1 is really mass2 and
        charge1 is really charge2

    double recoil_Py_1 = -1000;
    double recoil_Py_2 = -1000;
    double recoil_Py_1_reversed = -1000;  //if the mass1 is really mass2 and
        charge1 is really charge2
    double recoil_Py_2_reversed = -1000;  //if the mass1 is really mass2 and
        charge1 is really charge2

    double recoil_Px_1 = -1000;
    double recoil_Px_2 = -1000;
    double recoil_Px_1_reversed = -1000;  //if the mass1 is really mass2 and
        charge1 is really charge2
    double recoil_Px_2_reversed = -1000;  //if the mass1 is really mass2 and
        charge1 is really charge2



    for (int i=0;i<(Ueber.rec.number_of_reconstructed_hits-1);i++)
      { // begin for: recoils
        for (int j=0;j<(Ueber.elec.number_of_reconstructed_hits);j++)
```

115

```
{ // begin for: electrons

electron_tof_1 = fmod((Ueber.elec.time[j] −
    tdc_ns[bunchmarker_channel][1] + bunchspacing*1000),bunchspacing);
recoil_tof_1 = (Ueber.rec.time[i]   − Ueber.elec.time[j] +
    electron_tof_1);
recoil_tof_2 = (Ueber.rec.time[i+1] − Ueber.elec.time[j] +
    electron_tof_1);

recoil_Ptof_1 = tof2mom_3accel(recoil_tof_1,  R_accel_length,
    R_accel_length_2,  R_accel_length_3,  E_field_Vpcm,
    Ion_E_field_Vpcm_2,  Ion_E_field_Vpcm_3,  charge1,  mass1); //a.u.
    of momentum
recoil_Ptof_2 = tof2mom_3accel(recoil_tof_2,  R_accel_length,
    R_accel_length_2,  R_accel_length_3,  E_field_Vpcm,
    Ion_E_field_Vpcm_2,  Ion_E_field_Vpcm_3,  charge2,  mass2); //a.u.
    of momentum
recoil_Px_1 = (mass1 * Ueber.rec.x[i]   / recoil_tof_1 ) * Kg_over_AMU
    * (M_over_MM / S_over_nS) * (1/KgMpers_over_Pau); //a.u. of momentum
recoil_Px_2 = (mass2 * Ueber.rec.x[i+1] / recoil_tof_2 ) * Kg_over_AMU
    * (M_over_MM / S_over_nS) * (1/KgMpers_over_Pau); //a.u. of momentum
recoil_Py_1 = (mass1 * Kg_over_AMU ) * (  ((Ueber.rec.y[i]    /
    recoil_tof_1 ) * (M_over_MM / S_over_nS) − jet_velocity_SI) )*
    (1/KgMpers_over_Pau); //a.u. of momentum
recoil_Py_2 = (mass2 * Kg_over_AMU ) * (  ((Ueber.rec.y[i+1]  /
    recoil_tof_2 ) * (M_over_MM / S_over_nS) − jet_velocity_SI) )*
    (1/KgMpers_over_Pau); //a.u. of momentum


//—————————ideal resistor correction

// the detector gets rotated by 180 so I will just make px=−px and
    py=−py

if(mass1 == 1){
  recoil_Ptof_1 = recoil_Ptof_1 + 0.357581;
  recoil_Px_1 = −recoil_Px_1 +0.078977;//pz
  recoil_Py_1 = −recoil_Py_1 +0.156418;

}
if(mass1 == 2){
  recoil_Ptof_1 = recoil_Ptof_1 − 0.758001;
  recoil_Px_1 = −recoil_Px_1 + 0.028448; //pz
  recoil_Py_1 = −recoil_Py_1 + 0.179222;

}

if(mass2 == 14) {
  recoil_Ptof_2 = recoil_Ptof_2 − 1.184648;
  recoil_Px_2 = −recoil_Px_2 − 1.229821;//pz
  recoil_Py_2 = −recoil_Py_2 − 0.475133;
}
if(mass2 == 15) {
  recoil_Ptof_2 = recoil_Ptof_2 − 3.380583;
```

```
  recoil_Px_2  =  −recoil_Px_2   −1.698323;// pz
  recoil_Py_2  =  −recoil_Py_2  −  0.041085;
}

//————————————————————————————————————————————————————


  if (
    filling  ==  0
    &&
    (
      (
        (  fabs ( recoil_Px_1  +  recoil_Px_2 )  <  momentum_halfwidth      )
        &&
        (  fabs ( recoil_Py_1  +  recoil_Py_2 )  <  momentum_halfwidth      )
        &&
        (  fabs ( recoil_Ptof_1  +  recoil_Ptof_2 )  <  momentum_halfwidth_tof
            )
      )
    )
    &&
    fabs ( electron_tof_1  −  e_tof_center )  <=  electron_halfwidth  // good
        electron  TOF)
  )
  { // begin  if :   Momentums  matched  and  electron  tof  was  good


    for  ( int  k=i ; k<(Ueber . rec . number_of_reconstructed_hits ) ; k++)  // it
        is  k<(Ueber . rec . number_of_reconstructed_hits )  because
        Ueber . rec . time [0]  is  the  first  hit
    {
      if  ((k−i )  <  array_length    ){
          //    recoils [ recoil #][ value ]

            recoils [k−i ][0]  =  Ueber . rec . time [k]  −  Ueber . elec . time [ j ]  +
                electron_tof_1 ;  // recoil  tof
            recoils [k−i ][1]  =  Ueber . rec . x [k ] ;
            recoils [k−i ][2]  =  Ueber . rec . y [k ] ;
            recoils [k−i ][3]  =  Ueber . rec . method [k ] ;  // flag

        // record  the  which  mass  and  charge  goes  with  each  recoil  but
            only  the  first  two
        if  ((k−i )==0)  // first  recoil
        {
          if   ( fabs ( recoil_Ptof_1  +  recoil_Ptof_2 )  <  momentum_halfwidth
              )
          {
            recoils [k−i ][4]  =  mass1 ;
            recoils [k−i ][5]  =  charge1 ;
            recoils [k−i ][6]  =  recoil_Ptof_1 ;
            recoils [k−i ][7]  =  recoil_Py_1 ;
            recoils [k−i ][8]  =  recoil_Px_1 ;
```

117

```cpp
        }
        else
        {
          recoils[k-i][4]  = mass2;
          recoils[k-i][5]  = charge2;
          recoils[k-i][6]  = recoil_Ptof_1_reversed;
          recoils[k-i][7]  = recoil_Py_1_reversed;
          recoils[k-i][8]  = recoil_Px_1_reversed;
        }
      }
      else if  ((k-i)==1) //second recoil
      {
        if   (fabs(recoil_Ptof_1 + recoil_Ptof_2) < momentum_halfwidth
            )
        {
          recoils[k-i][4]   = mass2;
          recoils[k-i][5]   = charge2;
          recoils[k-i][6]   = recoil_Ptof_2;
          recoils[k-i][7]   = recoil_Py_2;
          recoils[k-i][8]   = recoil_Px_2;
        }
        else
        {
          recoils[k-i][4]   = mass1;
          recoils[k-i][5]   = charge1;
          recoils[k-i][6]   = recoil_Ptof_2_reversed;
          recoils[k-i][7]   = recoil_Py_2_reversed;
          recoils[k-i][8]   = recoil_Px_2_reversed;
        }
      }
      else // If it isn't the first or second recoil then I don't know
          what the mass and charge are.
      {
        recoils[k-i][4]   = 0.0;
        recoils[k-i][5]   = 0.0;
        recoils[k-i][6]   = -1000;
        recoils[k-i][7]   = -1000;
        recoils[k-i][8]   = -1000;
      }
    }
  }
}

reaction_flag = reaction_flag - 0.1; // so that the first electron
    goes in to the whole number bin
int bad_electrons = 0;

for (int l = j;l<(Ueber.elec.number_of_reconstructed_hits);l++){
  // electron_tof_1 = fmod((Ueber.elec.time[j] -
      tdc_ns[bunchmarker_channel][1] +
      bunchspacing*1000),bunchspacing);
  if( //fabs(electron_tof_1 - e_tof_center) <= electron_halfwidth
    fabs( fmod((Ueber.elec.time[l] - tdc_ns[bunchmarker_channel][1]
        + bunchspacing*1000),bunchspacing) - e_tof_center ) <=
        electron_halfwidth) // if the electron is good record it.
```

```
            {
              if (  ( (l−j) − bad_electrons) < array_length    ){
              //   electrons [electron #][value]
              //
                electrons [(l−j) − bad_electrons ][0] =
                    fmod(( Ueber . elec . time [ l ] − tdc_ns [ bunchmarker_channel ][1]
                    + bunchspacing *1000) , bunchspacing ) ;   // electron tof
                electrons [(l−j) − bad_electrons ][1] = Ueber . elec . x [ l ];
                electrons [(l−j) − bad_electrons ][2] = Ueber . elec . y [ l ];
                electrons [(l−j) − bad_electrons ][3] = Ueber . elec . method [ l ];
                    // flag

                reaction_flag = reaction_flag + .1;  // reaction_flag
              }
            }
            else {
              bad_electrons ++;  // If the electron is bad , remember how many
                  you have skipped .
            }
          }

          electrons [0][ array_length −1] = reaction_flag ;

          filling =1;

        }
      }
    }


  return  filling ;
}
```

Bibliography

[1] A. Landers *et al.* Photoelectron diffraction mapping: Molecules illuminated from within. *Phys. Rev. Lett.*, 87: 013002, 2001.

[2] Th Weber *et al.* K-shell photoionization of co and n 2 : is there a link between the photoelectron angular distribution and the molecular decay dynamics? *Journal of Physics B: Atomic, Molecular and Optical Physics*, 34:3669, 2001.

[3] Andre T. J. B. Eppink and David H. Parker. Velocity map imaging of ions and electrons using electrostatic lenses: Application in photoelectron and photofragment ion imaging of molecular oxygen. *Review of Scientific Instruments*, 68(9):3477–3484, 1997. doi: 10.1063/1.1148310. URL `http://link.aip.org/link/?RSI/68/3477/1`.

[4] A J R Heck and D W Chandler. Imaging techniques for the study of chemical reaction dynamics. *Annual Review of Physical Chemistry*, 46(1):335–372, 1995. doi: 10.1146/annurev.pc.46.100195.002003. URL `http://www.annualreviews.org/doi/abs/10.1146/annurev.pc.46.100195.002003`.

[5] C Smeenk, L Arissian, A Staudte, D M Villeneuve, and P B Corkum. Momentum space tomographic imaging of photoelectrons. *Journal of Physics B: Atomic, Molecular and Optical Physics*, 42(18):185402, 2009. URL `http://stacks.iop.org/0953-4075/42/i=18/a=185402`.

[6] J. J. Larsen, K. Hald, N. Bjerre, H. Stapelfeldt, and T. Seideman. Three dimensional alignment of molecules using elliptically polarized laser fields. *Phys. Rev. Letts.*, 85, 2000.

[7] Bretislav Friedrich and Dudley Herschbach. Alignment and trapping of molecules in intense laser fields. *Phys. Rev. Lett.*, 74:4623–4626, Jun 1995. doi: 10.1103/PhysRevLett.74.4623. URL `http://link.aps.org/doi/10.1103/PhysRevLett.74.4623`.

[8] Jonas L. Hansen, Lotte Holmegaard, Line Kalhøj, Sofie Louise Kragh, Henrik Stapelfeldt, Frank Filsinger, Gerard Meijer, Jochen Küpper, Darko Dimitrovski, Mahmoud Abu-samha, Christian Per Juul Martiny, and Lars Bojer Madsen. Ionization of one- and three-dimensionally-oriented asymmetric-top molecules by intense circularly polarized femtosecond laser pulses. *Phys. Rev. A*, 83:023406, Feb 2011. doi: 10.1103/PhysRevA.83.023406. URL `http://link.aps.org/doi/10.1103/PhysRevA.83.023406`.

[9] Vinod Kumarappan, Simon S Viftrup, Lotte Holmegaard, Christer Z Bisgaard, and Henrik Stapelfeldt. Aligning molecules with long or short laser pulses. *Physica Scripta*, 76(3):C63, 2007. URL `http://stacks.iop.org/1402-4896/76/i=3/a=N09`.

[10] Wikipedia. Methane — wikipedia, 2012. URL `http://en.wikipedia.org/w/index.php?title=Methane&oldid=479820011`. [Online; accessed 1-April-2012].

[11] N. Wainfan, W. C. Walker, and G. L. Weissler. Photoionization efficiencies and cross sections in o_2, n_2, co_2, a, h_2o, h_2, and ch_4. *Phys. Rev.*, 99:542–549, Jul 1955. doi: 10.1103/PhysRev.99.542. URL `http://link.aps.org/doi/10.1103/PhysRev.99.542`.

[12] R. W. Ditchburn. Absorption cross-sections in the vacuum ultra-violet. iii. methane. *Proceedings of the Royal Society. A, Mathematical, physical, and engineering sciences*, 1955.

[13] A. P. Lukirskii, I. A. Brytov, and T. M. Zimkina. Photoionization Absorption of He, Kr, Xe, CH_4, and Methylal in the 23.6-250 Å Region. *Optics and Spectroscopy*, 17:234, September 1964.

[14] H.-U. and Chun. Fine structure of the x-ray k-absorption edge of carbon in methane. *Physics Letters A*, 30(8):445 – 446, 1969. ISSN 0375-9601. doi: 10.1016/0375-9601(69)90234-5. URL http://www.sciencedirect.com/science/article/pii/0375960169902345.

[15] V Myrseth, J.D Bozek, E Kukk, L.J Sæthre, and T.D Thomas. Adiabatic and vertical carbon 1s ionization energies in representative small molecules. *Journal of Electron Spectroscopy and Related Phenomena*, 122(1):57 – 63, 2002. ISSN 0368-2048. doi: 10.1016/S0368-2048(01)00321-8. URL http://www.sciencedirect.com/science/article/pii/S0368204801003218.

[16] James A. R. Samson, G. N. Haddad, T. Masuoka, P. N. Pareek, and D. A. L. Kilcoyne. Ionization yields, total absorption, and dissociative photoionization cross sections of ch[sub 4] from 110 to 950 [a-ring]. *The Journal of Chemical Physics*, 90(12):6925–6932, 1989. doi: 10.1063/1.456267. URL http://link.aip.org/link/?JCP/90/6925/1.

[17] D R Denne. Measurements of the ultrasoft x-ray absorption of ar, ne, n 2 , o 2 , ch 4 , he and h 2. *Journal of Physics D: Applied Physics*, 3(9):1392, 1970. URL http://stacks.iop.org/0022-3727/3/i=9/a=323.

[18] L. J. Sæthre, O. Sværen, S. Svensson, S. Osborne, T. D. Thomas, J. Jauhiainen, and S. Aksela. High-resolution c 1s photoelectron spectra of methane, ethene, propene, and 2-methylpropene. *Phys. Rev. A*, 55:2748–2756, Apr 1997. doi: 10.1103/PhysRevA.55.2748. URL http://link.aps.org/doi/10.1103/PhysRevA.55.2748.

[19] L Asplund, U Gelius, S Hedman, K Helenelund, K Siegbahn, and P E M Siegbahn. Vibrational structure and lifetime broadening in core-ionised methane. *Journal of Physics B: Atomic and Molecular Physics*, 18(8):1569, 1985. URL http://stacks.iop.org/0022-3700/18/i=8/a=014.

[20] R. Püttner, T. Arion, M. Förstel, T. Lischke, M. Mucke, V. Sekushin, G. Kaindl, A. M. Bradshaw, and U. Hergenhahn. Probing dissociative molecular dications by mapping vibrational wave functions. *Phys. Rev. A*, 83: 043404, Apr 2011. doi: 10.1103/PhysRevA.83.043404. URL http://link.aps.org/doi/10.1103/PhysRevA.83.043404.

[21] E. Kukk, K. Ueda, U. Hergenhahn, X.-J. Liu, G. Prümper, H. Yoshida, Y. Tamenori, C. Makochekanwa, T. Tanaka, M. Kitajima, and H. Tanaka. Violation of the franck-condon principle due to recoil effects in high energy molecular core-level photoionization. *Phys. Rev. Lett.*, 95:133001, Sep 2005. doi: 10.1103/PhysRevLett.95.133001. URL http://link.aps.org/doi/10.1103/PhysRevLett.95.133001.

[22] E Kukk, G Prümper, R Sankari, M Hoshino, C Makochekanwa, M Kitajima, H Tanaka, H Yoshida, Y Tamenori, E Rachlew, and K Ueda. Electronic state dependence in the dissociation of core-ionized methane. *Journal of Physics B: Atomic, Molecular and Optical Physics*, 40(18):3677, 2007.

[23] M. S. Schöffler, J. Titze, N. Petridis, T. Jahnke, K. Cole, L. Ph. H. Schmidt, A. Czasch, D. Akoury, O. Jagutzki, J. B. Williams, N. A. Cherepkov, S. K. Semenov, C. W. McCurdy, T. N. Rescigno, C. L. Cocke, T. Osipov, S. Lee, M. H. Prior, A. Belkacem, A. L. Landers, H. Schmidt-Böcking, Th. Weber, and R. Dörner. Ultrafast probing of core hole localization in n2. *Science*, 320(5878):920–923, 2008. doi: 10.1126/science.1154989. URL http://www.sciencemag.org/content/320/5878/920.abstract.

[24] N. A. Cherepkov, S. K. Semenov, M. S. Schöffler, J. Titze, N. Petridis, T. Jahnke, K. Cole, L. Ph. H. Schmidt, A. Czasch, D. Akoury, O. Jagutzki, J. B. Williams, T. Osipov, S. Lee, M. H. Prior, A. Belkacem, A. L. Landers, H. Schmidt-Böcking, R. Dörner, and Th. Weber. Auger decay of $1\sigma_g$ and $1\sigma_u$ hole states of the n_2 molecule. ii. young-type interference of auger electrons and its dependence on internuclear distance. *Phys. Rev. A*, 82: 023420, Aug 2010. doi: 10.1103/PhysRevA.82.023420. URL http://link.aps.org/doi/10.1103/PhysRevA.82.023420.

[25] T. Osipov, Th. Weber, T. N. Rescigno, S. Y. Lee, A. E. Orel, M. Schöffler, F. P. Sturm, S. Schössler, U. Lenz, T. Havermeier, M. Kühnel, T. Jahnke, J. B. Williams, D. Ray, A. Landers, R. Dörner, and A. Belkacem. Formation of inner-shell autoionizing co$^+$ states below the co^{2+} threshold. *Phys. Rev. A*, 81:011402, Jan 2010. doi: 10.1103/PhysRevA.81.011402. URL http://link.aps.org/doi/10.1103/PhysRevA.81.011402.

[26] R. R. Lucchese, A. Lafosse, J. C. Brenot, P. M. Guyon, J. C. Houver, M. Lebech, G. Raseev, and D. Dowek. Polar and azimuthal dependence of the molecular frame photoelectron angular distributions of spatially oriented linear molecules. *Phys. Rev. A*, 65:020702, Jan 2002. doi: 10.1103/PhysRevA.65.020702. URL `http://link.aps.org/doi/10.1103/PhysRevA.65.020702`.

[27] T. Osipov, M. Stener, A. Belkacem, M. Schöffler, Th. Weber, L. Schmidt, A. Landers, M. H. Prior, R. Dörner, and C. L. Cocke. Carbon k-shell photoionization of fixed-in-space c_2h_4. *Phys. Rev. A*, 81:033429, Mar 2010. doi: 10.1103/PhysRevA.81.033429. URL `http://link.aps.org/doi/10.1103/PhysRevA.81.033429`.

[28] R R Lucchese, R Carey, C Elkharrat, J C Houver, and D Dowek. Molecular frame and recoil frame angular distributions in dissociative photoionization of small molecules. *Journal of Physics: Conference Series*, 141(1): 012009, 2008. URL `http://stacks.iop.org/1742-6596/141/i=1/a=012009`.

[29] F. P. Sturm, M. Schöffler, S. Lee, T. Osipov, N. Neumann, H.-K. Kim, S. Kirschner, B. Rudek, J. B. Williams, J. D. Daughhetee, C. L. Cocke, K. Ueda, A. L. Landers, Th. Weber, M. H. Prior, A. Belkacem, and R. Dörner. Photoelectron and auger-electron angular distributions of fixed-in-space co_2. *Phys. Rev. A*, 80:032506, Sep 2009. doi: 10.1103/PhysRevA.80.032506. URL `http://link.aps.org/doi/10.1103/PhysRevA.80.032506`.

[30] M. Yamazaki, J. Adachi, T. Teramoto, A. Yagishita, M Stener, and P. Decleva. 3d mapping of photoemission from a single oriented h_2 molecule. *J. Phys. B: At. Mol. Opt. Phys.*, 42, 2009.

[31] Kouichi Hosaka, Jun ichi Adachi, Alexander V. Golovin, Masahiko Takahashi, Noboru Watanabe, and Akira Yagishita. Coincidence velocity imaging apparatus for study of angular correlations between photoelectrons and photofragments. *Japanese Journal of Applied Physics*, 45(3A):1841–1849, 2006. doi: 10.1143/JJAP.45.1841. URL `http://jjap.jsap.jp/link?JJAP/45/1841/`.

[32] . D. Landau L and M. Lifshitz E. *Quantum Mechanics (Non-Relativistic Theory)*. 1977.

[33] R. Dörner, V. Mergel, O. Jagutzki, L. Spielberger, J. Ullrich, R. Moshammer, and H. Schmidt-Böcking. Cold target recoil ion momentum spectroscopy: a momentum microscope to view atomic collision dynamics. *Physics Reports*, 330:95, 2000.

[34] J Ullrich, R Moshammer, A Dorn, R Dörner, L Ph H Schmidt, and H Schmidt-Böcking. Recoil-ion and electron momentum spectroscopy: reaction-microscopes. *Reports on Progress in Physics*, 66(9):1463, 2003. URL `http://stacks.iop.org/0034-4885/66/i=9/a=203`.

[35] H. Bluhm, K. Andersson, T. Araki, K. Benzerara, G.E. Brown, J.J. Dynes, S. Ghosal, M.K. Gilles, H.-Ch. Hansen, J.C. Hemminger, A.P. Hitchcock, G. Ketteler, A.L.D. Kilcoyne, E. Kneedler, J.R. Lawrence, G.G. Leppard, J. Majzlam, B.S. Mun, S.C.B. Myneni, A. Nilsson, H. Ogasawara, D.F. Ogletree, K. Pecher, M. Salmeron, D.K. Shuh, B. Tonner, T. Tyliszczak, T. Warwick, and T.H. Yoon. Soft x-ray microscopy and spectroscopy at the molecular environmental science beamline at the advanced light source. *Journal of Electron Spectroscopy and Related Phenomena*, 150(2-3):86 – 104, 2006. URL `http://www.sciencedirect.com/science/article/pii/S0368204805004573`.

[36] Lawrence Berkeley National Laboratory's photostream. URL `http://www.flickr.com/photos/berkeleylab/3351606687/`.

[37] Thorsten Weber. *Untersuchung der verschränkten Bewegung freier Elektronenpaare emittiert aus Ein- und Zweizentren Coulomb-Potentialen in Photoabsorptionsprozessen*. PhD thesis, Johann Wolfgang Goethe-Universität Frankfurt am Main, 2003.

[38] W. C. Wiley and I. H. McLaren. Flight mass spectrometer with improved resolution. *Review of Scientific Instruments*, 26(12):1150 –1157, dec 1955. ISSN 0034-6748. doi: 10.1063/1.1715212.

[39] RoentDek Handels GmbH. Microchannel plate detector. URL `http://www.roentdek.com/manuals/MCP%20Delay%20Line%20manual(9.22.1003.1).pdf`.

[40] Joseph Ladislas Wiza. Microchannel plate detectors. *Nucl. Instr. Meth.*, 162:587, 1979.

[41] Wikipedia. Microchannel plate detector — wikipedia, 2012. URL `http://en.wikipedia.org/w/index.php?title=Microchannel_plate_detector&oldid=481021113`. [Online; accessed 1-April-2012].

[42] Stanford Research Systems. High voltage power supplies. URL `http://www.thinksrs.com/downloads/PDFs/Catalog/PS300c.pdf`.

[43] Cronologic. User manual, 2011. URL `http://www.cronologic.de/products/time_measurement/hptdc/HPTDC_description.pdf`.

[44] Rene Brun and Fons Rademakers. Root - an object oriented data analysis framework. *Nuclear Instruments and Methods in Physics Research Section A*, 389(1–2):81 – 86, 1997. ISSN 0168-9002. doi: 10.1016/S0168-9002(97)00048-X. URL `http://www.sciencedirect.com/science/article/pii/S016890029700048X`.

[45] M. Kato, Y. Morishita, M. Oura, H. Yamaoka, Y. Tamenori, K. Okada, T. Matsudo, T. Gejo, I.H. Suzuki, and N. Saito. Absolute photoionization cross sections with ultra-high energy resolution for ar, kr, xe and n2 in inner-shell ionization regions. *Journal of Electron Spectroscopy and Related Phenomena*, 160(1–3):39 – 48, 2007. ISSN 0368-2048. doi: 10.1016/j.elspec.2007.06.003. URL `http://www.sciencedirect.com/science/article/pii/S0368204807002204`.

[46] Rana N.S. Sodhi and C.E. Brion. Reference energies for inner shell electron energy-loss spectroscopy. *Journal of Electron Spectroscopy and Related Phenomena*, 34(4):363 – 372, 1984. ISSN 0368-2048. doi: 10.1016/0368-2048(84)80050-X. URL `http://www.sciencedirect.com/science/article/pii/036820488480050X`.

[47] K Jakubowska, G Vall-llosera, A Kivimäki, M Coreno, E Melero García, M Stankiewicz, and E Rachlew. Lyman and balmer emission following core excitations in methane and ammonia molecules. *Journal of Physics B: Atomic, Molecular and Optical Physics*, 40(8):1489, 2007. URL `http://stacks.iop.org/0953-4075/40/i=8/a=003`.

[48] Roald Wangsness. *Electromagnetic Fields, 2nd ed.* Wiley, 1986. Appendix A: Motion of Charged Particles, Equation A-46.

[49] David A Dahl. Simion for the personal computer in reflection. *International Journal of Mass Spectrometry*, 200 (1–3):3 – 25, 2000. ISSN 1387-3806. doi: 10.1016/S1387-3806(00)00305-5. URL `http://www.sciencedirect.com/science/article/pii/S1387380600003055`. <ce:title>Volume 200: The state of the field as we move into a new millenium</ce:title>.

[50] Ahmed H. Zewail. Four-dimensional electron microscopy. *Science*, 328:187, 2010.

[51] H. N. Chapman *et al.* Femtosecond x-ray protein nanocrystallography. *Nature*, 470:73–77, 2011.

[52] Y Arasaki, K Takatsuka, K Wang, and V McKoy. Time-resolved photoelectron spectroscopy of wavepackets through a conical intersection in no2. *J. Chem. Phys.*, 132:124307, 2010.

[53] P. Hockett, C. Z. Bisgaard, O. J. Clarkin, and A. Stolow. Time-resolved imaging of purely valence-electron dynamics during a chemical reaction. *Nature Physics*, 7, 2011.

[54] R Flammini, M Satta, E Fainelli, G Alberti, F Maracci, and L Avaldi. The role of the methyl ion in the fragmentation of ch 4 2+. *New Journal of Physics*, 11:083006, 2009.

[55] J. Viefhaus, A. N. Grum-Grzhimailo, N. M. Kabachnik, and U. Becker. Electron-electron coincidence study of double auger processes in atoms. *J. Electron. Spectrosc. Relat. Phenom.*, 141:121–126, 2004.

[56] R. Dörner, V. Mergel, O. Jagutzki, L. Spielberger, J. Ullrich, R. Moshammer, and H. Schmidt-Böcking. Cold target recoil ion momentum spectroscopy: a momentum microscope to view atomic collision dynamics. *Physics Reports*, 330:95, 2000.

[57] T Jahnke, Th Weber, T Osipov, A L Landers, O Jagutzki, L Ph H Schmidt, C L Cock, M H Prior, H Schmidt-Böcking, and R Dörner. Multicoincidence studies of photo and auger electrons from fixed-in-space molecules using the coltrims technique. *J. Elec. Spect. and Rel. Phen.*, 141:229, 2004.

[58] T. N. Rescigno, B. H. Lengsfield, and A. E. Orel. Interchannel coupling and ground state correlation effects in the photoinization of co. *J. Chem. Phys.*, 99:5097, 1993.

[59] S. Miyabe, C. W. McCurdy, A. E. Orel, and T. N. Rescigno. Theoretical study of asymmetric molecular-frame photoelectron angular distributions for $c\,1s$ photoejection from co_2. *Phys. Rev. A*, 79:053401, 2009.

[60] C S Trevisan, C W McCurdy, and T N Rescigno. Imaging molecular geometries with molecular frame photoelectron angular distributions from core hole ionization. *J. Phys. B: At., Mol. and Opt. Phys.*, XX:submitted, 2012.

[61] J B Williams, C S Trevisan, M S Schöffler, T Jahnke, I Bocharova, H Kim, B Ulrich, R Wallauer, F Sturm, T N Rescigno, A Belkacem, R Dörner, Th Weber, C W McCurdy, and A L Landers. Imaging polyatomic molecules in three dimensions using molecular frame photoelectron angular distributions. *Phys. Rev. Letts.*, XXX:submitted, 2012.

[62] E Fainelli, G alberti, R Flammini, F Maracci, P Bolognesi, M Mastropietro, and L Avaldi. Fragmentation of ch_4^{++} following c 1s ionisation studied by auger electrion-ion-ion coincidence experiments. *J. Elect. Spect. and Rel. Phen.*, 161:51, 2007.

[63] B Ulrich, A Vredenborg, A Malakzadeh, L Ph H Schmidt, T Havermeier, M Meckel, K Cole, M Smolarski, Z Chang, T Jahnke, and R Dörner. Imaging the structure of the argon and neon dimer, trimer and tetramer. *J. Phys. Chem. A*, 115:6936, 2011.

[64] A Matsuda, E J Takahasi, and A Hishikawa. *J. Chem. Phys.*, 127:114318, 2007.

[65] T Osipov, C L Cocke, M H Prior, A Landers, Th. Weber, O Jagutzki, L Schmidt, H Schmidt-Böcking, and R Dörner. Photoelectron-photoion momentum spectroscopy as a clock for chemical rearrangements: Isomerization of the dication of acetylene to the vinyidene configuration. *Phys. Rev. Letts.*, 90:233002, 2003.

[66] M H Wong and L Radom. Methane dication: Planar but not square. *J. Am. Chem. Soc.*, 111:1155, 1989.

[67] J. C. Slater. *The Self-Consistent Field for Molecules and Solids: Quantum Theory of Molecules and Solids*, volume 4. McGraw-Hll, New York, 1974.

[68] R J Renka. Algorithm 660: Qshep2d: Quadratic method for bivariate interpolation of scattered data. *ACM Transactions on Mathematical Software*, 14:149, 1988.

[69] H. Lischka, R. Shepard, I. Shavitt, R. M. Pitzer, M. Dallos, Th. Müller, P. G. Szalay, F. B. Brown, R. Ahlrichs, H. J. Böhm, A. Chang, D. C. Comeau, R. Gdanitz, H. Dachsel, C. Ehrhardt, M. Ernzerhof, P. Höchtl, S. Irle, G. Kedziora, T. Kovar, V. Parasuk, M. J. M. Pepper, P. Scharf, H. Schiffer, M. Schindler, M. Schöffler, M. Seth, E. A. Stahlberg, J.-G. Zhao, S. Yabushita, Z. Zhang, M. Barbatti, S. Matsika, M. Schuurmann, D. R. Yarkony, S. R. Brozell, E. V. Beck, , J.-P. Blaudeau, M. Ruckenbauer, B. Sellner, F. Plasser, and J. J. Szymczak. COLUMBUS, an ab initio electronic structure program, release 7.0 2012.